Flux noise in a magnetic field

Stavenga, T.

DOI
10.4233/uuid:57e68a2b-0d80-40bb-a105-8a0757c98c05

Publication date
2023

Document Version
Final published version

Citation (APA)
Stavenga, T. (2023). *Flux noise in a magnetic field*. [Dissertation (TU Delft), Delft University of Technology]. https://doi.org/10.4233/uuid:57e68a2b-0d80-40bb-a105-8a0757c98c05

Flux noise in a magnetic field

Flux noise in a magnetic field

Proefschrift

ter verkrijging van de graad van doctor
aan de Technische Universiteit Delft,
op gezag van de Rector Magnificus Prof. dr. ir. T.H.J.J. van der Hagen,
voorzitter van het College voor Promoties,
in het openbaar te verdedigen op woensdag 21 Juni 2023 om 12:30 uur

door

Thijs STAVENGA

Master of Science in Master Applied Physics,
Technische Universiteit Delft, Delft, Nederland,
geboren te Woudenberg, Nederland.

Dit proefschrift is goedgekeurd door de promotoren.

Prof. dr. L. Di Carlo,
Prof. dr. B.M. Terhal,

Samenstelling promotiecommissie bestaat uit:

Rector Magnificus,	voorzitter
Prof. dr. L. Di Carlo,	Technische Universiteit Delft, *promotor*
Prof. dr. B.M. Terhal,	Technische Universiteit Delft, *promotor*
Onafhankelijke leden:	
Dr. P. Bertet	Université Paris-Saclay
Prof. dr. F. Kuemmeth	University of Copenhagen
Prof. dr. Y.M. Blanter	Technische Universiteit Delft
Dr. C.K. Andersen	Technische Universiteit Delft
Reservelid:	
Prof. dr. G.A. Steele	Technische Universiteit Delft, *reservelid*

Geprint door: Gildeprint, Enschede – www.gildeprint.nl

Voor & Achter: Artistic impression of flux noise affecting the devices discussed in this work.
Design by Lucía Pellitero.

Casimir PhD Series, Delft-Leiden 2023-06

ISBN 978-94-6419-836-2

Een digitale versie van dit proefschrift is beschikbaar via
https://repository.tudelft.nl/.

Contents

Summary

Quantum computers promise to speedup certain problems that conventional computers take too long to solve. These problems include nitrogen fixation, quantum chemistry and prime factorization. One promising platform for the implementation of a practical quantum computer are superconducting qubits in combination with circuit quantum electrodynamics (CQED). However, preventing the large scale application of quantum computers is noise and decoherence, limiting the size and depth of a quantum algorithm. Particularly flux noise plagues tunable qubits, limiting their flexibility and fidelity.

One of the most used and advanced qubits is the transmon, a LC oscillator with a capacitor in parallel with a non-linear inductive element called a Josephson junction. Conventionally, the Josephson junction is formed with an Al-AlO-Al tunnel barrier. Contrastingly, here we use a InAs nanowire covered with a thin layer of Al forming a S-N-S Josephson junction. Crucially, this junction is magnetic field compatible, allowing us to do experiments with cQED in a magnetic field. Additionally this junction is voltage-tunable, opening the path towards lower distortion voltage gates. This thesis focusses on measuring the flux noise in a magnetic field using the nanowire Josephson junction. To that end, the chapters address the necessary conditions to achieve this goal.

In the first experimental chapter (Ch. 3) of this thesis we show extended coherence of both the voltage and flux tunable nanowire transmon. Furthermore we investigate the evolution of a nanowire transmon in parallel magnetic field up to 70 mT, the upper bound set by the closing of the induced gap.

In the next chapter (Ch. 4) we make airbridges compatible with a magnetic field by making them out of NbTiN. However since the InAs nanowires are sensitive to temperature during fabrication, the standard reflow recipe is not adequate. We implemented grayscale lithography to allow us, with minor modifications to the fabrication recipe, to have airbridges with the nanowire junction.

In the second experimental chapter (Ch. 5) we perform the main experiment of this thesis, by applying an in-plane magnetic field to the flux tunable nanowire transmon. In steps of 10 mT we increased the magnetic field and measured the flux noise amplitude by sweeping the flux bias and monitoring the coherence. The flux noise amplitude increased linearly as a function of magnetic field.

In the last experimental chapter (Ch. 6) we do noise spectroscopy meas-

urements using spin-locking and repeated Ramsey measurements for different magnetic fields and sensitivities to flux noise. The increase in the flux noise amplitude is not reproduced in the noise spectroscopy measurements.

Samenvatting

Kwantumcomputers beloven om bepaalde problemen die voor conventionele computers te lang duren in een redelijke tijd op te lossen. Dit soort problemen omvat zaken als stikstofbindin, kwantumchemie en het factoriseren van priemgetallen. Een veelbelovend platform voor de implementatie van een kwantumcomputer zijn supergeleidende qubits in combinatie met circuit kwantumelectrodynamica (cQED). Echter, voor de toepassing van kwantumcomputers op grote schaal zijn ruis en decoherentie een groot obstakel, wat de grootte en diepte van een kwantumalgorithme limiteert. Specifiek flux ruis is een groot probleem voor verstelbare qubits, iets wat de flexibiliteit en de betrouwbaarheid limiteert.

Een van de meest gebruikte en geavanceerde qubits is de transmon, een LC oscillator met een condensator in parallel met een niet-lineare spoel, ookwel een Josephson junctie genoemd. In het algemeen wordt een Josephson junctie gevormd door een stapel van Al-AlO-Al, wat een tunnelbarrière vormt. Contrasterend, hier gebruiken we een InAs nanodraad bedekt met een dun laagje Al wat een S-N-S Josephson junctie vormt. Cruciaal is dat deze junctie bestand is tegen een magnetisch veld, zodat we experimenten kunnen doen met cQED in dit magnetische veld. Daarnaast is deze junctie ook verstelbaar met een voltage, wat een pad opent voor distortievrije 2-qubit operaties. Deze thesis focust op het meten van flux ruis in een magnetisch veld gebruik makende van de nanodraad Josephson junctie. Daarvoor zijn er hoofdstukken die de noodzakelijke voorwaarden behandelen om dit doel te realiseren.

In het eerste experimentele hoofdstuk (H. 3) van deze thesis laten we de coherentie van zowel de voltage en flux verstelbare nanodraad transmons zien. Bovendien onderzoeken we de evolutie van een nanodraad transmon in een parallel magnetisch veld tot wel 70 mT, gelimiteerd door het sluiten van het supergeleidende gat.

In het opvolgede hoofdstuk (H. 4) maken we de luchtbruggen die bestand zijn tegen een magnetisch veld door ze van NbTiN te maken. Desondanks, omdat de InAs nanodraden gevoelig zijn voor temperatuur tijdens het fabricatieproces, is het standaard vloei recept niet goed genoeg. We implementeren grijstint lithografie wat ervoor zorgt dat we luchtbruggen kunnen hebben met de nanodraad juncties, zonder grote veranderingen aan het fabricatie recept.

In het tweede experimentele hoofdstuk (H. 5) voeren we het hoofdexperiment uit van deze thesis, door een magnetisch veld in het vlak toe te passen aan de flux verstelbare nanodraad transmon. In stappen van 10 mT voe-

ren we het magnetisch veld op en meten we de flux ruis amplitude door de flux verstelling te veranderen en de coherentie te monitoren. De flux ruis amplitude verhoogde lineair als een functie van het magnetisch veld.

In het laatste experimentele hoofdstuk (H. 6) voeren we ruisspectroscopie metingen uit door gebruik te maken spinvergrendeling en herhaalde Ramsey metingen voor verschillende magnetische velden en gevoeligheden voor flux ruis. De verhoging van de flux ruis amplitude is niet terug te zien in de ruisspectroscopie metingen.

1

Introduction

1

The information age has brought us many life improvements over the past where computers did not play a role in our daily lives. From engineering, physics, chemistry and medicine to the offices and homes, computers are used everywhere and necessary in all those places. To such an extent they are vital that whole factories and industries collapse without the digital infrastructure they provide. This becomes clear when an attack is done on a piece of digital infrastructure and the societal consequences are felt without the service it provides.

Physics and engineering have been revolutionized. While it used to be difficult to calculate the dynamics of anything but the simplest systems. Computers have allowed us to simulate even some of the most complicated systems with ever increasing accuracy. Weather patterns and climate change used to be notoriously difficult to forecast, with recent computation and modelling advances these become more accurate every time.

However when it comes to quantum mechanics the computer is not doing so well. Only the simplest and smallest systems can be simulated accurately. Scaling up to larger systems, such as the ones encountered frequently in physics and chemistry are no longer simulatable on a computer. This is because every time a particle with only two quantum states is added to the system, the number of states that in principle have to be taken into account doubles. Adding only a few dozen particles quickly makes the computation out of reach of a current quantum computer. Making a computer more powerful also does not get us very far, since for every particle added one needs to double the computing power. Now that Moore's law is coming to an end, it does not seem likely that simply waiting for computation advances will get us to a place where computers will ever be able to simulate systems with even a moderate amount of quantum degrees of freedom. A fundamentally different solution is needed that can handle the computation amount required by quantum systems. The natural idea is to use a controllable quantum system to simulate the quantum system of interest. This is called an analog quantum computer. Here the system needs to map one-to-one to the system of interest. However this is not always possible. For the other situations a different quantum computer has been invented, the digital quantum computer. This one requires many more quantum resources, but in principle it can simulate any quantum system imaginable. A large programmable quantum computer is the holy grail of the field of quantum computation and currently many people are working towards this goal. Even though a practical one that is more powerful than a conventional computer does not exist at the moment, people have theorized programs and algorithms that the quantum computer can compute more efficiently than a normal computer. One of them is Shor's algorithm named after its inventor. This algorithm is a purely quantum mechanical in the way that is only provides a speed-up over any known non-quantum algorithm when it is run on a quantum computer. Of course is is still possible to run it on a normal computer but without the desirable speed boost. The

purpose of this algorithm is to factor numbers into its prime factors. For large numbers this becomes a very hard task for conventional computers to such an extent that a large part of our public key cryptography is built on it. The numbers used in cryptography are so large that it is expected that even future computers will not be able to factor them. If such a number would be factored the cryptography is broken and the security it provides vanishes. Current quantum computers are no where near good enough to run this algorithm so there is no reason to worry that this becomes a security threat. However this algorithm was an early breakthrough that proved that quantum computers could be useful beyond simulating quantum systems and it inspired many to try and build a quantum computer.

1.1. The qubit

The quantum computer is made out of quantum bits, or qubits in short. but what is a qubit? Unfortunately there is no analog found in our classical world. The conventional bit, the smallest unit of information, of the computer, denotes whether the piece of information is in either the 0 or the 1 state. The quantum bit can be in a superposition of the $|0\rangle$ and $|1\rangle$ state, $\alpha|0\rangle + \beta|1\rangle$. We see that there are many more possible combinations between the two states, α and β in principle can be any complex number, as long as $|\alpha|^2 + |\beta|^2 = 1$. This condition on the state implies that qubit state can be represented on the surface of a sphere, also called the Bloch sphere. A picture of a qubit state represented on the Bloch sphere can be seen in Fig. 1.1. A interpretation of α and β that is more conducive to the Bloch sphere picture is one that measures the angle between the $|0\rangle$ state on the north pole and the qubit state, and the phase is the angle on the equator with the qubit state.

There are many different ways of implementing a qubit, each with their own advantages and disadvantages. Some of the most common technologies include: Spin qubits, Superconducting qubits and trapped ions. Although the implementation differs between technology, they all store a quantum state that is addressable and can be manipulated. In order for these qubits to make a quantum computer, several requirements have to be met. We have to be able to readout, manipulate and couple the qubit. In this thesis we focus on superconducting qubits, specifically the transmon. In this case the manipulation, readout and coupling are all done using microwave frequency waveguides. The microwave frequency makes is it easy to design waveforms for the readout and manipulation. Furthermore, the readout signal can be analyzed using microwave frequency equipment and computers.

However, even though the control is relatively easy, superconducting qubits have other disadvantages compared to other technologies. The time that they can keep their quantum information, the so called coherence time, is relatively short compared to trapped ions for example. This, to-

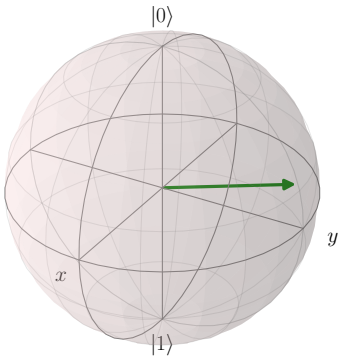

Figure 1.1: Bloch sphere representation of the qubit state. The conventional computer only as access to the states 0 and 1, represented on the poles of the Bloch sphere. The qubit can occupy any state on the Bloch sphere. One such state is represented with the arrow.

gether with other errors, limits the size of the quantum computer in practice. Other technologies suffer from different errors and limitations that limit their ability to make a large quantum computer as well. These errors mean that any algorithm requiring many quantum gates and qubits has no realistic chance of executing successfully. Therefore, people have been looking at quantum error correction mitigating the worst effects of these errors. Here many qubits are coded into one or a few, which are resilient to errors.

However, even with quantum error correction the amount of errors is only reduced and not completely overcome. Therefore, the ideal solution would be to reduce the errors. Additionally, this would also improve the quantum error correction, since reducing the errors also helps for quantum error correction. One of the most promising quantum technologies are the superconducting qubits. In particular the transmon is widely used and it has been shown that quantum error correction is possible in this platform [1–3]. Currently the error rates are still very close to the threshold, where correction does better than just using the bare qubit. There are two types of errors, first there are control errors, where signals applied to the qubit are not perfect resulting into an error in the single-qubit or two-qubit gate. Alternatively there are decoherence errors that are due to an uncontrolled environment of the qubit. These decoherence errors fall into two broad categories, relaxation and dephasing. Relaxation is the loss of the qubit excitation to some part of the environment the qubit couples to. On the other hand, dephasing is the environment randomly changing the phase via a σ_z type coupling. Both decoherence errors cause the qubit to lose its quantum information.

One of the most persistent errors is due to flux noise. Flux noise is a

dominant source of dephasing in qubits that are flux tunable. Flux tunability is useful as a flexibility to tune the qubit transition to a specific frequency and is also frequently used for the control of 2-qubit gates [4–10]. Here, a magnetic flux is able to tune the transition frequency of the qubit using a SQUID loop. A SQUID-loop is a parallel arrangement of two Josephson junctions that encircle an area. The area can be penetrated by a magnetic field forming a magnetic flux. This flux causes a phase shift between the two Josephson junction potentials (currents). Depending on the phase a constructive or destructive interference between the currents is observed. The simplest form of a Josephson junction forms a $\cos\hat{\phi}$ potential. Having two of these junction potentials with one phase shifted relative to the other plays out the interference and the tunability of the qubit. The resulting combination of the two potentials is still a cosine with a different amplitude and phase. However this control knob also makes the qubit sensitive to dephasing via flux noise. Magnetic flux noise causes dephasing by randomly changing the qubit frequency and phase. Flux noise has been a practical limitation to the technology since it was first measured in a SQUID [11]. Though progress has been made [12–17] and models have been proposed [18–21], the microscopic origin of flux noise has never been unambiguously confirmed.

Although the microscopic origin currently is not known, models have been made based on spinful two-level systems [17, 19]. These spins reside on the surface of the superconductor that is part of the SQUID loop. These spins are the ones that couple the largest to the SQUID loop and away from there the coupling is so small it can be neglected. When one of these spins changes its state, a small different flux is introduced to the SQUID loop. An ensemble of these spins can create the flux noise.

The question now is, if we can change the dynamics of spin fluctuator, maybe it will be possible to affect the flux noise. Since the spin couples to a magnetic field, the idea is that if we apply a magnetic field to the spins we can change the flux noise spectrum. To achieve this, two ingredients are needed, Magnetic field compatible Josephson junction and a qubit that couples to the flux noise, while being stable in a magnetic field, to measure the noise spectrum. These requirements are discussed in the next section.

1.2. Circuit Quantum Electrodynamics (cQED)

Electrical circuits analog to conventional integrated circuits can be made in the context of quantum computing as well. The superconducting qubits are the computing analog to the integrated circuit and the interconnects are made out of superconducting coplanar waveguides (CPW). Contrary to the integrated circuit, all the signals are applied in the microwave range of typically 4-8 GHz. This flexibility of routing circuits on chip makes cQED a compelling technology and one of the simplest ways of making an integrated quantum computer. The signals are applied via a feedline made

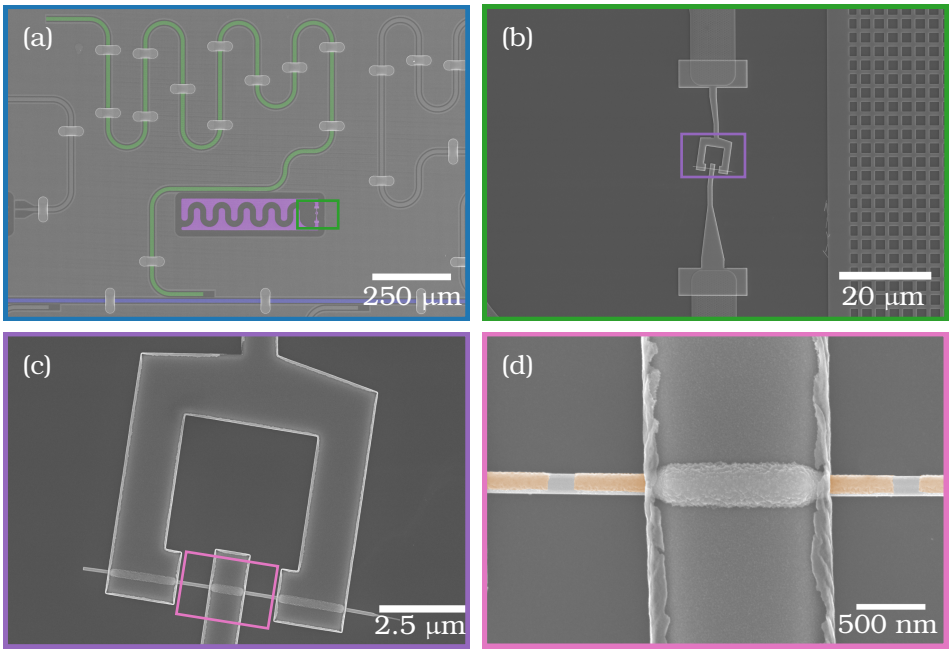

Figure 1.2: An overview of one of the chips used in the thesis. (a) False colored SEM image of the chip, with in green the readout resonator, in blue the feedline and in purple the qubits. (b) Zoom in on the SQUID loop, that has an area of roughly 20 µm^2. (c) Zoom in on the SQUID loop with the two junctions on the bottom. (d) High resolution SEM image with a zoom in on the junction itself. The aluminum superconductor is false colored in orange and is removed for 200 nm to define the junction.

out of a CPW via a readout resonator, also implemented with a CPW, to the qubit. The readout resonator is a resonator with one end capacitively coupled to the feedline and the other end shorted to the chip ground. The capacitive coupling acts as an open for the resonator such that the resonance frequency is at $\lambda/4$. This configuration is chosen as it makes the shortest possible resonator. For the typical frequencies used, 6-7 GHz resonance frequency, the length of the resonator is 3-4 mm. Since the chips in this thesis is only 2.3 mm by 7 mm, the resonator is meandered to save space. The qubit itself is coupled to the resonator, this has the advantage that the decay of the qubit excitation is filtered by the resonator, making it irrelevant when the detuning of the qubit with respect to the resonator is large enough. There are many superconducting qubits that can be chosen to be implemented in the chip, each with their own advantages and disadvantages. Some of these, that have recently been popular, include the fluxonium [22, 23], the flux qubit [24], the 0-π qubit [25–28] and the trans-

mon. [29, 30], all of these can be implemented in combination with cQED. Perhaps the simplest of all of these implementations is the transmon, which just consists of a Josephson junction in parallel with a relatively large capacitor. The Josephson junction can be seen as a non-linear inductor with a $\cos(\hat{\phi})$ potential instead of the linear inductor potential of $\hat{\phi}^2$. The inductor in parallel with the capacitor makes a well-known harmonic oscillator circuit. In the quantum case this becomes a quantum harmonic oscillator where the energy levels are equally spaced. In the case that the inductor deviates from the $\hat{\phi}^2$ potential the energy levels are not equally spaced anymore. The deviation from the harmonic potential can be quantified by the anharmonicity, which is positive for a potential that is larger than its $\hat{\phi}^2$ approximation and negative in the other case. Therefore the cosine potential of the Josephson junction has a negative anharmonicity. When this is quantified more, the attention is turned to the Hamiltonian of the transmon,

$$H = 4E_c\hat{n}^2 - E_J\cos(\hat{\phi}). \tag{1.1}$$

Here, E_C is the charging energy to add an electron to the capacitor plate of the transmon and E_J is the Josephson energy associated with the Josephson junction. The Josephson term can be expanded into a Taylor series, yielding $-E_J\cos(\hat{\phi}) = -E_J + E_J\hat{\phi}^2/2 - E_J\hat{\phi}^4/4! + \ldots$. The constant term just gives an addition to the energy of the eigenstates, but this cannot observed, since only transitions between states can be driven. This means that the constant term can be neglected in calculating the transition frequencies. The quartic term is dominant when calculating the anharmonicity using perturbation theory, note that the sign of this term is negative implying that the anharmonicity is negative as well. When only taking the quadratic term the Hamiltonian can be diagonalized to $H = hf_0(a^\dagger a + 1/2)$, with the transition frequency $f_0 = \sqrt{8E_C E_J}$. The anharmonicity of the transmon allows to limit the consideration of the Hilbert space to just the qubit subspace. Since we are using a nanowire in this thesis the details of the hamiltonian are different (Sec. 2), however the big picture with the negative anharmonicity is the same. A picture of two nanowire Josephson junctions is shown in Fig. 1.2(d).

1.2.1. Applying a magnetic field

The simplest and most used junction is the superconductor - insulator - superconductor (SIS) tunnel junction. The area of overlap and the thickness of the tunnel barrier determine the Josephson energy of the junction allowing for precise engineering [31–34]. However one of the disadvantages of the SIS junction is that the standard recipe is not compatible with a magnetic field of larger than about 40 mT [35]. Adjusting this recipe using a thinner aluminum superconductor is possible and greatly extends the magnetic field compatibility [36]. Another path towards a field compatible junction is to use a nanowire Josephson junction. The junction used

in this case is a nanowire made of InAs with a small shell of 10 nm aluminum. These have been studied extensively in the context of Majorana fermions [37, 38]. Here the weak link instead of a tunnel barrier is given by a semiconductor. The density of states, or the subbands, can be tuned by voltage on a gate, allowing for an additional control knob to cQED [39–42]. In principle this can allow for simplified control schemes compared to flux control. However in practice flux control is more stable and reproducible. Additionally due to the thin layer of the aluminum superconductor these semiconductor Josephson junctions are also magnetic field compatible up to at least 1 T [43]. Besides the junction, the superconductor that the metal of the chip is made of also has to survive magnetic fields. Additionally even if the superconductivity is maintained the ac losses in the 6-7 GHz range have to be low, since the resonators operate in this regime. By having a thin layer of NbTiN it is possible to have high quality factor resonators operating at several Tesla magnetic fields [43]. These two provide the basis of the magnetic field investigations into flux noise.

1.2.2. Expectation of the spin dynamics in a magnetic field

Since a magnetic field will be applied to the sample it is interesting to see what the spin dynamics are in a magnetic field. A simple semi-classical model is explored that takes the spins as independent fluctuators that are aligned with the field direction. There can be many criticisms on this model, for example the spins are not independent, the alignment with the magnetic field might not be in the same direction as the coupling is to the SQUID loop. Nonetheless the model can give a simple motivation and expectation for the experiment. The model starts with the Zeeman energy splitting of the two spin states due to the magnetic field,

$$H = \frac{1}{2} g \mu_B B \sigma_z.$$

Here, g is the gyromagnetic ratio, μ_B is the Bohr magneton and B the magnetic field strength. The energies of the eigenstates are $|\uparrow\rangle = -\frac{1}{2} g\mu_B B$ and $|\uparrow\rangle = \frac{1}{2} g\mu_B B$ and the energy splitting between the states is $\Delta E = g\mu_B B$. The partition function is $Z = 2\cosh\left(\frac{\Delta E}{2kT}\right)$ and the resulting probabilities in steady state and thermal equilibrium are

$$p_\uparrow = \frac{\exp\left[\frac{\Delta E}{2kT}\right]}{2\cosh\left(\frac{\Delta E}{2kT}\right)} \qquad p_\downarrow = \frac{\exp\left[-\frac{\Delta E}{2kT}\right]}{2\cosh\left(\frac{-\Delta E}{2kT}\right)}.$$

In order to calculate the noise power spectral density (PSD) of the spinful switcher in a magnetic field, the Wiener-Kinchin theorem is used,

$$S(f) = \int_{-\infty}^{\infty} \mathrm{E}\left[(x_t - \mu_x)(x_{t+\tau} - \mu_x)\right] e^{-2\pi i f \tau} d\tau.$$

The evaluation of this equation requires the knowledge of $x_{t+\tau}$ and the dynamics of the switcher trace x. Assuming the dynamics are Markovian, the master equation for the probability of finding a state based on the switching rates can be written down,

$$\begin{bmatrix} \frac{dP_\uparrow}{dt} \\ \frac{dP_\downarrow}{dt} \end{bmatrix} = \begin{bmatrix} -\Gamma_{\uparrow\downarrow} & \Gamma_{\downarrow\uparrow} \\ \Gamma_{\uparrow\downarrow} & -\Gamma_{\downarrow\uparrow} \end{bmatrix} \begin{bmatrix} P_\uparrow \\ P_\downarrow. \end{bmatrix}$$

This equation gives the evolution of the probabilities based on the initial probability of finding the spin in a particular state. In the steady state case the evolution of the probabilities is zero, implying that the ratio of probabilities is the same as the ratio of the transition rates. Using this equation it is possible to find the probability after some time has elapsed, which is required to evaluate the expectation value. The expectation value is evaluated and is found to be

$$\mathrm{E}\left[(x_t - \mu_x)(x_{t+\tau} - \mu_x)\right] = \mathrm{sech}^2\left(\frac{\Delta E}{kT}\right) e^{-(\Gamma_{\uparrow\downarrow}+\Gamma_{\downarrow\uparrow})t}$$

such that the noise PSD of the TLS becomes

$$S(f) = \mathrm{sech}^2\left(\frac{g\mu_b B}{kT}\right) \frac{\Gamma}{\Gamma^2 + (2\pi f)^2}$$

Here, $\Gamma = \Gamma_{\uparrow\downarrow} + \Gamma_{\downarrow\uparrow}$ is the sum of the rates. This equation shows that it is possible to decrease the noise of a single TLS by increasing the magnetic field and polarizing the spin. An ensemble of spins with a particular distribution of relaxation rates can produce $1/f$ noise. This is still in combination with the sech^2 term that decreases the flux noise amplitude rapidly in a magnetic field. The factor $g\mu_B$ is about 28 GHz/T and the factor kT is about 1 GHz at 50 mK, so that already at 35 mT the thermal energy and the Zeeman energy are roughly the same. This is assuming that the spin bath is at around 50 mK. The noise PSD at that point is already reduced by a factor of 0.42 and decreases exponentially afterwards.

This model is one of the motivations to perform the experiment and it will be tested against the measured data in later chapters.

1.3. Thesis overview

In chapter 2 the theory of the nanowire transmon is explored together with the noise sources it is sensitive to. In chapter 3 the coherence properties of a flux tunable nanowire qubit as well as a gate tunable qubit are measured. The gate tunable qubit is put into a magnetic field and the coherence is measured. The quality factor of the resonators on the chip are also measured. This chapter lays the foundations for operating a qubit in a magnetic field and is the first step to measuring flux noise in a magnetic field. In

chapter 4 the fabrication of airbridges is made compatible with a nanowire. To do this it was necessary to use a lower temperature resist method using grayscale lithography for the airbridges. In chapter 5 all of the previously developed technology is used to measure a flux tunable nanowire transmon in a magnetic field. The echo dephasing time is tracked as a function of magnetic field and sensitivity to flux noise. The flux noise amplitude is measured for both white flux noise and $1/f$ flux noise using two different methods. Finally in chapter 6 noise spectroscopy is performed of the qubit for different magnetic fields and sensitivities to flux noise. Two different ways of measuring the noise PSD are done, which both provide information on the PSD at different frequencies.

2

Theory

The nanowire transmon is a device with rich physics. The nanowire itself is used for the purpose of topological quantum computing and has the possibility of hosting Majorana fermions. A magnetic field additionally opens up a large variety of phenomena. In this chapter the physics of the InAs nanowire is discussed, followed by a simple model of the nanowire transmon. Noise sources affecting the nanowire transmon are elaborated on, such as flux noise and photon shot noise. Finally an overview is presented on some of the microscopic models of flux noise.

2

In this chapter the theory behind the two main parts of the thesis is discussed, the nanowire and the noise affecting transmon qubits. First the focus is set on the superconducting-normal-superconducting (SNS) nanowire Josephson junction. The conduction channels of the supercurrent and the effect of the magnetic field is discussed. However for the experimental part of the thesis only a simple functional form is used. This is presented in both the phase basis as well as in the charge basis in the context of the transmon. The second part of this chapter is the noise. Here different noise types affecting the transmon are discussed such as noise due to charge tunneling in the presence of charge dispersion, photon shot noise due to resonator photons, charge noise coupling to the Josephson energy and finally flux noise. In the final part of this chapter I discuss how this noise affects the transmon.

2.1. SNS nanowire Josephson junction

The nanowire is the Josephson junction in the transmon and provides a non linear inductive element. The nonlinearity allows to limit the Hilbert space to the lowest two levels, the qubit subspace. Contrary to the SIS Josephson junction, where the supercurrent is transported by tunneling through the insulating barrier, the SNS case has the supercurrent transported through conduction channels. In this section the SNS Josephson junction is studied and the mechanism for supercurrent transport is discussed.

The nanowire consists of three sections, the left superconducting part, the normal part and the right superconducting lead. The Hamiltonian of the nanowire can be modeled [44, 45] by a particle in a box,

$$H_{BdG}^{3D} = (H_0 - \mu)\tau_z + H_R\tau_z + H_Z + H_S. \tag{2.2}$$

Here where H_0 describes momentum and confinement potential of the particle as well as the scattering potential, μ is the chemical potential, H_R is the Rashba spin-orbit coupling Hamiltonian H_Z is the Zeeman Hamiltonian due to the magnetic field and H_S is the superconducting Hamiltonian. The momentum Hamiltonian is given by

$$H_0 = \frac{p_x^2 + p_y^2 + p_z^2}{2m} + U_s(z) + V(x, y),$$

where $p_x^2 = -\hbar^2 \frac{\partial}{\partial x}$ describes the momentum, m is the mass, $U_s(z)$ is the scattering term in the normal part of the junction and $V(x, y)$ describes the confinement potential. The second term in the Hamiltonian is the Rashba spin-orbit coupling,

$$H_R = -\alpha p_x \sigma_z + \alpha p_z \sigma_x$$

where α is the strength of the spin-orbit coupling. The Zeeman Hamiltonian is given by

$$H_Z = \frac{1}{2} g\mu_B(\vec{B} \cdot \vec{\sigma}) = \frac{1}{2} g\mu_B(B_x\sigma_x + B_y\sigma_y + B_z\sigma_z)$$

where g is the g-factor and μ_B is the Bohr magneton. Finally the superconducting Hamiltonian is given by

$$H_S = \Delta(z)\tau_x e^{-i\phi(z)\tau_z/2},$$

where $\Delta(z)$ is Δ_0 in the superconducting parts and 0 in the normal part and $\phi(z)$ is ϕ_L in the left lead and ϕ_R in the right lead. In all the previous equations the τ Pauli matrices act on Nambu space (electron/hole space) and the σ Pauli matrices act on spin space.

This Hamiltonian is very general and it is not easy to find solutions to this equation directly, therefore simplifying assumptions are made to make the analysis easier. The Hamiltonian besides the Rashba spin-orbit coupling and the momentum does not depend on x and y, the variables perpendicular to the nanowire axis. Therefore it is possible to separate the wave function into a perpendicular part and a part parallel to the nanowire, $\psi = \psi_\perp(x,y)\psi_\parallel(z)$. The spin-orbit coupling is not taken into account initially in the determination of the perpendicular wavefunction. Substituting this equation back into the Hamiltonian and separating the variables a perpendicular Hamiltonian and a parallel one is obtained, $H_\perp = E_\perp\psi_\perp$ and $H_\parallel = E_\parallel\psi_\parallel$.

The perpendicular Hamiltonian is given by,

$$H_\perp = \frac{p_x^2 + p_y^2}{2m} + V(x,y),$$

which only depends on x and y. The eigenfunctions and eigenenergies of this Hamiltonian depend on the potential, which for the nanowire is not simple. First the nanowire has a hexagonal shape for which there are no simple eigenfunctions and second the addition of the aluminum on top of two of the facets, which causes band bending and causes a highly non-trivial confinement potential. This is exacerbated in the case a gate potential would be added. Therefore it is not feasible to analytically analyze the subband structure of a realistic nanowire. Numerical methods have been developed to analyze these cases [46]. The eigenfunctions and corresponding eigenenergies of the perpendicular Hamiltonian are called subbands. Every subband that has an energy lower than the Fermi energy provides a conduction channel where a particle can provide current transport. The Hamiltonian of the particle in the subband is the parallel Hamiltonian, $H_\parallel$. Without spin-orbit coupling the different subbands do not couple to each other and thus are completely independent of each other,

$$\int\int \psi_\perp^{n\dagger}(x,y) H_{BdG}^{3D} \psi_\perp^m(x,y)\mathrm{d}x\mathrm{d}y = 0$$

where $n \neq m$ and n and m are indices to the different eigenstates. However in the presence of spin-orbit coupling different subbands can couple to each other [44] and the different subbands are not independent anymore. The

subbands that couple are the ones where

$$-\int\int \psi_{\perp}^{n\dagger}(x,y)\alpha p_x \sigma_z \psi_{\perp}^{m}(x,y)\mathrm{d}x\mathrm{d}y \neq 0.$$

For all the other cases it is possible to write down an effective Hamiltonian where the subband information has been integrated out. This 1D Hamiltonian depends only on the z coordinate and for the lowest perpendicular level is

$$H^{1D} = \frac{p_z^2}{2m} - \mu + U_s(z) + E_{\perp}^{0} - \alpha p_z \sigma_x + \frac{1}{2} g \mu_B (\vec{\sigma}\cdot\vec{B}) + \Delta(z)\tau_x e^{-i\phi(z)\tau_z/2},$$

where $E_{\perp}^{0}$ is the energy of the lowest subband. This energy combined with the chemical potential determine whether or not a particular subband is occupied with a quasiparticle and it also determines the Fermi velocity. Every time the chemical potential crosses one of the $E_{\perp}^{n}$ one more conduction channel opens for current transport. This could in principle without any scattering impurities and a match of Fermi velocities in the superconducting part and the normal part lead to quantized conductance. This Hamiltonian has been extensively studied in the context of Majorana fermions [44, 45] with all the terms included and a appropriate linearization of the momentum. However in this case a simplifying assumption is made for the case of zero magnetic field and a junction of zero length. The solution in that case is the well known Andreev bound state (ABS) [47]:

$$E_A = \pm\Delta_0 \sqrt{1 - \tau \sin^2\left(\frac{\hat{\varphi}}{2}\right)}, \tag{2.3}$$

where τ describes the transparency of the channel that is affected by the impurity $U_s(z)$ and φ is the phase difference between the two superconductors. This solution is spin degenerate and is valid even in the case that spin-orbit coupling is included. In a magnetic field the spin degeneracy is lifted and the two different spin states split in energy. For the current transport only the sum of the two quasiparticles in the junction is important. The total supercurrent depends on the phase difference, the number of conduction channels and their transparency.

2.2. Nanowire transmon

The nanowire Josephson junction is shorted with a capacitor making a qubit called a nanowire transmon. The addition of the capacitor makes that the phase operator of the junction is not a good quantum variable anymore. Instead a superposition of the charge and phase variable has to be used. The general Hamiltonian in this case is $H_{NT} = 4E_c\hat{n}^2 + H_{BdG}^{3D}$, where H_{BdG}^{3D} is the Hamiltonian in 2.2 and E_C is the charging energy required to

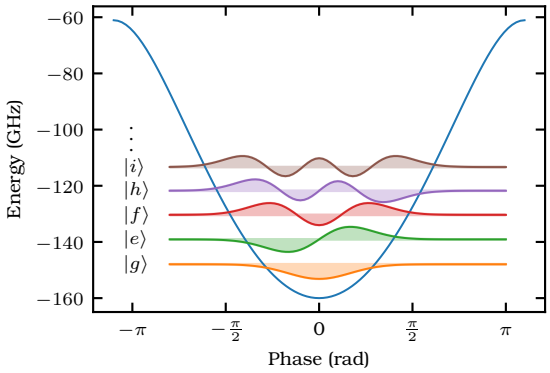

Figure 2.1: The eigenstates and eigenvalues of the short-junction Hamiltonian at zero flux bias.

add a quasiparticle to the capacitor. However if the same assumptions are made as in the previous section and additionally it is assumed that the ABS does not couple to the transmon plasma mode (the transmon charge oscillation), the Hamiltonian can be simplified to

$$H_{NT} = 4E_C\hat{n}^2 - \Delta_0\sqrt{1-\tau\sin^2\left(\frac{\hat{\varphi}}{2}\right)}, \tag{2.4}$$

which is just the combination of the charge and ABS Hamiltonians. This equation cannot be easily analyzed analytically, so a numerical method is required. There are two options for a basis of the numerical analysis, the phase basis or the charge basis. each basis is analyzed individually in an individual section.

Before this analysis is done we point out that there are two ways to change the Hamiltonian and therefore the transition energy of the nanowire transmon. First, the chemical potential of the nanowire can be adjusted with a side or bottom gate and therefore the density of states can be adjusted by allowing more subbands to be below the Fermi energy. Besides this due to universal conductance fluctuations between the chemical potentials required to add another subband below the Fermi level, the conductance changes randomly but reproducably with the side gate potential. This allows for tuning the supercurrent transport through the junction, which is useful in the case that a tunable supercurrent is required.

Second, when an additional nanowire junction is used parallel to the first one between the capacitor plates, the junctions together form a loop. This is called a SQUID loop and the magnetic flux trough this loop has to be quantized. The quantization implies that the relative phase drop can be tuned by applying a small magnetic flux through the SQUID loop. The

difference between the phases across each junction then is, $\varphi_1 - \varphi_2 = \pi\frac{\Phi}{\Phi_0}$, where φ_1 (φ_2) is the phase across junction 1 (2), Φ is the flux bias and Φ_0 is the flux quantum. The flux tunable version of Eqn. 2.4 then becomes

$$H_{NT} = 4E_C\hat{n}^2 - \Delta_0\sqrt{1-\tau_1\sin^2\left(\frac{\hat{\varphi}}{2}\right)} - \Delta_0\sqrt{1-\tau_2\sin^2\left(\frac{\hat{\varphi}+\pi\frac{\Phi}{\Phi_0}}{2}\right)}. \tag{2.5}$$

This equation forms the fundamentals for the future analysis on the nanowire transmon, which will be done in the phase basis in the next section (Sec. 2.2.1) and in the charge basis in Sec. 2.2.2.

2.2.1. Phase basis

The analysis of Eqn. 2.4 in the charge basis requires the charging term to be written in the phase basis, in which case it takes the form $\hat{n} = -i\frac{\mathrm{d}}{\mathrm{d}\varphi}$. The derivative is not possible to be directly implemented in a numerical calculation and therefore it needs to be discretized. This procedure is called tight binding and is an approximation to the derivative. A simplified explanation of the procedure applicable to this case starts with dividing the phase basis up in N different sites. Every site has a different phase, φ_i, and this vector forms a basis. The more sites are added the more accurate the approximation is. The square of the charge operator can be discretized to

$$E_c\frac{\mathrm{d}^2}{\mathrm{d}\varphi^2} \approx E_c\left(\frac{2}{a^2}\varphi_i - \frac{1}{a^2}\varphi_{i-1} - \frac{1}{a^2}\varphi_{i+1}\right),$$

where $a = 2\pi/N$. This equation shows that the charge operator couples the different phase sites to each other. The nanowire term does not depend on charge and stays diagonal,

$$V_{NW}(\varphi_i) = \Delta_0\sqrt{1-\tau_1\sin^2\left(\frac{\hat{\varphi}_i}{2}\right)} - \Delta_0\sqrt{1-\tau_2\sin^2\left(\frac{\hat{\varphi}_i+\pi\frac{\Phi}{\Phi_0}}{2}\right)}. \tag{2.6}$$

The final Hamiltonian is the sum of these two discretized terms, with $-E_c\frac{1}{a^2}$ on the off diagonals and $E_c\frac{2}{a^2} + V_{NW}(\varphi_i)$ on the diagonal. Since this Hamiltonian only has the diagonal terms and the first off-diagonal term as a non-zero entry in the matrix, it is relatively easy for computers to diagonalize it.

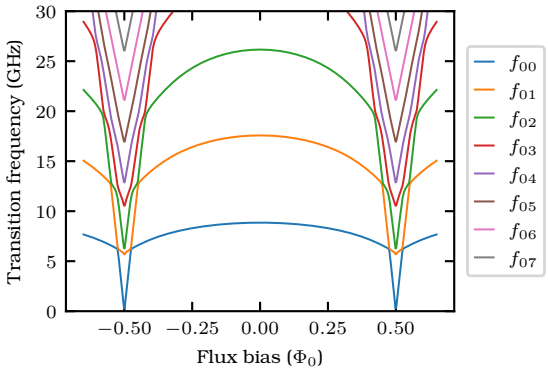

Figure 2.2: Transition frequencies of the nanowire transmon. At the sweetspot the spectrum is an anharmonic oscillator with a negative anharmonicity. Around a flux bias of $0.5\Phi_0$ the nanowire potential is a double well, explaining the linear fluxonium like behavior around that point.

In matrix form the equation becomes,

$$H = \begin{bmatrix} \frac{2}{a^2}E_c + V_{NW}(\varphi_0) & -\frac{1}{a^2}E_c & 0 & \cdots & 0 \\ -\frac{1}{a^2}E_c & \frac{2}{a^2}E_c + V_{NW}(\varphi_1) & -\frac{1}{a^2}E_c & \cdots & 0 \\ 0 & -\frac{1}{a^2}E_c & \frac{2}{a^2}E_c + V_{NW}(\varphi_2) & \cdots & 0 \\ \vdots & \vdots & \vdots & \ddots & \vdots \\ 0 & 0 & 0 & \cdots & \frac{2}{a^2}E_c + V_{NW}(\varphi_N) \end{bmatrix}. \tag{2.7}$$

The fact that only the first off-diagonal entries of the matrix are non zero means that it is fast to calculate the eigenstates and eigenenergies of the Hamiltonian. This is done for this equation and shown in Fig. 2.1. The spectrum of the nanowire transmon is similar to that of a conventional SIS transmon with a reduced anharmonicity. In this cast the anharmonicity is about -132 MHz. Around half a flux quantum of flux bias the potential is radically different to a conventional SIS transmon. The potential is a double well potential and at the sweetspot the wells are of equal depth. The degeneracy of the states dwelling in each well is lifted by a finite tunneling barrier between them. The lower the barrier the wider the sweetspot is in terms of flux bias. In practice the two eigenstates are the odd and even superposition of the particle being in either potential well, where the even superposition state has the lower energy. Around a small deviation away from this sweetspot one of the wells will linearly increase in energy compared to the other well. This behavior is very similar to the behavior in a fluxonium qubit.

2.2.2. Charge basis

The other natural choice of basis for analyzing the nanowire transmon Hamiltonian of Eq. 2.4 is the charge basis. The charging term is naturally in the charge basis, so only the Josephson junction term has to be transformed into the charge basis. Before transforming the junction potential, first the attention is turned to the SIS Josephson potential, which is just a cosine. Transforming this into the charge basis, the following relation is obtained [48]

$$E_J \cos(\varphi) = \frac{E_J}{2} \sum_n \left(|n\rangle\langle n+1| + |n\rangle\langle n-1| \right).$$

This relation motivates to expand the nanowire potential into a Fourier series, since it is known how the cosine is transformed to the charge basis. The expansion of the Andreev energy of Eq. 2.3 is,

$$V_{ABS}(\varphi) = \sum_m E_J^m(T) \cos(m\varphi).$$

Here the m-th Josephson energy term is for $m > 1$

$$E_J^m(T) = \Delta_0 \frac{2}{\pi} \int_0^\pi \cos(m\varphi) \sqrt{1 - T \sin^2\left(\frac{\varphi}{2}\right)} \mathrm{d}\varphi$$

while for $m = 0$ the expression is half of this. This integral can be evaluated in terms of a recurrence relation,

$$E_J^m(T) = \frac{TDelta_0}{2\pi m} B(m-1) - \frac{TDelta_0}{2\pi m} B(m+1), \tag{2.8}$$

where $B(m)$ is given by another recurrence relation,

$$B(m) = \frac{3-2m}{2m-1} B(m-2) + \frac{T-2}{T} \frac{4m-4}{2m-1} B(m-1) \tag{2.9}$$

$$B(0) = \mathrm{K}\left(\sqrt{T}\right) \tag{2.10}$$

$$B(1) = \frac{2}{T} \mathrm{E}\left(\sqrt{T}\right) + \frac{T-2}{T} \mathrm{K}\left(\sqrt{T}\right). \tag{2.11}$$

Here, $\mathrm{K}\left(\sqrt{T}\right)$ is the complete elliptic function of the first kind and $\mathrm{E}\left(\sqrt{T}\right)$ is the complete elliptic function of the second kind. The first term in the Fourier series is $E_J^0 = 2\Delta/\pi \mathrm{E}\left(\sqrt{T}\right)$. The first few terms are expressed in a table for convenience (Tab. 2.1). The Fourier series approximation to this equation is plotted in Fig. 2.3.

The m-th cosine term describes cooper pair tunneling through the junction of m cooper pairs,

$$E_J^m \cos(m\varphi) = \frac{E_J^m}{2} \sum_n \left(|n\rangle\langle n+m| + |n\rangle\langle n-m| \right).$$

m	E_J^m
0	$2\Delta_0/\pi \mathrm{E}\left(\sqrt{T}\right)$
1	$\frac{\Delta_0}{3\pi T}\left[(8-4T)\mathrm{E}\left(\sqrt{T}\right)+8\mathrm{K}\left(\sqrt{T}\right)(T-1)\right]$
2	$\frac{\Delta_0}{15\pi T^2}\left[(-4T^2+64T-64)\mathrm{E}\left(\sqrt{T}\right)+32\mathrm{K}\left(\sqrt{T}\right)(T-1)(T-2)\right]$
3	$\frac{\Delta_0}{105\pi T^3}\left[(-12T^3+536T^2-1536T+1024)\mathrm{E}\left(\sqrt{T}\right)+ 216\mathrm{K}\left(\sqrt{T}\right)(T-1)\left(T^2-\frac{128}{27}T+\frac{128}{27}\right)\right]$

Table 2.1: Coefficients of the first few terms in the Fourier series of the short junction potential.

The matrix form of the Hamiltonian in the charge basis then can be represented as,

$$H=\begin{bmatrix} 4E_c & -\frac{1}{2}E_J^1 & -\frac{1}{2}E_J^2 & \cdots & -\frac{1}{2}E_J^k \\ -\frac{1}{2}E_J^1 & 4E_c & -\frac{1}{2}E_J^2 & \cdots & -\frac{1}{2}E_J^{k-1} \\ -\frac{1}{2}E_J^2 & -\frac{1}{2}E_J^1 & 4E_c & \cdots & -\frac{1}{2}E_J^{k-2} \\ \vdots & \vdots & \vdots & \ddots & \vdots \\ -\frac{1}{2}E_J^k & -\frac{1}{2}E_J^{k-1} & -\frac{1}{2}E_J^{k-2} & \cdots & 4E_c \end{bmatrix}. \tag{2.12}$$

Contrary to the case of the phase basis (Eq. 2.7) this matrix does not have zeros. This makes finding the eigenvalues and eigenstates a computationally expensive task in the case a large number of charges is needed.

2.3. Noise in superconducting qubits

Noise in qubits causes dephasing and decoherence causing the qubit to lose its quantum information. Noise causes dephasing when the qubit couples to a noisy environment. This implies that the effect of the noise on the decoherence can be reduced by either reducing the coupling to the qubit or reducing the noisy environment. Reducing the noise can be difficult in practice. Generally the environment is not known exactly and even when it is known it can be difficult to improve the noise characteristics. On the other hand it is usually easier to limit the impact of a noisy environment on the dephasing of a qubit. One such example is the evolution of the cooper pair box to the transmon. The cooper pair box is sensitive to charge noise, which is dominant for this qubit. This requires tuning of the charge offset parameter to a charge sweetspot. Contrastingly, the transmon is exponentially insensitive to charge noise and tuning the charge offset to a sweetspot is no longer required [30]. This method is the simplest to improve the coherence of the qubit, but it is not always possible. Reducing the sensitivity to a noisy environment usually also reduces the controllability of the qubit.

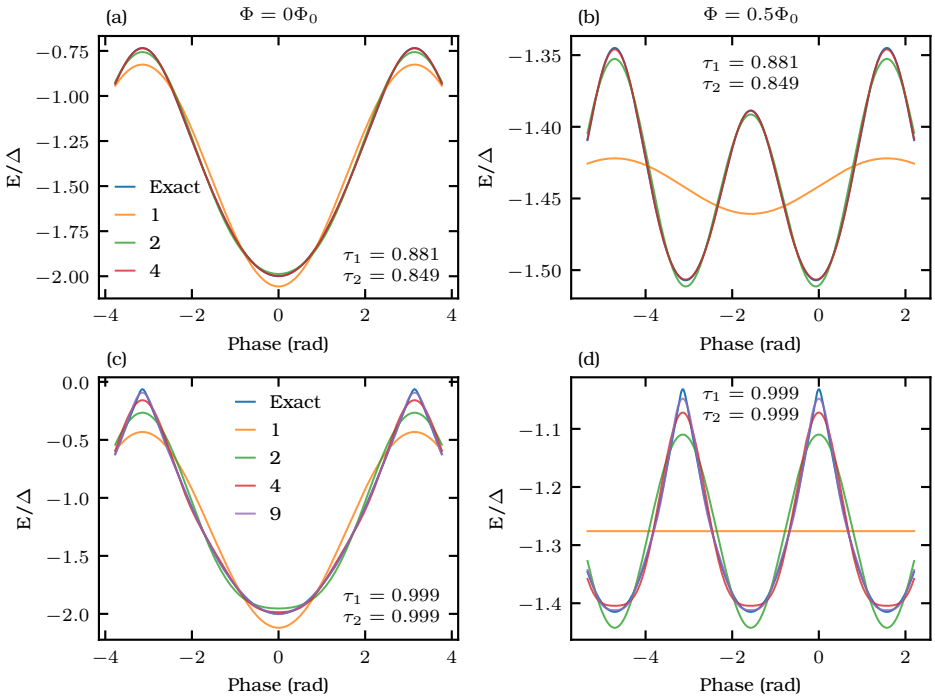

Figure 2.3: Fourier Series approximation of the short junction potential with two junctions in a SQUID-loop configuration. (a) The top row shows the potential to the best fit of the data in Ch. 6 at the sweetspot at 0 ϕ_0 and in (b) for 0.5 Φ_0 with $\tau_1 = 0.881$ and $\tau_2 = 0.849$. (c) The bottom row for an equal transparent junction of $\tau_1 = \tau_2 = 0.999$ at 0 Φ_0 and (d) 0.5 Φ_0

This is exemplified by the fluxonium, where the controllability relative to the transmon is sacrificed by limiting the $|0\rangle$ to $|1\rangle$ transition dipole moment [22, 23]. This allows the fluxonium to be less impacted by T_1 relaxation due to dielectric losses. However the control of the qubit is more complicated requiring higher levels to aid in the $|0\rangle$ to $|1\rangle$ driving [49–51]. Other protected qubits have been devised with a similar trade-off, such as Josephson rhombus qubits [52], nanowire $\cos(2\phi)$ potential similar to the rhombus [53] or the 0-π qubit [25–28]. These schemes all have in common that the computational states $|0\rangle$ and $|1\rangle$ are disjoint in the phase basis. This means that they do not have a dipole moment between the computational states. Other schemes that are for example based on topological protection do not necessarily have this limitation. Therefore some proposals have been made on how to make such a qubit. For example the Majorana fermion could make a topologically protected qubit [38, 54]. However to this date no intrinsically topologically protected qubit has been made. Since mitigation

of noise directly is difficult, other schemes have been devised to encode many unprotected qubits into protected qubits. These schemes are known as quantum error correction and is currently the most promising way to a practical quantum computer.

2.4. Dephasing and decoherence

Whenever a qubit can be controlled by a particular type of control knob, the environment can also cause dephasing via the same knob. On the other hand not having that control knob also means that noise associated with that knob cannot affect that qubit. These control knobs can for example be flux or side gate voltage in the case of the nanowire transmon. However there are more noise sources that affect the nanowire transmon, such as quasiparticle tunneling in the presence of charge dispersion (Sec. 2.5.1), photon shot noise (Sec. 2.5.3) due to thermal photons in the readout resonator, E_J noise (Sec. 2.5.4) due to charges coupling to the nanowire Josephson junction and flux noise (Sec. 2.5.2) in the case of a flux tunable transmon.

If the noise is weakly coupled to the qubit the decoherence due to these noise sources can be expressed with the coherence integral,

$$\langle \varphi^2(t) \rangle = (2\pi\tau)^2 \sum_{\lambda} \left(\frac{\partial f_{01}}{\partial \lambda} \right)^2 \int S_\lambda(f) W(f) \mathrm{d}f. \tag{2.13}$$

Here, .The dephasing is measured as an exponential decay, $\exp(-\langle \varphi^2(t) \rangle)$.

where $\partial f_{01}/\partial \lambda$ is the sensitivity to the noise, S_λ is the associated noise power spectral density (PSD) and W is the filter function that is defined by the sequence measuring the dephasing. This formula suggests three mechanisms for reducing the dephasing experienced by the qubit. Transmons at zero flux bias have a first order insensitivity to flux noise, where the derivative of the frequency with respect to flux is zero. It is desirable to have the qubit operating at a frequency as close as possible to this sweetspot, because the dephasing due to flux noise here is zero (at least in first order). The second way the dephasing can be extended is by changing the filter function. This changes to what part of the noise spectrum the qubit is sensitive. In general, more π pulses means that the sensitivity to noise is shifted towards higher frequencies, this is for example done in CPMG or UDD [55]. If there is $1/\mathrm{f}$ noise or another type of noise that is peaked towards low frequencies, the coherence time can be extended. However for white noise there is no gain. The final way the dephasing can be reduced is by attenuating the noise power spectral density, which is one of the goals of this research for the flux noise.

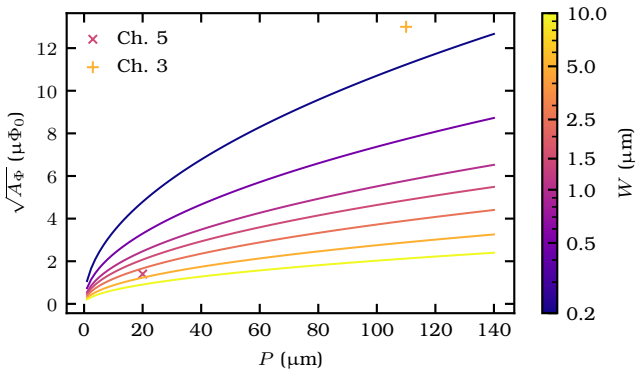

Figure 2.4: The flux noise amplitude for a SQUID loop of various geometries. The devices of Ch. 3 and Ch. 5 are shown as a point. The theory has one free variable, $m^2\sigma$, that determines the overall amplitude of the flux noise. In this figure the value in [17] is used. The amplitude of the device in Ch. 3 is higher and the device of Ch. 5 is lower than that in [17].

2.5. Noise sources for the nanowire transmon

In this section each of the different noise sources that are of consideration for the nanowire transmon will be discussed and elaborated on.

2.5.1. Charge dispersion

The transmon is not completely insensitive to charge fluctuations. The transmon eigenstates split into two different energies dependent on the charge offset and the quasiparticle parity of the transmon island. The splitting of the eigenenergies of the lowest states of the transmon can be approximated by [30],

$$\epsilon_m \approx (-1)^m E_C \frac{2^{4m+5}}{m!}\sqrt{\frac{2}{\pi}}\left(\frac{E_J}{2E_C}\right)^{\frac{2m+3}{4}} \exp\left[-\sqrt{\frac{8E_J}{E_C}}\right] \tag{2.14}$$

Here, m is the m-th transmon level. The charge dispersion as seen from this equation increases with the transmon level exponentially and decreases exponentially with the root of the E_J/E_C ratio. Since this is only one degree of freedom and couples strongly to the transmon Eq. 2.13 does not apply. The random process required for dephasing in this case is the random event of the charge parity tunneling. This changes the transmon frequency by $\epsilon_1 - \epsilon_0$ and the corresponding dephasing rate in the strong coupling limit only depends on, and is equal to, the quasiparticle tunneling rate. In experiments this is typically in the millisecond range [56] and is thus not the limiting factor dephasing in the experiments of this thesis, which is in the range

of 5 µs to 20 µs. In experiment the way charge dispersion shows up is by having a bistable f_{01} transition frequency. This in turn causes a double beating when doing a Ramsey type experiment (Ch. 3).

2.5.2. Flux noise

The exact microscopic origin of flux noise is presently unknown. However starting from a spinful two level fluctuator it is possible to derive some qualities of the flux noise. The two level fluctuator has a spin that produces a magnetic field and couples to the SQUID-loop. The coupling is strongest on top of the superconductor of the SQUID-loop, where the supercurrent is the largest. Away from the surface of the superconductor the coupling falls off rapidly and any spinful two-level system can be ignored for the analysis of flux noise. This means that only the only the spins on the surface of the superconductor have to be taken into account. This fact can be seen by considering the coupling mechanism of the spin with the SQUID-loop. When the transmon is operated away from the sweetspot, a persistent supercurrent is flowing around the SQUID-loop. This current produces a local magnetic field that is strongest on the surface and couples to the spin affecting the two-level system. The opposite also happens, when the spin changes state, the supercurrent in the SQUID-loop is also affected. This coupling can be seen as a mutual inductive coupling. The noise that the randomly flipping ensemble of spins imparts on the SQUID-loop can be expressed as [13, 17]

$$\langle \Phi^2 \rangle = \frac{1}{3} m^2 \sigma P \int \left(\frac{B(x)}{I} \right)^2 \mathrm{d}x, \tag{2.15}$$

where m is the magnetic moment of the spin, σ is the density of spin, P is the perimeter of the SQUID-loop and B is the magnetic field due to the SQUID-loop current, I. The superconductor of the SQUID-loop can be modeled assuming a current density and the equation can be expressed as,

$$\langle \Phi^2 \rangle = \frac{\mu_0^2}{3\pi} m^2 \sigma \frac{P}{2\pi W} \left(\ln(2bW/\lambda^2) + e - 1 \right), \tag{2.16}$$

where b is the thickness of the superconductor and W the width and λ the penetration depth of the superconductor.

2.5.3. Photon shot noise

When a (thermal) photon is in the readout resonator of the qubit, the qubit dephases due to photon shot noise. The random entry and exit times cause the qubit to dephase. The stark shift associated with a photon being present in the resonator is $\Delta = 2\eta\chi\bar{n}$, where χ is the dispersive shift, $\bar{n}$ is the average photon number and $\eta = \kappa^2/(\kappa^2 + 4\chi^2)$. Where κ is the relaxation rate of the

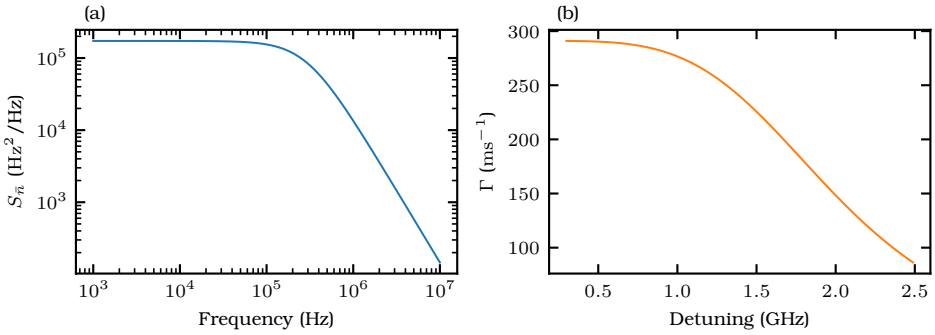

Figure 2.5: Photon shot noise experienced by a qubit coupled to a resonator. (a) Photon shot noise PSD for parameters corresponding to the qubit in Ch. 5. (b) Dephasing rate due to photon shot noise as a function of detuning for parameters corresponding to the qubit in Ch. 5.

resonator. The dephasing rate associated to the photon shot noise is [57]

$$\Gamma = \frac{4\eta\chi^2\bar{n}}{\kappa} \tag{2.17}$$

and the noise PSD of is

$$S_{\bar{n}} = \frac{8\chi^2\eta\bar{n}\kappa}{(\kappa^2+\omega^2)}. \tag{2.18}$$

The noise PSD follows a Lorentzian distribution with a cutoff frequency of κ. Below this frequency the PSD is basically flat, making an echo measurement of the T_2 the same value as a Ramsey measurement. Since this is the most prevalent type of white noise, measuring an equal Ramsey and Echo pure dephasing time is a sign that the qubit is limited by photon shot noise. Alternatively the higher levels of the transmon due to the anharmonicity are affected differently allowing to distinguish photon shot noise from other types of noise by measuring the dephasing of higher levels [58].

The noise PSD and dephasing rate due to photon shot noise is shown in Fig. 2.5. The parameters chosen for the plot correspond to the device in Ch. 5. Here, the anharmonicity, $\alpha = -138$ MHz, the coupling, $g = 64.7$ MHz, the resonator coupling rate, $\kappa = f_r/Q$, with $f_r = 6.401$ GHz and $Q = 22000$, and $\bar{n} = 1$.

The dispersive shift also depends on the qubit frequency in the following way [30, 57],

$$\chi = -\frac{g^2}{\Delta(1+\Delta/\alpha)}, \tag{2.19}$$

where α is the anharmonicity, g is the resonator qubit coupling and Δ is the resonator qubit detuning. This means that the noise PSD and dephasing depend on the detuning between the resonator and qubit. This dependence

on frequency is further explored in Ch. 5 in the context of excess dephasing at the sweetspot, which is getting closer in frequency to the resonator due to a magnetic field.

2.5.4. Josephson energy noise

The nanowire Josephson junction can be tuned by applying a voltage to a side gate (Ch. 3). This means that noise can also couple via this degree of freedom and cause dephasing. The noise can be either strongly coupled, which results in a bi-stable transition frequency, or it can be weakly coupled. The strongly coupled case is extensively studied in Ch. 3. The weakly coupled case causes dephasing that can be measured with an echo or a Ramsey sequence. Since this type of noise does not couple via flux, the dephasing contribution will be constant as a function of flux. This allows to distinguish this noise type from flux noise. The charge two-level systems that generate this type of noise turn out to fluctuate at relatively low rates affecting the Ramsey times dominantly and not the Echo dephasing times. The relatively low Ramsey dephasing time compared to the echo dephasing time of Sec. 5.2 are likely to be caused by this type of noise.

Assuming the frequency can be approximated by $f_{01} \approx \sqrt{8E_J E_C}$, which is the case away from half a flux quantum, the sensitivity to charge noise is,

$$\frac{\partial f_{01}}{\partial E_J} = \sqrt{\frac{2E_C}{E_J}}. \tag{2.20}$$

This shows that the higher the E_J/E_C ratio the lower the sensitivity to charge noise. It is thus beneficial to operate the qubit at a high frequency because this simultaneously decreases the sensitivity to charge noise and increases the sensitivity to flux noise. Flux noise being the quantity of interest for this thesis. The higher levels of the transmon are affected in basically the same way as the $|0\rangle$ to $|1\rangle$ transition, making it possible to distinguish weakly coupled charge noise with photon shot noise by looking at the higher levels.

2.6. Microscopic origin of flux noise

Over the years many proposals have been made to explain the microscopic origin of flux noise, here a few are discussed. Most of the mechanisms have in common that there is a spinful electron that can switch between two spin states with a wide variety of tunnelling rates that produce a $1/f$ noise PSD. A list is shown with some of the models that have been put forward together with their references.

Model 1 Perhaps the simplest model [59] is a free electron that is situated on the surface of the superconductor of the SQUID. This electron is stuck in a charge trap with a fixed magnetic field orientation. By

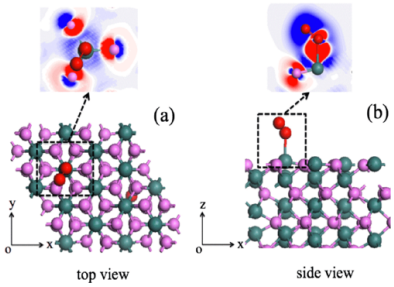

Figure 2.6: Magnetic oxygen site on AlO of the Josephson junction. Image adopted from [20]

hopping to a different charge trap with a different but fixed field orientation, noise is produced. By adding defects to this model a good agreement with the $1/f$ noise is observed in simulations.

Model 2 This model [60] instead of charge traps focuses on the two magnetic states of a dangling bond that arises in the interface between a semiconductor and its semiconductor oxide. The spin of the dangling bond can flip its state in the presence of a phonon, which produces a wide range of flipping rates. The dangling bond can be modeled as a tunneling two level system (TLS) with an energy barrier, this can be visualized by a double well potential (Fig. 2.7). The well has a tunneling barrier and an offset produced by a small local magnetic field. The model produces a $1/f^{\alpha}$ noise PSD, where in the high temperature limit $\alpha = 1$, in the mid temperature limit $\alpha = 1.2 - 1.5$ and the noise is exponentially suppressed in the case of the low temperature limit. The high temperature limit is defined when kT is larger than the largest transition energy of the TLS, the low energy limit by the lowest energy TLS and the mid limit is in between these. For realistic parameters a flux noise amplitude is found of $1(\mu\Phi_0)^2/Hz$ at 1 Hz, which is in the range of most of the experimental studies [11, 12, 17, 36, 42].

Model 3 This model [18] starts from a criticism of the previous two models. Where they find that the number of thermally activated TLSs is too high for the temperature of the device. They rule out vortices and nuclear spins as the source of flux noise. However electron spins on top of the superconductor or insulator can produce flux noise in the presence of the RKKY interaction. The RKKY interaction couples these spins with conduction electrons of the metal. They show that the spectrum is white for low frequencies ($f \ll f_W$) and proportional to $1/f$ for high frequencies ($f \gg f_W$). where the cut-off frequency, $f_W = \mathcal{D}/W^2$, depends on the width, W of the SQUID loop and the diffusion constant, $\mathcal{D}$. For typical values of $\mathcal{D}$ and W this cut-off is in the range of $10^2 - 10^3$ Hz.

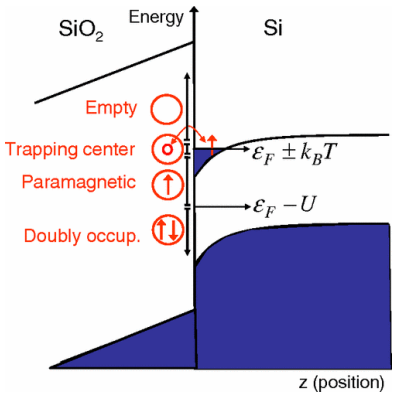

Figure 2.7: Dangling bonds on the ubiquitous interface between silicon and silicon dioxide. Image reproduced from [60]

Model 4 Absorbed oxygen molecules [20] have a magnetic moment and can produce flux noise at low temperatures. An image of an absorbed oxygen molecule on the surface of aluminum oxide is shown in Fig. 2.6. Their density functional theory calculations show a 1 f noise PSD with a ferromagnetic type of interaction between the oxygen molecules. They propose that removing these molecules can reduce the flux noise.

Model 5 When a sapphire substrate is used there are magnetic surface states that might be responsible for flux noise [61]. They show that some surface absorbents may also contribute to these magnetic states. It is proposed that by chemically passivating the surface especially with NH_2 the flux noise can be reduced. The non-magnetic NH_2 substitutes for magnetic sites such as an OH group.

Model 6 States at the interface between the metal and insulator can become magnetic and produce flux noise [21]. Simulations of these so called metal induced gap states produce a noise PSD that agrees with the measured data.

Model 7 A measurement [15] of flux noise showing that oxygen molecules are be responsible for flux noise. The oxygen was identified using x-ray spectroscopy techniques. By passivating the surface with NH_3 the flux noise power was reduces across the measured spectrum. Additionally preparing the sample in an ultra-high vacuum improved the noise as well.

Model 8 Ising spin glass model [62] can produce magnetization noise that is observed as flux noise. They show that it has the same $1/T$ temperature dependence as observed in experiment and they predict that the noise is maximum at the spin-glass transition temperature.

Model 9 Flux noise can be due to hyperfine interactions [63] with the nuclear spins and the electron spins of a molecule. The nuclear spins provide a path for the relaxation of the electron spin together with the hyperfine interaction. They find a $1/T_1$ distribution of relaxation rates producing a $1/f$ noise PSD. The model predicts that the relaxation rates would be significantly lower for superconductors with low nuclear magnetic moments. For example by substituting niobium for zinc or lead they expect a reduction in the amount of flux noise of 25 and 5 respectively.

3

cQED in a magnetic field

We present an experimental study of flux- and gate-tunable nanowire transmons with state-of-the-art relaxation time allowing quantitative extraction of flux and charge noise coupling to the Josephson energy. We evidence coherence sweetspots for charge, tuned by voltage on a proximal side-gate, where first order sensitivity to switching two-level systems and background $1/f$ noise is minimized. We next investigate the evolution of a nanowire transmon in parallel magnetic field up to 70 mT, the upper bound set by the closing of the induced gap. Several features observed in the field dependence of qubit energy relaxation and dephasing times are not fully understood. Using nanowires with a thinner, partially covering Al shell will enable operation of these circuits up to 0.5 T, a regime relevant for topological quantum computation and other applications.

This chapter has been published in *Phys. Rev. Lett.* **120**, 100502 (2018) [42].

3.1. introduction

Circuit quantum electrodynamics (cQED) offers unprecedented control over coupled atomic and photonic degrees of freedom in engineerable, microscale superconducting circuits [29, 64]. It relies crucially on the dissipationless nonlinearity of the Josephson effect between two weakly coupled superconductors [65]. The Josephson junction (JJ), usually implemented as a superconductor–insulator–superconductor (SIS) tunnel barrier, allows the realization of anharmonic oscillators that can be operated in the quantum regime and used as qubits [66]. Circuit QED has found applications in many areas, including scalable quantum computation [67], quantum optics [68], quantum foundations [69], and quantum measurement and control [70]. So far, cQED has been limited by standard SIS JJs based on aluminum and its oxide to fields < 10 mT, the critical field of bulk aluminum [71]. However, interesting applications such as coupling cQED devices to polarized electron-spin ensembles serving as quantum memories [72] and using qubits as charge-parity detectors in Majorana based topological quantum computation [37, 38] require fields of ~ 0.5 T. In such fields, more fundamental effects such as topological phase transitions [73] and degeneracy-lifting of the Andreev bound states which underlie the Josephson effect [74–77] can be studied. Entering this important regime for cQED requires the use of field-compatible superconductors and non-standard JJs [78–82].

To date, qubits in cQED architectures have been realized using various JJs: the ubiquitous SIS tunnel junction [66], atomic break junctions [83] and semiconductor weak-link nanowire junctions [39–41]. Nanowire qubits are of particular interest because of potential compatibility with high magnetic field, the voltage tunability of the JJ and the overlap with other technologies of interest, including nanowire-based transistors and lasers [84, 85]. Nanowire qubits are compatible with the transmon geometry [30], the most widely used in cQED, and have been realized in flux and voltage tunable variants [39, 40]. Nanowire transmons have reached echo dephasing times (T_2^{Echo}) up to 10 μs, and been used to implement two-qubit gates [41]. So far, the use of Al as a superconductor for the larger scale cQED elements [40, 41] and short coherence times [39] have inhibited study of the coherence of these circuits in a magnetic field.

In this Letter, we present an experimental study of decoherence processes affecting flux- and gate- tunable transmons based on nanowire Al-InAs-Al junctions, both at zero and applied magnetic field. As is typical for conventional transmons, we observe the coupling of flux noise to the Josephson energy in a split-junction device. We estimate the flux noise spectrum from measurements of qubit dephasing with respect to flux sensitivty. Crucially, taking advantage of a state-of-the-art qubit relaxation time, we can also evidence the coupling of charge noise directly to the Josephson energy. This noise takes the form of switching two-level systems and a $1/f$ background. Tuning the voltage sidegate, we demonstrate coherence sweetspots

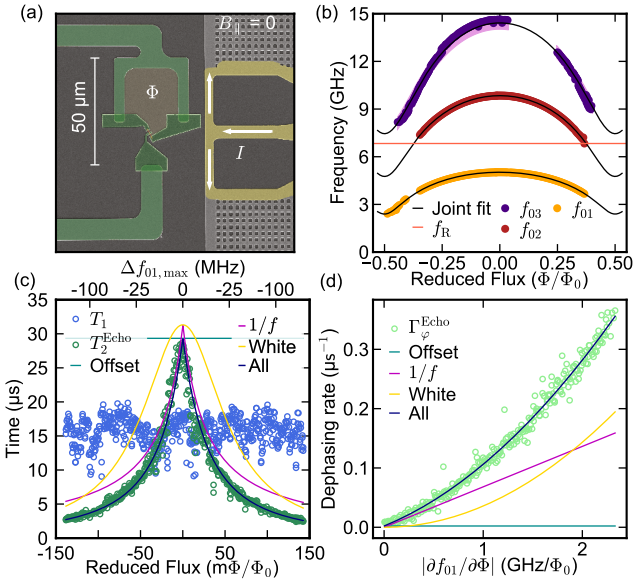

Figure 3.1: Characterization of flux-tunable split-junction qubit at $B_\parallel = 0$. (a) False-colored SEM micrograph of the SQUID-loop area. The current I in the flux-bias line (yellow) threads a magnetic flux Φ through the SQUID loop (green), tuning $E_J(\Phi)$. (b) The joint fit (black) of the first three transitions (orange, dark red and purple symbols) versus flux yields the transmission probability and the induced gap of each junction. (c) T_1 (blue) limits T_2^{Echo} (green) at the qubit flux sweetspot $\Phi = 0$. A fit to T_2^{Echo} that includes the measured T_1 limit allows extraction of flux-independent (cyan), $1/f$ (pink) and white-noise (gold) contributions to the dephasing. T_2^* is typically below 4 μs. Top axis indicates the frequency detuning from the flux sweetspot. (d) $\Gamma_\phi^{\text{Echo}}$ vs flux sensitivity, extracted from (c), with the different contributions to the fit.

at points where the first-order qubit sensitivity to charge is minimized. Paralleling the method used to study flux noise, we measure qubit dephasing as a function of this sensitivity to extract properties of the charge noise spectrum. Finally, we investigate the evolution of the qubit relaxation and dephasing as a function of in-plane magnetic field, up to the closing of the induced superconducting gap at 70 mT. Several features of the field dependence are not understood, calling for further experimental and theoretical investigation.

3.2. Fabrication

Device fabrication combines widely used NbTiN-based recipes for microscale features [86–88] with nanowire etching and contacting recipes. The

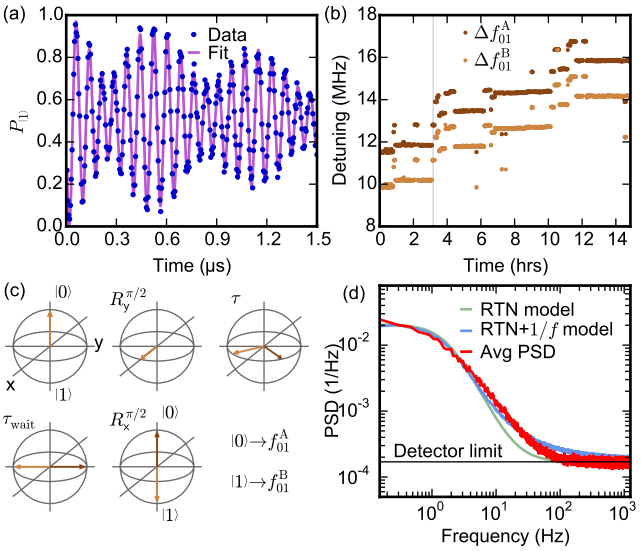

Figure 3.2: Frequency stability analysis of the flux-tunable qubit at the flux sweetspot and at $B_{\parallel} = 0$. (a) Ramsey experiment (dots) with artificial detuning (12 MHz). The strongly coupled TLS yields a beating between two decaying sinusoids (purple, $\tau^{A} = 2.2$ μs and $\tau^{B} = 2.0$ μs). (b) The extracted detunings of repeated Ramsey experiments show a constant frequency spacing and drift of the center frequency. The gray vertical line indicates the trace in (a). (c) Pulse sequence of the Ramsey-type TLS-state detection scheme. The free evolution time τ is chosen as $\tau_{\text{wait}} = 1/2\Delta f$ for maximal contrast. (d) The PSD (red) of the TLS is computed from qubit state traces obtained by monitoring the qubit frequency real-time using the pulse sequence in (c). The PSD is fitted using RTN models with (blue) and without (green) $1/f$ noise.

nanowires have an InAs core and an epitaxially grown Al shell that induces a hard superconducting gap [80, 89–91]. A home-made image recognition software defines etch- and contacting masks [92, 93] of the individual wires. After defining the superconductor-semiconductor-superconductor (SNS) junction by wet-etching a 200 nm segment of the 30 nm thick shell, the wires are contacted with NbTiN. Standard cQED control and measurement schemes [64, 94] are used to probe the qubits that are coupled to the common feedline via dedicated readout resonators [95].

3.3. Flux-tunable nanowire transmon

Following previous work [39], we first extract information about the SNS junctions by studying the spectrum of the flux-tunable, split-junction device. A current I in the flux-bias line changes the magnetic flux Φ through the

SQUID loop [Fig. 3.1(a)], controlling the superconducting phase difference $\hat{\delta}$ between the transmon islands. This tunes E_J, given in the short-junction, single-channel limit by Andreev bound states with transmission probability T_i and energy $V_i(\phi_i) = -\Delta_i\sqrt{1 - T_i \sin^2(\phi_i/2)}$. Employing the bound-state model in the split-junction Cooper-pair-box Hamiltonian, $H = 4E_C\hat{N}^2 + V_A(\hat{\delta}) + V_B(2\pi\Phi/\Phi_0 - \hat{\delta})$, yields good agreement with the observed spectrum [Fig. 3.1(b)] [39]. The best-fit values of the induced gaps $\Delta_A/h = 46 \pm 4$ GHz and $\Delta_B/h = 38.5 \pm 0.9$ GHz are close to the 43 GHz of bulk Al, suggesting that the shell fully proximitizes the nanowire [91].

We investigate the flux noise of the split-junction qubit by measuring coherence times as a function of flux offset. T_2^{Echo} is T_1 limited in a range around ~ 20 MHz around the flux sweetspot [Fig. 3.1(c)]. The noise is quantified [12, 92, 96, 97] using a second-order polynomial fit of the echo dephasing rate $\Gamma_\phi^{\text{Echo}} = 1/T_\phi^{\text{Echo}} = 1/T_2^{\text{Echo}} - 1/(2T_1)$ versus $|\partial f_{01}/\partial\Phi|$. We extract a white-noise contribution to the double-sided spectral density $S_{\Phi,\text{white}} = (60\ \text{n}\Phi_0/\sqrt{\text{Hz}})^2$ (from the quadratic term), a $1/f$ noise amplitude $\sqrt{A_\Phi} = 13.0\ \mu\Phi_0$ where $S_{\Phi,1/\text{f}} = A_\Phi/|f|$ (from the linear term), and a 2 ms^{-1} offset. This value of $\sqrt{A_\Phi}$ is on the high side of the range observed for flux-tunable SIS transmons [12, 15, 97, 98]. White flux noise has not been reported in these more standard systems.

3.3.1. Strongly coupled two-level system

Ramsey measurements reveal a beating pattern of two exponentially decaying sinusoids [Fig. 3.2(a)], indicating a switching of the qubit frequency f_{01} between two values. This is the reason for not reporting Ramsey coherence times (T_2^*) in Fig. 3.1. The observed frequency difference $\Delta f = f_{01}^{\text{A}} - f_{01}^{\text{B}} = 1.6$ MHz is nearly constant overnight [Fig. 3.2(b)]. Because Δf is constant and much larger than the calculated charge dispersion [30] of 200 kHz, we conclude that the switching is due to a TLS coupling directly to the nanowire E_J. Furthermore, we attribute the correlated jumps in the two frequencies to other TLSs switching on slower timescales. Using the qubit, we monitor the fast TLS in real time using a single-shot Ramsey-based pulse sequence tailored for Δf [Fig. 3.2(c)] [56]. The double-sided power spectral density (PSD) of the TLS state time evolution is well explained by an asymmetric random telegraph noise (RTN) with characteristic switching times of 100 ms [Fig. 3.2(d)] [92]. Better agreement with the measured PSD is achieved by taking $1/f$ noise into account [92]. The switching of f_{01} between multiple values can be observed in several qubits. In addition, the Δf of gatemons was observed to depend on V_G [92]. This dependence indicates that the TLSs are charge traps in the vicinity of the junction, influencing the transmission probabilities of the Andreev bound states.

3.4. Voltage-tunable nanowire transmon

We now study the spectrum of a gatemon as a function of V_G [Fig. 3.3(a-d)]. Tuning V_G changes f_{01} by altering the T_i, hence altering E_J. The anharmonicity $\alpha = f_{02} - 2f_{01}$ (f_{02} the transition from the ground to the second-excited state) indicates that E_J is dominated by two channels [92]. The tuning is repeatable upon small excursions (1-2 V), except for isolated deviations which we attribute to charge traps changing state. These changes — some are reproducible, others are stochastic — lead to jumps in f_{01}. Because the gatemon-resonator pair is well described by the dressed-state picture [64], f_{01} is easily found after a jump by measuring f_R and calculating f_{01}.

The strong V_G dependence of gatemon dephasing times allows a quantitative study of the effect of charge noise. Figure 3.3(e) clearly shows the presence of charge sweetspots, where the sensitivity $\partial f_{01}/\partial V_G$ vanishes and the dephasing times correspondingly peak. The ratio $T_\phi^{\mathrm{Echo}}/T_\phi^* \sim 8$ observed on and off the sweetspots (data not shown) indicates that the dominant dephasing noise is $1/f$ like [96]. From a linear fit of $\Gamma_\phi^{\mathrm{Echo}}$ against $|\partial f_{01}/\partial V_G|$ [12, 92, 96, 97], we extract a voltage-noise-independent offset of 66 ms^{-1} and a $1/f$ voltage noise amplitude $\sqrt{A_V} = 26\ \mu\mathrm{V}$, where $S_{V,1/f} = A_V/|f|$. The extracted noise clearly exceeds the noise floor of the biasing circuit [92], indicating that on-chip charge noise dominates over electrical noise on the gate.

3.4.1. Applying a parallel magnetic field

We now apply a $B_\parallel$ to the same gatemon. We focus on the gatemon because flux-tunable devices experience fluctuating f_{01} due to imperfect alignment and limited stability of $B_\parallel$. To disentangle $B_\parallel$ and V_G contributions, the gatemon is placed at the same V_G sweetspot for each $B_\parallel$ value. We attribute the observed monotonic decrease in f_{01} with $B_\parallel$ [Fig. 3.4(a)] to a reduced superconducting gap induced in the nanowire junction, $\Delta(B_\parallel) = \Delta(0)\sqrt{1-(B_\parallel/B_c)^2}$ [99]. The bulk of the cQED chip exhibits little change due to the high parallel critical field (B_c) of the NbTiN film [92]. We approximate the Andreev bound state energy with $V_i(\phi_i, B_\parallel) = -\Delta(B_\parallel)\sqrt{1 - T_i \sin^2(\phi_i/2)}$. The Hamiltonian $H = 4E_C\hat{N}^2 + V_A(\hat{\delta}, B_\parallel) + V_B(\hat{\delta}, B_\parallel)$ is fitted to f_{01} and $f_{02}/2$, fixing $\Delta(0)$ to the bulk Al gap and E_C to the value obtained for the split-junction device. The best-fit parameters $T_{A,B} = 0.95$, 0.62 and $B_c = 83.9$ mT match f_{01} and $f_{02}/2$ with an average of the absolute residuals of 12.6 MHz. The extracted B_c of the Al shell is similar to other measurements of wires from this growth batch [89]. Because $B_\parallel$ is not collinear with the nanowires, the B_c of different qubits varies between 50 and 90 mT, roughly correlating with the nanowire-to-$B_\parallel$ alignment [92]. The B_c values stay constant during one cooldown and vary by ~ 5 % between cooldowns, provided the sample orientation is kept fixed. Explaining the data by flux penetration of an extended junction (Fraunhofer model) [99] provides neither qualitative nor quantitative agreement.

Finally, we investigate the gatemon coherence properties in $B_\parallel$. At each $B_\parallel$ value, we extract T_1 and T_2^{Echo} [Fig. 3.4(b)] in a V_G sweep through a sweetspot. Before quasiparticle tunneling [56] dominates T_1 at 70 mT, we find a good match with a model including the Purcell effect [100] and a background field-dependent quality factor Q_b: $1/T_1(f_{01}, B_\parallel) = 1/T_1^{\mathrm{P}}(f_{01}) + 2\pi f_{01}/Q_\mathrm{b}(B_\parallel)$. Here, Q_b decreases from $4.6 \cdot 10^5$ at $B_\parallel < 6$ mT to $2.7 \cdot 10^5$ at $B_\parallel > 10$ mT, as shown in Fig. 3.4(c) inset. A similar step-like trend is observed in the internal quality factors of most resonators [92]. We surmise that the drop in Q_b is due to the Al wirebonds turning normal. Future experiments will use NbTiN air-bridges to hopefully eliminate the effect. The dip in T_1 at 45 mT is reproducible but hysteretic. We do not understand its origin.

The field dependence of qubit dephasing is comparatively less understood. Tracking the V_G sweetspot, we observe that T_2^{Echo} is not T_1 limited above 20 mT [Fig. 3.4(b)]. The corresponding increase in $\Gamma_\phi^{\mathrm{Echo}}$ [Fig. 3.4(e)] is reproduced when repeating the procedure of Fig. 3.3(f) at various $B_\parallel$ [Fig. 3.4(d)]. The gradual decrease in $\sqrt{A_\mathrm{V}}$ and the shift of the minimum of $\Gamma_\phi^{\mathrm{Echo}}$ away from $\partial f_{01}/\partial V_\mathrm{G} = 0$ with $B_\parallel$ are also not understood. One possible explanation for these three effects may be that the sensitivity to the dominant on-chip charge noise differs from $\partial f_{01}/\partial V_\mathrm{G}$ away from $B_\parallel = 0$ around the one sweetspot that we tracked. Studying the dephasing around multiple V_G sweetspots (not possible with this gatemon and cooldown) may allow to test this hypothesis in the future.

3.5. Conclusion

In summary, we have first characterized flux- and gate-tunable nanowire transmons with state-of-the-art T_1 at $B_\parallel = 0$, focusing on quantitative extraction of flux and charge noise coupling to the Josephson energy. We have next investigated the evolution of a gatemon in $B_\parallel$ up to 70 mT, the upper bound set by the closing of the induced gap. Several features of the T_1 and T_2^{Echo} dependence in $B_\parallel$ are not understood yet, inviting further theoretical and experimental investigation.

Our immediate next experiments will further the study and development of nanowire transmons in field. Using a persistent current mode for the solenoid providing $B_\parallel$, we aim to investigate the spectrum and coherence of flux-tunable transmons in $B_\parallel$. This could yield further insight into the microscopic origin of $1/f$ flux noise [98]. Studying the temperature and $B_\parallel$ behavior of the observed charge traps may lead to further understanding of their nature. Nanowires with a thinner, partial shell (10 nm), which have already been shown to induce a hard superconducting gap [101], will allow operation of nanowire transmons up to 0.5 T, reaching the relevant field range for attractive new applications of cQED.

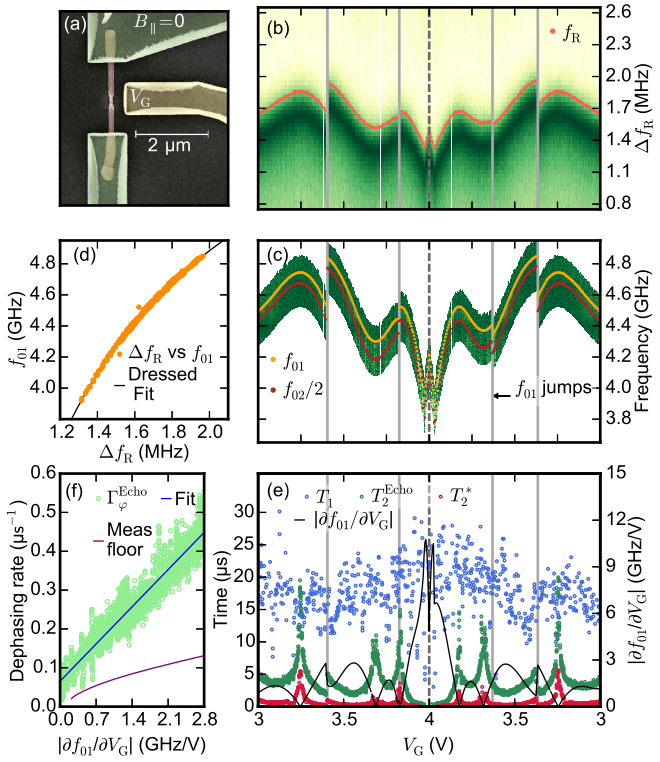

Figure 3.3: Gatemon characterization at $B_\parallel = 0$. (a) False-colored SEM micrograph of the nanowire Josephson junction (light red) with a side-gate (yellow) enabling V_G tuning. (b) Deviation of f_R, Δf_R, from the bare resonator frequency $f_{bare} = 6.732$ GHz for a triangle sweep in V_G. Note the change in direction of the V_G sweep, indicated by the dashed line. On return to the same V_G, f_R is roughly reproduced. (c) f_{01} versus V_G. Random, but sometimes reproducible jumps of f_{01} occur (at light gray lines). (d) Plot of f_{01} against f_R (orange dots) and dressed state fit (black) with coupling strength $g/2\pi = 60.8$ MHz, allowing a prediction of f_{01}. (e) Gatemon T_1 (blue), T_2^{Echo} (green) and T_2^* (red) versus V_G. Both T_2^{Echo} and T_2^* are strongly correlated with the V_G sensitivity (black). (f) Γ_φ^{Echo} against V_G sensitivity, extracted from (e). The fitted $1/f$ noise (blue) is above the setup-imposed dephasing limit (purple), indicating additional on-chip noise.

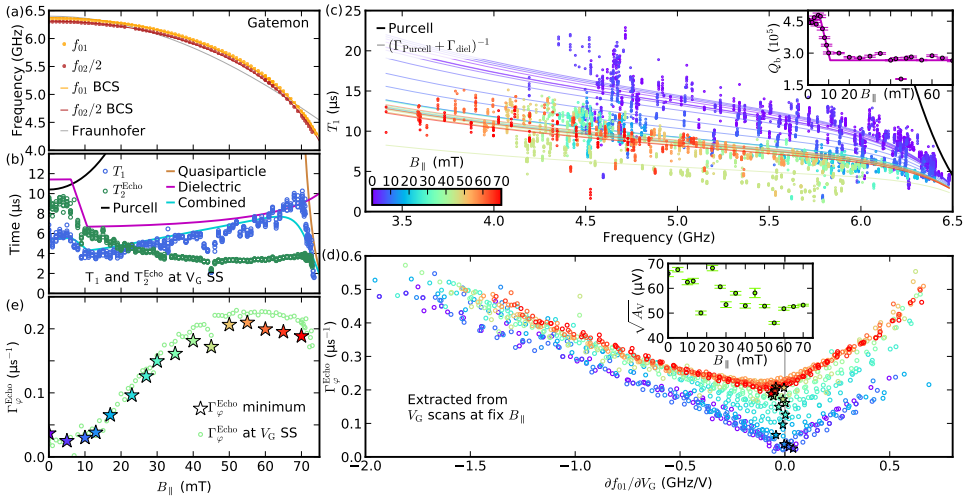

Figure 3.4: Evolution of the gatemon of Fig. 3.3 in $B_\parallel$. (a) Qubit f_{01} and $f_{02}/2$ (orange and red) are described by a closing BCS gap (curves) with $B_c = 83.9\,\mathrm{mT}$. (b) At each value of $B_\parallel$, the gatemon is tuned to a V_G sweet-spot to measure T_1 and T_2^{Echo} (blue and green). At low $B_\parallel$ (f_{01} near the resonator), T_1 is mainly Purcell-limited (red). At $B_\parallel$ close to B_c the superconducting gap becomes so weak that quasiparticle tunneling dominates T_1 (brown, assumes 100 mK effective quasiparticle temperature). In-between, the T_1 evolution can be attributed to a step in Q_b, see below. (c) T_1 versus frequency at different $B_\parallel$. Accounting for T_1^P, we fit a Q_b at each $B_\parallel$ (inset), finding a step-like drop from 6 to 10 mT. (d) Keeping $B_\parallel$ fixed [same color scale as (c)], V_G scans are performed to extract Γ_ϕ^{Echo}, similar to Fig. 3.3(e). Inset: averaged extracted $1/f$ voltage noise amplitude. (e) Pure dephasing rates at V_G sweetspots versus $B_\parallel$ from data in (b) and (d). Stars are the interpolated minimal dephasing rates from (d).

3.6. Supplemental information

This supplement provides experimental details and additional data supporting the claims in the main text.

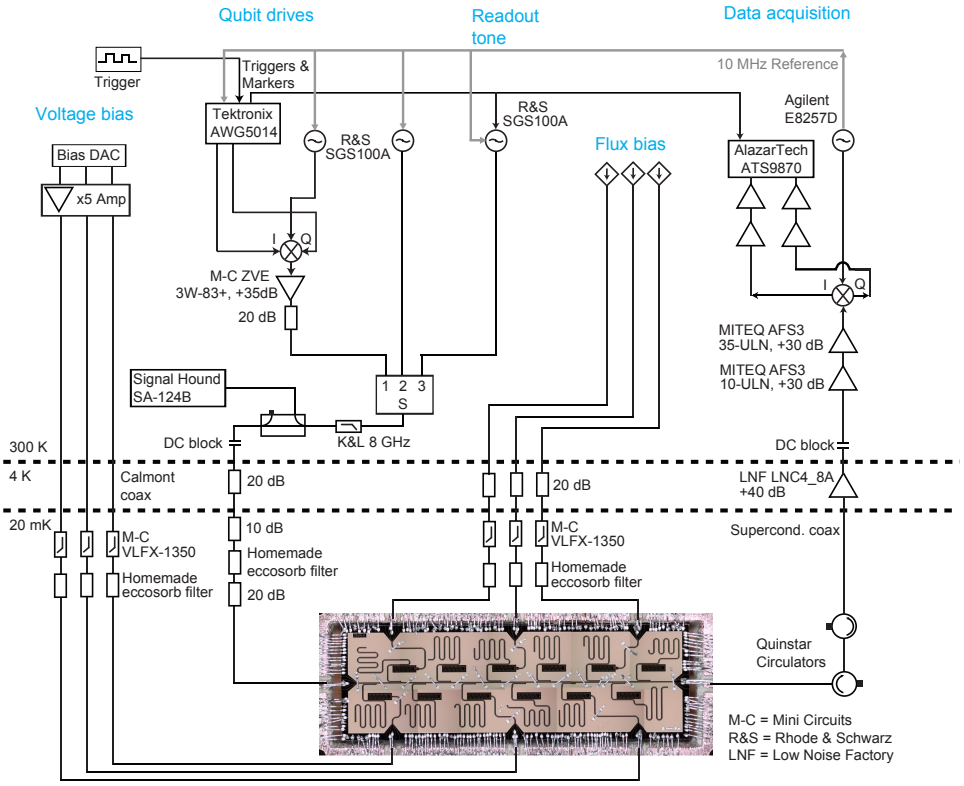

Figure 3.5: Optical micrograph of the cQED chip and schematic of the experiment showing microwave and dc connectivity in- and outside the dilution refrigerator. Silver features crossing the feedline and bias lines are on-chip wire bonds.

3.6.1. Experimental Setup

Measurements were performed in a variety of experimental conditions, differing in degrees of magnetic and radiation shielding. The data shown in Figs. 1, 2 and 3.7 are taken with the sample in a box that provides radiation and magnetic shielding. The shielding consists of two layers of Cryophy, a superconducting Al shield and a copper cup coated on the inside with a mixture of silicon carbide and Stycast for infrared shielding [102]. The data in other figures are taken with the sample in a copper box, only surrounded by a copper shield coated with the mixture. Using superconducting shields

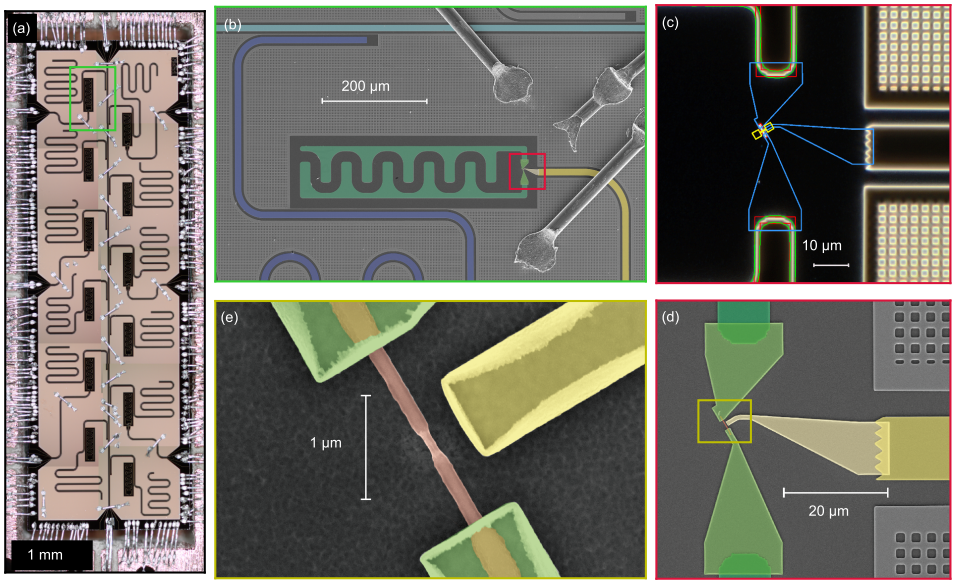

Figure 3.6: Optical and SEM micrographs (added false color) of the sample used for Figs. 1 and 4. (a) Optical micrograph of the twelve-qubit test chip wirebonded to a PCB. (b) SEM micrograph zoom-in view on a gatemon qubit (green interdigitated capacitor plates). Readout resonators (blue) connect to a common feedline (light blue). The sidegate (yellow) allows for V_G tuning of the qubit. (c) After deterministic deposition of the NW, an optical dark field image is taken. The image recognition software automatically detects contours of wire and leads (light green) and generates an etch mask (bright yellow) and a contact mask (light blue). (d) SEM micrograph of the same region as (c) after NW etch and contact deposition. (e) SEM micrograph zoom-in of the region highlighted in (d). The InAs NW (red) is contacted with NbTiN and has a segment of the Al shell etched near the center.

or passive magnetic shielding was not possible in this situation as this would conflict with the external magnetic field applied. The coaxial cables carrying voltages, currents and microwave signals are connected to the chip that is mounted on a printed circuit board (PCB) using non-magnetic SMP connectors. The detailed microwave setup is shown in Fig. 3.5. Care was taken to only use non-magnetic brass screws in proximity to sample and solenoid.

The magnetic field is generated by a single-axis, cryogen-free, compensated solenoid (American Magnetics, Inc.) with a current-to-field conversion factor 51.6 mA/T (max. 2 T), driven by a Keithley 2200-20-5 programmable power supply. This solenoid does not have a persistent current switch.

The dc current for flux biasing the split-junction devices is provided by

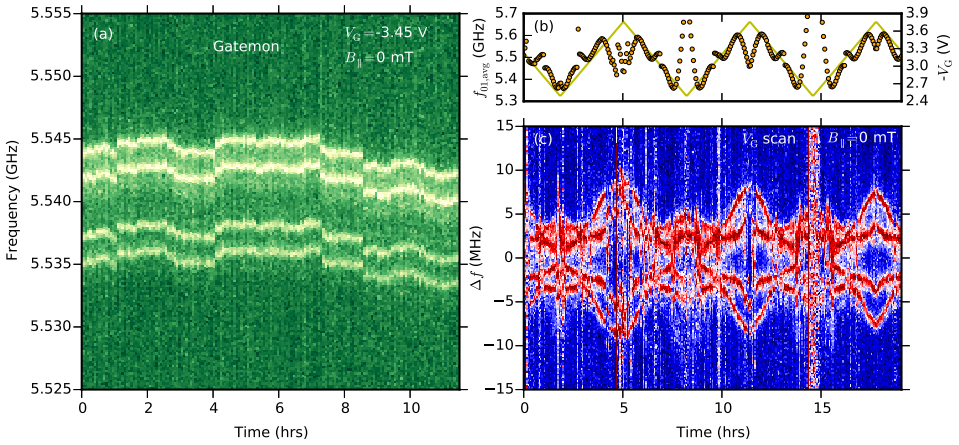

Figure 3.7: Frequency stability of a gatemon. (a) Repetitions of pulsed qubit spectroscopy scans show four distinct, drifting frequencies between which the qubit switches. (b) Average f_{01} (orange dots) and the triangle profile of V_G (yellow line) of the scan in (c). (c) Pulsed qubit spectroscopy while sweeping V_G in a triangle profile [shown in (b)]. Scans are centered around the extracted average f_{01}. The difference between the distinct f_{01} values changes with V_G, indicating a sensitivity of the TLSs to the electrostatic environment of the junction.

home-built low-noise current sources mounted in a TU Delft IVVI-DAC2 rack. The voltage to bias the gatemons (provided by DACs of the IVVI rack, amplified with a 5 V/V battery-driven amplifier) is low-pass filtered (through Calmont coaxial cables, cutoff frequency 100 MHz, Mini Circuits VLFX 1050 and a home-made, absorptive eccosorb filter) before arriving at the sample.

Microwave tones for qubit control and readout are generated, modulated and combined at room temperature. They are coupled to the chip through the common feedline. Filtering and attenuation at different temperature stages (see Fig. 3.5) suppresses unwanted photon population in the readout resonators. The readout line wiring is similar to [103].

3.6.2. Fabrication procedure

Standard cQED fabrication techniques are used to pattern ground plane, coplanar waveguide structures and qubit capacitor islands [88]. Then, the NWs are deterministically placed in each qubit junction area using a nanomanipulator. The InAs NWs have an epitaxially grown Al shell [89, 104] (core diameter 65 nm, shell thickness 30 nm). Using a PMMA etch mask, a 200 nm window is etched into the Al shell. This defines the N section of the SNS junction. The wet etchant used (Transene D, 12 s at 50 °C) is selective enough that no damage to the InAs core can be detected in scanning elec-

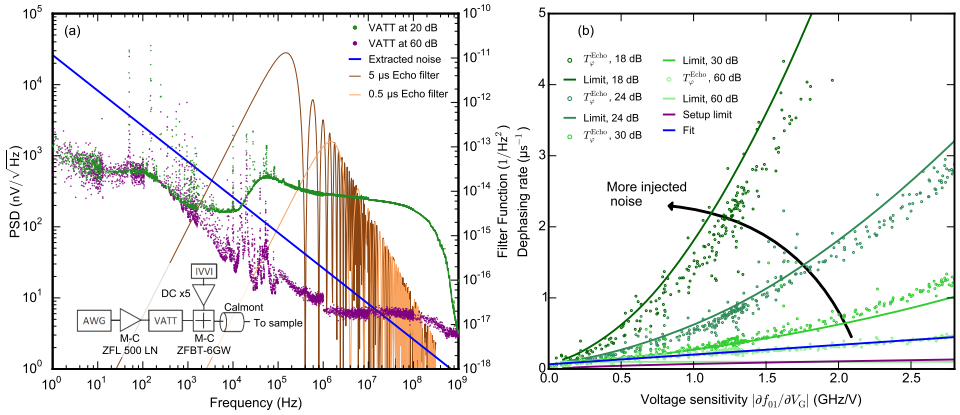

Figure 3.8: Channel configuration of the gatemon presented in Fig. 3. (a) Extracted α versus V_G. The dashed line indicates the change in direction of the V_G sweep. Markers and continuous gray lines indicate jumps in f_{01}. (b) Anharmonicity versus f_{01}. Jumps in f_{01} are indicated by the markers [same as in (a)]. Curves indicate the anharmonicity as calculated from a full Hamiltonian diagonalization for a single channel (blue), two equally transmitting channels (orange) and the SIS case (green).

tron microscope (SEM) micrographs [Fig. 3.6(e)]. Some SEM micrographs reveal residues of Al in the junction area of the NWs. We could not establish a correlation between qubit T_1 or T_2^{Echo} and such residues.

To contact the Al shell, a gentle in-situ argon plasma etch is first used to remove the aluminum oxide. Then, the NbTiN contacts to capacitor plates and sidegates are sputtered. Although a bilayer of resist is used, the formation of standing edges could not be prevented. Note that using the metal contacts of already contacted NWs as an etch mask did not produce reliably working qubits.

On-chip Al wirebonds are used to suppress slot-line modes. These are added as the sample is also wirebonded to a standard PCB. In the future work, we will employ airbridges made of NbTiN [105], both for this purpose and to ensure compatibility with higher magnetic fields.

3.6.3. Image recognition software

The advantage of top-down fabrication common in cQED is compromised for NW transmons: a bottom-up fabrication approach is required for individual NWs. Each NW has a different position with respect to the corresponding qubit leads, hence etch mask and contacts (including sidegate) must be individually designed for each qubit. To reduce the turnaround time, we wrote software to automatically generate these masks using optical dark field images [compare Fig. 3.6(c)] [93].

Setup	Qbit	f_R [GHz]	f_{01} [GHz]	T_1 [μs]	T_2^{Echo} [μs]	B_c [mT]	∢NW	Comment
Mag. Shields	C	6.08	7.08	15-20	15-20	-	-	2 freqs, 10-15 μs T_2^*, Single
	H	6.618	6.815	7-10	6-8	-	-	Single-junction, ungated
	J	6.832	4.9 (SS)	10-20	30 (SS)	-	-	Flux-tunable, Figs. 1, 2
	K	6.93	5.68	2.5-3	1.7-2.1	-	-	Single-junction, ungated
Mag. Shields	1	6.41	7.62	5-5	~1	-	-	Gatemon
	4	6.20	4.48	7-10	~4	-	-	Single-junction, ungated
	5	6.30	5.4-5.8	4-7	1-2	-	-	Gatemon, Fig. 3.7
	6	6.42	7.62 (SS)	4-5	~1 (SS)	-	-	Flux tunable
Solenoid &Shield	1	5.88	7.06	~7	~2	-	15 °	Gatemon
	4	6.21	5.49	~4.5	~4	60/59/60	50°	Single-junction, ungated
	5	6.31	5.08	3-4	2-3	53	60°	Gatemon
	6	6.42	7.22	6-10	~8 (SS)	95/95	5°	Flux tunable
	9	6.74	4-6.5	10-30	~20 (SS)	86/82	10	Gatemon, Figs. 3, 4, 3.8

Table 3.1: Summary of qubit parameters and performance [typical, where indicated on sweetspots (SS)] in different cooldowns. Only working qubits are listed. The two chips investigated have 12 qubits each. Qubits F, G, I, 2, 3, 10 and 11 do not work for fabrication reasons (e.g., displaced NW). It is not clear why the other qubits do not work. Cooldown-to-cooldown reproducibility of f_{01}, T_1 and T_2^{Echo} is limited due to the strong influence of surface absorbents on the NW junction [106].

Our image recognition software employs a suite of filtering procedures and feature detection algorithms to reliably design etch and contact masks. First, the image is low-pass filtered with a Gaussian point spread function. This reduces the sensitivity to possible dirt in the junction area. The image is then binarised using Otsu's thresholding method [107]. To further reduce the chance of picking up uninteresting features (such as the holes in the ground plane) and increase the stability of the procedure, a morphological filter combines adjacent areas [108]. The Canny edge detection algorithm finds all contours present in the image. These are compared to the known shape of the leads to select the best match (green) [109]. The scaling, rotation and offset of the image are determined using a Hough transformation and fitting the analytical shape of the leads to the extracted contours (red) [110]. This allows the definition of a coordinate system. The NW is then determined as the contour between the leads enclosing the largest area. The orientation and position of the NW are determined by the smallest rectangle encompassing the NW contour. This allows correct detection of the NW in ~ 93 % of the cases. The position and orientation information is used to create the pattern file for the etch windows (yellow), and to place and connect (light blue) contacting regions predefined with respect to leads and wire using a distance minimizing routine. These contours are used to generate the pattern file for the contact mask.

The performance of the image recognition software is sufficient for our purpose. The NW width is only 130 nm, well below the diffraction limit (500 nm) and the effective width of the wire in the image (~ 1 µm). The achieved rms error in sidegate placement is 140 nm.

3.6.4. Gatemon frequency splitting

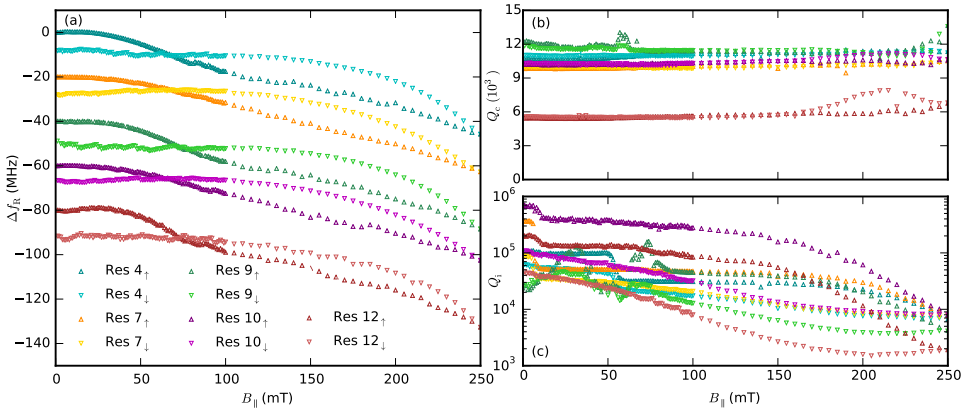

Figure 3.9: Voltage noise injection and coherence time limit. (a) Measured upper limit to the PSD of the IVVI bias circuit noise (purple) and PSD with additionally injected AWG noise (green), measured after the BiasTee. The extracted noise experienced by the gatemon (blue) exceeds the setup noise floor. Echo filter functions (brown) indicate the frequencies at which the qubit is most sensitive to noise. Inset: Schematic of the noise injection circuit. (b) Computed dephasing rate limits (curves) agree well with measured dephasing rates (points) when the injected noise is dominant. If no noise is injected (purple), another noise source becomes dominant [blue, same fit curve as in Fig. 3(e)].

We have observed the splitting of the qubit transition frequency due to strongly coupled TLSs influencing E_J also in gatemons. Figure 3.7(a) shows repeated pulsed spectroscopy scans taken at fixed $V_G = -3.45$ V. Four distinct, drifting values of f_{01} with semi-constant spacings are clearly visible. A possible explanation of the four frequencies is the strong coupling of two TLSs to E_J. A background of many weakly coupled TLSs causes the drift in the center frequency.

The difference between the values of f_{01} depends on the applied V_G [Figs. 3.7(b,c)]. Pulsed spectroscopy scans are performed while V_G is swept up and down. For each scan, the multiple values of f_{01} are extracted and their average is set to $\Delta f = 0$ MHz. The frequency spacing between the peaks changes with V_G. We therefore interpret the V_G-sensitive TLSs that are influencing E_J to be charge traps in the vicinity of the NW junction. The frequencies do not return to the same value upon return to the same V_G. The drift of the center frequency made it challenging to setup a reliable frequency state measurement (compare Fig. 2). Hence, we were not able to estimate the PSD of these TLSs.

3.6.5. PSD of the TLS

The strong coupling of a TLS to the flux-tunable, split junction qubit [Fig. 2(a,b)] allows detailed characterization of the TLS dynamics in real time via Ramsey based time-domain measurements [Fig. 2(c,d)] [56]. By monitoring the frequency state of the qubit every $\Delta t = 400\ \mu$s for 6.6 s, we track the TLS state $x_{\mathrm{TLS}}(t)$ over time. The PSDs $\mathcal{S}(f)$ of such traces, given as

$$\mathcal{S}(f) = \frac{(\Delta t)^2}{T}\left|\sum_{n=1}^{N} x_{\mathrm{TLS}}(n\cdot\Delta t)e^{-i2\pi f n}\right|^2, \tag{3.21}$$

are averaged to get an estimation of the TLS PSD. The TLS PSD can be approximated by an asymmetric random telegraph noise (RTN) model

$$\mathcal{S}(f) = \frac{8F^2\Gamma_\uparrow\Gamma_\downarrow}{(\Gamma_\uparrow+\Gamma_\downarrow)((\Gamma_\uparrow+\Gamma_\downarrow)^2+(2\pi f)^2)} + (1-F^2)\Delta t, \tag{3.22}$$

where $\Gamma_\uparrow = 10.5\ \mathrm{s}^{-1}$ and $\Gamma_\downarrow = 0.57\ \mathrm{s}^{-1}$ are the two switching rates and $F = 0.76$ is the detector fidelity [Fig. 2(d)].

Better agreement with the observed data can be achieved by taking the influence of $1/f$ noise into account [Fig. 2(d)]. Given the switching rates $\Gamma_{\uparrow,\downarrow}$, the noise-free TLS traces are simulated using a Markov chain approach. Subsequently, $1/f$ frequency noise that is generated by spectrally filtering white noise is superimposed on the TLS traces. The action of the Ramsey experiment with evolution time τ_{wait} is thresholded to obtain the detector signal $d_{\mathrm{TLS}}(n\cdot\Delta t) = \mathrm{sign}(\sin(2\pi\cdot f_{\mathrm{n}}\tau_{\mathrm{wait}}))$ at the n-th time step, at which the frequency of the TLS is f_{n}. The detector fidelity (defined as $F = 1-\varepsilon_0-\varepsilon_1$, where $\varepsilon_{0,1}$ are the detection error probabilities for the $|0\rangle$ and $|1\rangle$ states) is taken into account by probabilistically flipping the thresholded values. PSDs of many such traces are calculated using Eq. (3.21) and their average is compared to the experimental PSD. The experimental parameters of f_{01} difference $\Delta f = 1.683$ MHz, $\tau_{\mathrm{wait}} = 297$ ns and $\Delta t = 400\ \mu$s are used for the simulations. Switching rates $\Gamma_\uparrow = 9.25\ \mathrm{s}^{-1}$ and $\Gamma_\downarrow = 0.5\ \mathrm{s}^{-1}$ and fidelity $F = 0.76$ agree well with the values found with the asymmetric RTN model [Eq. (3.22)]. The additional $1/f$ noise has an amplitude $\sqrt{A_{1/f}} = 102\ \mathrm{kHz}/\sqrt{\mathrm{Hz}}$ at 1 Hz. The resulting PSD matches the experimentally obtained PSD better than just an asymmetric RTN curve. This suggests that $1/f$ noise plays an important role.

3.6.6. Channels contributing to the Josephson energy

Studying the anharmonicity of the gatemon in Fig. 3 allows us to estimate the number of channels contributing to E_{J} (Fig. 3.8). Performing a full Hamiltonian diagonalization using the values of E_{C} and Δ obtained from the split-junction device shows that $|\alpha|$ is reduced for E_{J} given by a short junction model in comparison to the SIS case [Fig. 3.8(b)]. Thus, at a fixed

f_{01}, α depends on the number of channels. As it is not possible to reliably extract the T_i at each value of V_G (the gatemon does not allow for φ control), we only present the α for a single channel [blue curve in Fig. 3.8(b)] and a toy model with two channels of equal T_i (orange curve). The model with equal T_i sets an upper limit to $|\alpha|$. We can therefore conclude that main contribution to the transmission comes from two channels. It can not be excluded that more, weakly transmitting channels also participate.

3.6.7. Noise PSD extraction from dephasing rates

The qubits can be used to probe the noise on the control knobs λ they are sensitive to. In the presence of noise in λ, the $\Gamma_\phi^{\text{Echo}}$ increases with increasing sensitivity to λ, $D_\lambda = |\partial f_{01}/\partial\lambda|$. By performing a quadratic fit,

$$\Gamma_\phi^{\text{Echo}} = aD_\lambda^2 + bD_\lambda + c, \tag{3.23}$$

we can extract the relevant noise parameters [12, 96, 97]. These are the D_λ-independent offset c, a $1/f$ noise contribution linear in D_λ and a white noise contribution quadratic in D_λ. We quantify the $1/f$ PSD by

$$\sqrt{A_\lambda} = \frac{b}{2\pi\sqrt{\ln(2)}}. \tag{3.24}$$

The white noise is quantified by

$$S_{W,\lambda} = \frac{a}{\pi^2}.$$

Using the qubits as detectors to measure the noise they are subjected to therefore reveals information about the direct environment of the qubits (Figs. 1 and 3). This is needed to exclude that our control electronics limits the performance of the qubits (Fig. 3.8).

3.6.8. Coherence limitation given a noise PSD

It is also possible to measure the noise generated by the control electronics and from that calculate a limit on the qubit dephasing time [96]. To do so, the PSD of λ is measured at room temperature. The induced mean-squared phase-noise $\langle\phi^2(t)\rangle$ at a time t is then given as

$$\langle\phi^2(t)\rangle = (2\pi)^2\left(\frac{\partial f_{01}}{\partial\lambda}\right)^2\int_0^{f_{01}} S_\lambda(f)W(f)\mathrm{d}f, \tag{3.25}$$

where $W(f)$ is the filter function of the echo sequence used [96],

$$W_{\text{SE1}}(f) = \tan^2(\pi ft/2)\frac{\sin^2(\pi ft)}{(\pi f)^2}. \tag{3.26}$$

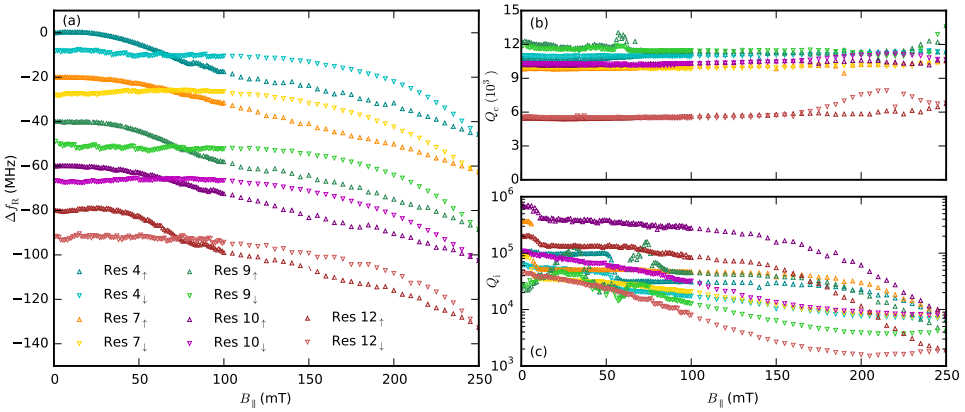

Figure 3.10: Behavior of the resonators when increasing $B_\parallel$ from 0 to 250 mT and back to 0 mT. (a) Deviation from the fundamental frequency at $B_\parallel = 0$ mT. Different resonator traces are offset by 20 MHz each for clarity. (b) Coupling quality factor Q_c versus $B_\parallel$. (c) Internal quality factor Q_i versus $B_\parallel$.

Under the assumption of Gaussian noise, the expected measurement outcome in the computational basis can be expressed as

$$\begin{aligned}\langle\sigma_z(t)\rangle &= \langle\cos(\phi(t))\rangle = 1 - \frac{1}{2}\langle\phi^2(t)\rangle + \frac{3!!}{4!}\langle\phi^2(t)\rangle^2 \pm \dots \\ &= \sum_{n=0}^{\infty} \frac{(-1)^n}{n!}\left(\frac{\langle\phi^2(t)\rangle}{2}\right)^n = \exp\left[-\frac{\langle\phi^2(t)\rangle}{2}\right].\end{aligned} \tag{3.27}$$

Inserting the measured PSD and the appropriate filter function [Eq. (3.26)] into Eq. (3.25) allows us to compute the $1/e$ echo time, using Eq. (3.27). This provides a tool to calculate an upper limit on the dephasing rates due to the setup.

3.6.9. Voltage noise

The procedure described above to calculate the dephasing limit is verified on a gatemon, where additional V_G noise is injected to be the dominating dephasing contribution (Fig. 3.8). Noise is generated by amplifying the 0-output of a Tektronix AWG 5014 with a Mini-Circuits ZFL 500 LN amplifier. Its amplitude is controlled by a Weinschel Aeroflex 8320 variable attenuator (VATT). The noise is injected to the DC biasing circuit using a Mini-Circuits ZFBT-6GW bias tee [inset Fig. 3.8(a)]. The noise PSDs for the VATT at 60 dB attenuation (no added noise) and at 20 dB (added noise dominates) are measured with a SRS SR770 FFT network analyzer in the range $1 - 10^5$ Hz. The range between 10^5 and 10^9 Hz is measured with a Rigol DSA 815 spectrum analyzer [Fig. 3.8(a)]. The PSDs are measured after the bias tee, and

the transfer function correction of the Calmont coaxial line is applied to the measured spectra. Note that the noise level measured for the VATT at 60 dB is not discernible from the instrument background. Hence, this only gives an upper limit to the noise floor. In Fig. 3.8(b), dephasing rates for different noise levels are plotted and compared to the expected rates given the rescaled injected noise using Eq. (3.27). In the cases where the injected noise is dominant the agreement is good. A strong deviation becomes apparent when no noise is injected. This indicates the presence of another noise source. The extracted noise from that source [Eq. (3.24), Figs. 3.8(a) and 3(f)] exceeds the upper limit on the setup noise floor.

3.6.10. Noise in the parallel magnetic field

An accurate estimation of the dephasing time limit imposed by noise in $B_\parallel$ is not possible due to the large inductance of the magnet. Although the current noise of the solenoid biasing circuit was measured, a reliable conversion into an effective noise in $B_\parallel$ is not straightforward. This is because the (frequency-dependent) conversion function of current to field is not known. However, the solenoid acts as a large low-pass filter. Therefore it is unlikely that this source of noise limits the observed dephasing times.

3.6.11. Resonator performance in the parallel magnetic field

The fundamental frequency f_R and the internal quality factor Q_i of the resonators change with applied magnetic field due to the changing kinetic inductance and the induction of vortices in the film. An increase in $B_\parallel$ means a decrease of the Cooper pair density in the superconducting film, leading to a higher kinetic inductance and thus decreasing f_R. This effect can be seen in Fig. 3.9(a), showing the deviation from the zero-field f_R of several resonators against $B_\parallel$. Upon return to zero field, this contribution alone does not lead to a hysteretic effect. Hysteretic effects can arise from a net magnetization of the film producing a change in the current distribution of the resonator mode [111]. Vortices induced in the film will experience a Lorentz force due to the current in the resonator, causing them to dissipatively move around, lowering Q_i. The values of Q_i are extracted using real and imaginary part of the feedline transmission [88]. To speed up measurements, an average intraresonator photon number of ~ 3000 was used. In several of the resonators, a decrease in Q_i between 6 and 10 mT can be observed. This is in qualitative agreement with the observed decrease in $Q_\mathrm{d}(B_\parallel)$ in this field range [Fig. 4(c), inset]. Besides this decrease, the performance of the resonators up to 70 mT allows to perform the experiments presented.

4

Fabrication of airbridges using grayscale lithography

Quantum hardware based on circuit quantum electrodynamics makes extensive use of airbridges to suppress unwanted modes of wave propagation in coplanar-waveguide transmission lines. Airbridges also provide an interconnect enabling transmission lines to cross. Traditional airbridge fabrication produces a curved profile by reflowing resist at elevated temperature prior to metallization. The elevated temperature can affect the coupling energy and even yield of pre-fabricated Josephson elements of superconducting qubits, tuneable couplers and resonators. We employ grayscale lithography in place of reflow to reduce the peak airbridge processing temperature from 200 *to* 150°C*, showing a substantial yield increase of transmon qubits with Josephson elements realized using Al-contacted InAs nanowires.*

This chapter has been published in *Arxiv* (2023) (preprint).[112]

4.1. Introduction

Free-standing metallic strips bridging separate planar conductors, called airbridges (ABs) [113], are widely used in classical [114] and quantum [105, 115–117] microwave-frequency integrated circuits. They are most commonly employed to suppress slotline-mode wave propagation in coplanar-waveguide transmission lines (CPWs) [118, 119] by connecting the ground planes flanking the central conductor, thereby avoiding spurious resonance modes and reducing crosstalk. A second use of ABs is as interconnect allowing transmission lines to cross with low impedance mismatch and crosstalk.

ABs are intensely used in superconducting quantum hardware based on circuit QED [57, 64], where CPWs are commonly used to make resonators for qubit readout and qubit-qubit coupling, as well as qubit control lines. For example, in our planar quantum hardware architecture [120] designed for surface-code error correction, 7- and 17-qubit processors contain ~ 600 and ~ 1200 ABs, respectively, of which 3 and 20 are used for crossovers [121]. In the 49-qubit version, the number of AB crossovers jumps to 130 owing to the routing of qubit control lines from the chip periphery to more qubits at the center. Signal routing at higher qubit counts requires advanced methods based on three-dimensional integration, including through-silicon vias [122–124], bump bonding [125, 126], and the chip packaging itself [127]. In this context, ABs remain essential for slotline-mode suppression and crossovers.

ABs are typically added in the final fabrication step as otherwise resist non-uniformity induced by the few-μm height of ABs can reduce yield and increase variability of post-fabricated circuit elements (for exceptions, see Refs. [1, 128]). The most traditional AB fabrication method uses resist reflow at elevated temperature to produce ABs with smooth, rounded profile. However, many types of Josephson junctions (JJs) are not compatible with this elevated temperature. Examples include the semiconductor-normal-superconductor (SNS) JJs based on InAs [104] and InSb nanowires [129] used in SNS transmons [40, 42] (also called gatemons and nanowire transmons). The temperature excursions can reduce JJ yield at worst and unpredictably affect the JJ coupling energy at best, affecting qubit frequency targeting.

In this Letter, we apply grayscale lithography (GSL), a method most commonly used to fabricate microlenses [130–132], to reduce the peak AB processing temperature from 200°C (required for standard reflow) to 150°C (limited by resist adhesion). We detail our calibration of GSL to accurately produce a curved resist-height profile by spatial control of electron-beam (e-beam) resist dose, with pre-compensation for proximity effect and resist nonlinearity. Our main result is the demonstration that the reduction in peak processing temperature increases the yield of SNS transmons with junctions realized using epitaxially grown, Al-contacted InAs nanowires. Very recent work [117] has demonstrated the use of GSL to fabricate ABs

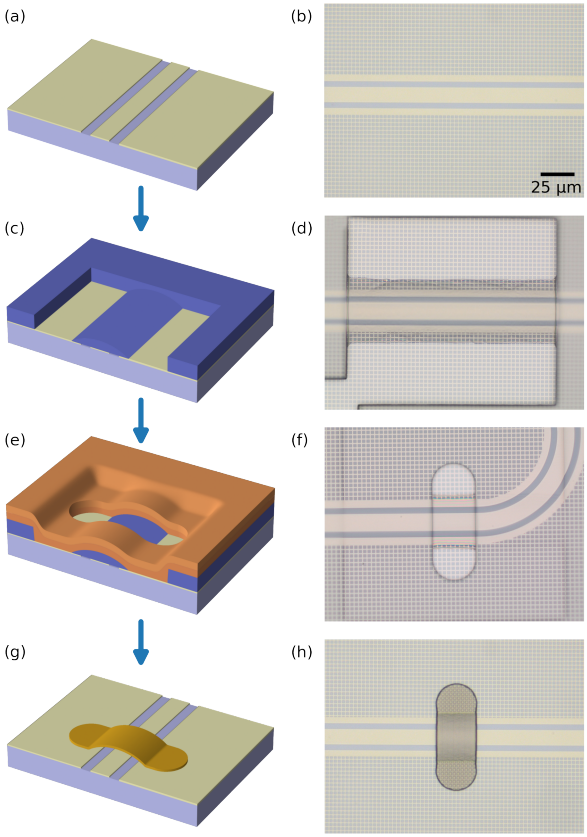

Figure 4.1: Overview of airbridge fabrication by the GSL method, using (left) schematics and (right) optical images. (a,b) Pre-fabrication of the base layer. Our CPW transmission lines have 12 µm center conductor width and 4 µm gaps between the central conductor and the flanking ground planes. (c,d) Patterning of the PMGI (blue) bottom resist layer using GSL. (e,f) Patterning of the PMMA top resist bilayer (orange) defining the lateral dimensions of airbridges. (g, h) Sputtering of NbTiN (gold) and liftoff.

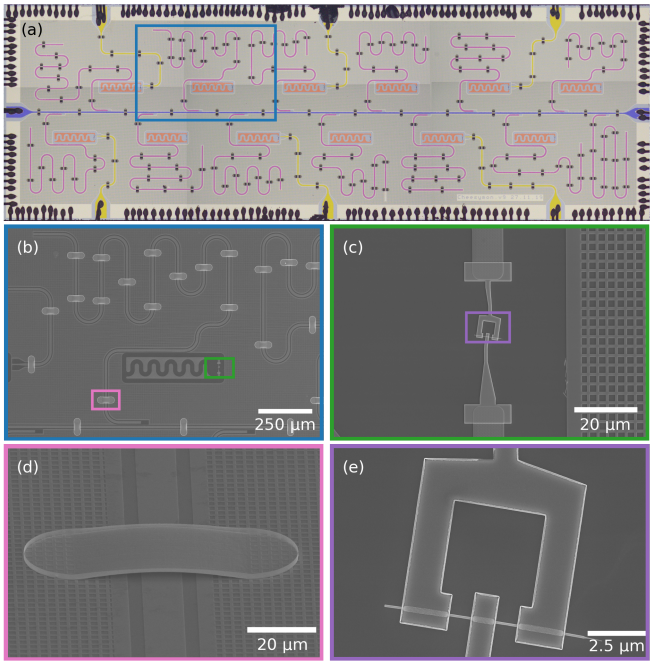

Figure 4.2: Images at various length scales of a circuit QED test device with 100% yield of 185 airbridges fabricated by the GSL method. (a) Optical image of the full device (7 mm × 2.3 mm), with added falsecolor. The device has 12 flux-tuneable SNS transmons (red) with dedicated readout resonators (purple) coupled to a common readout feedline (blue). Six of the SNS transmons have dedicated flux-control lines (yellow). (b,e) Scanning electron micrographs (SEM) showing (b) one SNS transmon and its dedicated readout resonator; (c) the SNS junction pair and its connection to the transmon capacitor pads; (e) zoom-in on the SNS junction pair and SQUID loop; and (d) an example airbridge.

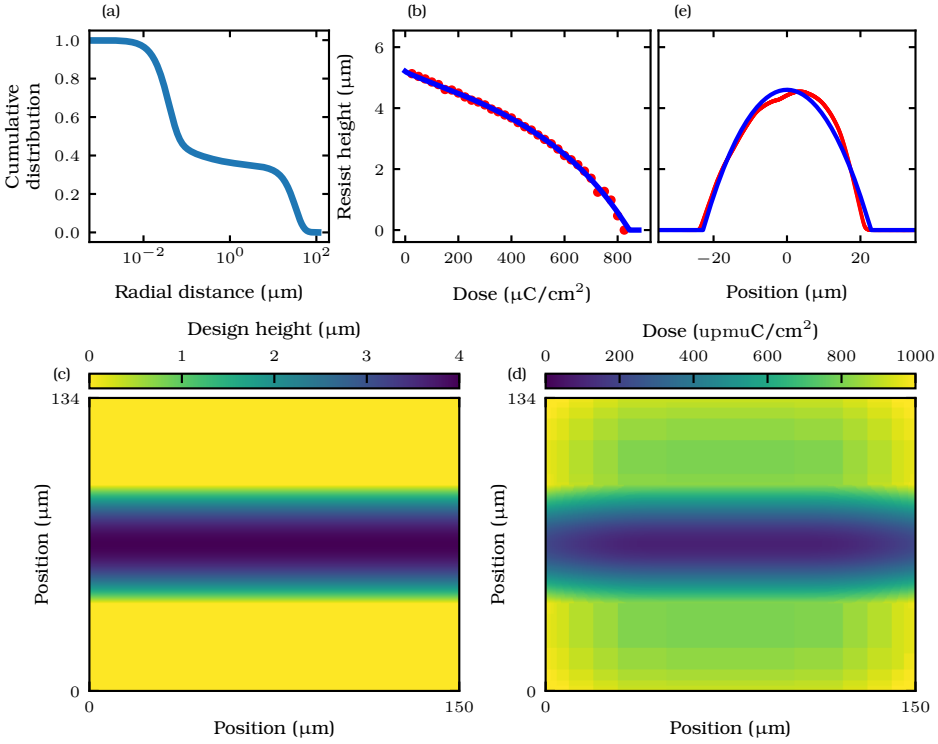

Figure 4.3: Calibration of grayscale e-beam lithography. (a) CDF of the energy of the e-beam in PMGI on top of NbTiN. Note that more than 30% of the energy is deposited beyond a 20 μm radius. (b) Calibration of PMGI height as a function of local e-beam dose (red) and fit (blue) used for interpolation by the software. (c) Two-dimensional image of the targeted resist height for the airbridge. (d) Image of the dose map required to achieve the height map in (d) with precompensation for proximity effect and resist nonlinearity. (e) Vertical line cut (red) of actual PMGI resist height as measured with a profilometer and best fit to a circle function (blue).

with a single e-beam step, showing compatibility with transmons based on standard superconductor-insulator-superconductor (SIS) JJs. Our focus here is on SNS JJ compatibility, with emphasis on the positive impact of AB fabrication at lower peak temperature as enabled by GSL.

4.2. Fabrication

AB fabrication by GSL (Fig. 4.1) starts after defining the chip base layer containing all CPW structures and transmons, including their SNS junctions. A layer of PMGI (blue) SF15 (6.4 or 3 µm thick, see below) is spun and baked for 5 min on a hotplate at 150°C. This is found to be the lowest viable temperature avoiding resist adhesion problems. Using e-beam lithography and GSL, the AB profile and clearances are then written. An AZ400K/water mixture in a 1:4 volume ratio is used for development. The chip is dunked into the developer for 35 s followed by a thorough water rinse for 30 s and blow-drying. At this point, we typically check for correctness by measuring the height profile along the curve of an AB using a profilometer [Fig. 4.3(c)]. Next, a 400 nm thick layer of PMMA 495K (orange) is spun and baked in a vacuum oven at 100°C for 10 min, immediately followed by a 1.5 µm thick layer of PMMA 950k (orange) spun and baked in the same way. E-beam lithography and resist development define the lateral dimensions of the ABs. The top-layer resists must be compatible with the bottom-layer resist. This means that the top layer solvent cannot dissolve the bottom resist after it has been developed and that the developer for the top layer resists cannot develop the bottom layer. A 30 s buffered oxide etch with 1:1 dilution factor is performed prior to metal deposition. We next sputter 200 nm of NbTiN (gold) without any argon milling as the plasma can induce currents in the SNS junctions, causing their failure. A photoresist, 700 nm of S1805 baked at 85°C for 3 min, is used for protection during dicing. After dicing, this resist is lift-off using 88°C N-methyl pyrrolidone (NMP) for 15 min and followed by two rinses in isopropanol (IPA) at 80°C for 10 min. Due to the conformal nature of sputtering, there is a vertical edge of NbTiN left that is approximately the height of the bottom PMMA layer.

Figure 4.2 shows a complete circuit QED test device with 185 ABs fabricated by GSL and with 100% yield. The device consists of 12 flux-tuneable SNS transmons each with a dedicated readout resonator coupling to a common feedline. Six of the transmons have dedicated flux bias lines, but all can be globally tuned using an external coil. The flux-tuneable Josephson element in each transmon consists of two Al/InAs/Al junctions in parallel with loop area ~ 20 μm^2. The two junctions are fabricated from a common hexagonal InAs nanowire with 100 nm diameter and two facets covered with epitaxially grown Al (10 nm thick). Each SNS junction is defined by etching a ~ 200 nm section of Al [Fig. 4.2(e)].

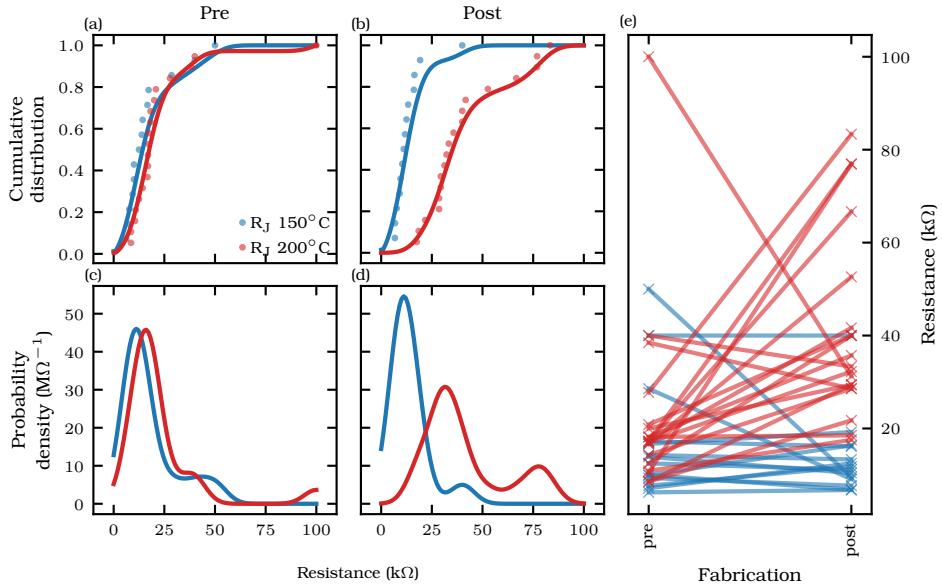

Figure 4.4: Temperature tests of two arrays of single SNS junctions that are exposed to either 150°C (blue) and 200°C (red) for 5 min in PMGI. The tests simulate the temperature excursions of the GSL method and the traditional reflow method, respectively. (a,b) CDFs of junction resistance (a) prior to and (b) following the temperature test. (c,d) PDFs derived from the CDFs (c) prior to and (d) following the temperature test. A clear shift toward higher resistances is observed for the 200°C test. (e) Comparison of each junction resistance before and after the test. Note the relatively similar initial distributions of resistance and the different final distributions.

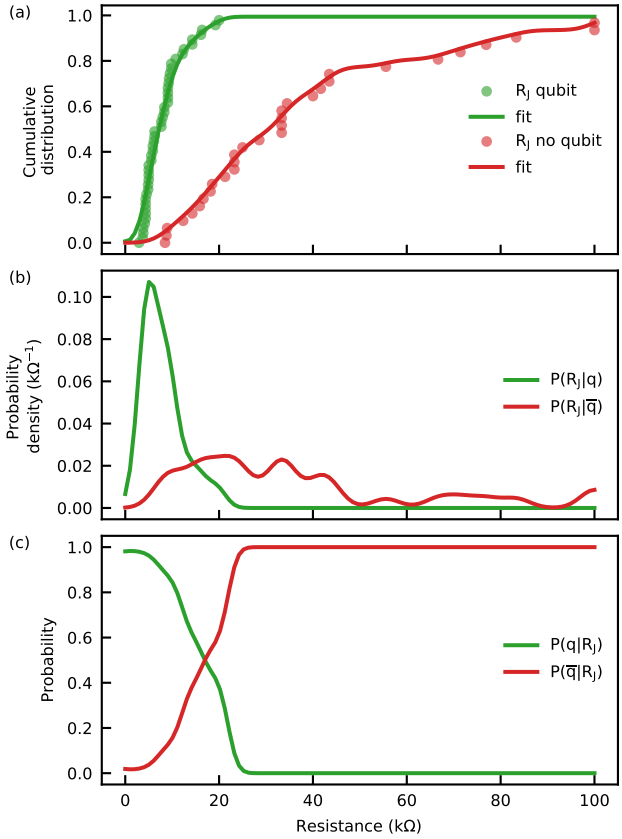

Figure 4.5: Study of the room-temperature resistance of the junction pairs in operable and non-operable SNS transmons. (a) Cumulative distribution function of the resistance for operable (green) and non-operable (red) transmons. Here, operable is conditioned on the observation of a power-dependent frequency shift in the dedicated readout resonator (see Fig. 4.7 for an example). (b) PDF derived from (a). (c) Posterior probability [calculated from (b)] of having an operable transmon as a function of its room-temperature JJ resistance.

4.3. Grayscale lithography

Contrary to the traditional method of producing a curved AB profile by reflowing the PMGI at elevated temperature (200°C), GSL achieves the rounding by spatial control of the e-beam dose. For a positive resist like PMGI, a lower (higher) dose causes slower (faster) removal of the resist, resulting in a higher (lower) remnant resist thickness. Our desired resist-height profile is semi-circular, mimicking the profile achieved in the reflow process by surface tension. To achieve this, it is necessary to correct for proximity error as long-range scattering deposits up to 30% percent of the e-beam energy at a range exceeding 20 µm [Fig. 4.3(a)]. If this effect is not compensated, areas with dense (sparse) features are overexposed (underexposed). It is also important to calibrate the non-linear dose-height correspondence (contrast curve). Non-linearity is desirable in typical microfabrication, as almost all processes require a binary resist profile (so-called perfect contrast) in which the resist is either not exposed or fully exposed. On the other hand, a linear resist is ideal for GSL. The non-linearity of PMGI (6.4 µm thick) is evident in the measured contrast curve shown Fig. 4.3(b). We precompensate proximity and resist nonlinearity using the three-dimensional proximity effect correction (3D-PEC) module in the GenISys BEAMER software [133]. The inputs are the point spread function of the energy deposited by the e-beam lithography machine on the resist stack, the interpolated contrast curve [134] and the desired height map [Fig. 4.3(c)]. The output is a prescribed position-dependent dose. Following these calibrations, we actually reduced the thickness of the PMGI layer to 3 µm in order to reduce stress in the film, which at the original thickness caused cracks in the resist and many nanowires to detach. By reducing the development time from 50 to 30 s, the calibrations were found to remain valid. This GSL process has very high yield and is stable with time. The first and last fabrication runs performed using the process, 16 months apart, yielded very similar airbridges without recipe adjustments.

GSL avoids the PMGI reflow step needed in the traditional method, reducing the peak PMGI temperature from 200°C to 150°C. We devise a simplified test to investigate the effect of PMGI peak temperature on SNS JJ room-temperature resistance. This test entails spinning 3 µm of PMGI on two chips with arrays of single junctions. Next, one chip is heated on a hotplate for 5 min to 150°C while the other is heated to 200°C. The chips are not directly placed on the hotplate; rather, as is standard practice, a Si wafer (6” diameter) is placed in between. Finally, the resist is stripped off using a bath of NMP at 88°C followed by two baths of IPA at 80°C.

4.4. Temperature compatibility of InAs nanowire junctions

For a valid comparison, it is important that initial junction resistances for both chips be similar. Two-point resistance measurements using a manual probe station confirm the overlap of cumulative distribution functions (CDFs) of initial resistance for both chips, as shown in Fig. 4.4(a). We perform a fit using kernel density estimation [135] to each of these CDFs and compute the derivative of the best fits to estimate the probability distribution functions (PDFs) of resistance. The results, shown in Fig. 4.5(c), reveal a pre-test concentration around 20 kΩ for both chips. The different temperature excursions make the resistance distributions become qualitatively different, as shown by the CDFs in Fig. 4.4(b) and the PDFs in Fig. 4.4(d) (similarly obtained). For junctions exposed to 150°C (200°C), the distribution of resistances shifts downward (upward). The trajectory of individual junctions can be followed in Fig. 4.4(e). For 150°C, the majority of resistances stay close to their initial values. For 200°C, however, the majority increase. Some junction resistances do decrease in both cases, particularly ones starting at the high end. While we do not understand the reason for this decrease, we speculate that it may arise from the different cleaning procedures used after the initial JJ contacting (see Supplementary Material) and after the simulated AB step.

4.5. Junction pair resistance and operability

Finally, we connect the of a transmon as a qubit at cryogenic temperature to the room-temperature resistance of its SNS junction pair. We deem a transmon to be operable if we can simply observe of a power-dependent shift of the frequency of its readout resonator (see Fig. 4.7 for an example). In total 78 qubits were measured from 8 different devices. These devices fall into three categories: 3 devices without ABs, in which 18 of 25 transmons were operable; 1 device with ABs fabricated by reflow, in which 1 of 9 transmons were operable; and 4 devices with ABs fabricated by GSL, in which 28 of 44 transmons were operable. Figure 4.5(a) shows numerical CDFs of the junction pair resistance for transmons that exhibit resonator power shifts (green) and for transmons that do not (red). These data clearly show that the resistance corresponding to an operable transmon is generally lower than that of a non-operable one. Fits to these numerical CDFs are done using kernel density estimation [135]. The derivative of each best fit gives a probability density function (PDF) [Fig. 4.5(b)]. Using a Bayesian update, we extract the posterior probability of a transmon being operable given its room-temperature resistance. The probability [Fig. 4.5(c)] starts off close to unity and decreases to 0.5 by ~ 18 kΩ. The probability reduces to near zero by ~ 25 kΩ. We conclude that for a good SNS Josephson junction it is vital that the room-temperature resistance be as low as possible,

cementing the benefits of GSL-based AB fabrication.

In summary, we have employed grayscale lithography to reduce the peak temperature for airbridge processing compared to the traditional reflow method. We have shown that lowering peak processing temperature from 200°C (needed for PMGI reflow) to 150°C (limited by PMGI adhesion) increases the yield of operable SNS transmons based on InAs-nanowire Josephson junctions. We have done this in two steps. First we showed that GSL-based fabrication produces lower room-temperature JJ resistances. Secondly, we showed that lower JJ resistance increases the probability of having an operable SNS transmon at cryogenic temperature. For future work, it remains important to correlate the AB fabrication process with SNS transmon coherence time. It is also worthwhile to explore other e-beam resists that bake at lower temperatures without suffering adhesion problems as well as optical GSL using a direct laser writer, which could possibly lower baking even to room temperature.

4.6. Supplemental material

This supplementary material describes the SNS junction fabrication, compares the processes for airbridge fabrication using the GSL method and the traditional reflow method (Table 4.1 and Fig. 4.7), and shows a typical example of a power-dependent resonator frequency shift (Fig. 4.7).

4.6.1. SNS junction fabrication

The SNS transmon fabrication recipe is adopted from [42]. First, the nanowire is transferred from a growth chip to the device using a nanomanipulator. A 180 nm thick layer of PMMA 950k is applied and baked for 5 min on a hotplate at 150°C. Using e-beam lithography, a 80 nm rectangular window defined at the desired location of junction, where the Al is to be removed. The PMMA is developed using a MIBK/IPA mixture with 1:3 volume ratio for 60 s, followed by a 10 s dunk in an ethanol/IPA mixture with 1:3 volume ratio, and finally a 10 s rinse in IPA. The Al is etched using Transene D at 48.2°C for 12 s, followed immediately by two dunks in water (first 5 s and then 30 s). The junction defining process is finished by removing the PMMA in acetone for 5 min at 55°C and cleaning with IPA for 10 s at 55°C followed by blow-drying.

To contact the nanowire junctions to the transmon capacitor pads, a 280 nm layer of PMMA is spun and baked for 5 min at 150°C. The e-beam writing and development is the same as for the etch windows. After development, the chip is loaded into a sputtering machine, where a 120 nm thick layer of NbTiN is deposited. An in-situ argon mill is first done for 90 s at 50 W and 3 mTorr to improve the contacting to the nanowire. (The duration of this critical process was pre-optimized for the lowest junction resistance.) Immediately afterwards, a thin NbTi sticking layer is deposited followed by the DC-sputtering of NbTiN at 2.5 mTorr and 250 W.

4.6.2. Airbridge fabrication using the reflow method

The fabrication process for the reflow method starts following pre-patterning of the chip base layer. A 6.4 µm thick layer of PMGI SF15 is spun in 2 layer steps. Both layers are baked for 5 min on a hotplate at 180°C. Then, using e-beam lithography, a rectangular profile with clearances is made at the desired position of airbridges. An AZ400k/water mixture in a 1:4 volume ratio is then use to develop the PMGI. The chip is dunked into the developer for 50 s, followed by a thorough water rinse for 30 s, and finished by blow-drying. The chip is then placed on a hotplate at 200°C for 5 min to reflow the resist and thus produce round profile. Due to surface tension, the resulting height of the PMGI at the airbridge location is higher than the original resist height. The resulting layer is shown in Fig. 4.6(f). Next, a 400 nm thick layer of PMMA 495K is spun and baked on a hotplate at 150°C for 5 min, immediately followed by a 1.5 µm thick layer of PMMA 950k spun and baked in the same way. After e-beam lithography and development, the resist looks as in Fig. 4.1(g).

	GSL	Reflow
Resist contrast	low	any
Resist type	positive	positive or negative
Need compatibility with solvent of top top resist stack	yes	yes
Can developer top resist stack develop the bottom resist	no	no

Table 4.1: Comparison of the requirements for the resist used for the GSL method and the traditional reflow method.

4.6.3. Resonator power-induced frequency shift

We judge whether or not a transmon is operable by determining whether its dedicated readout resonator exhibits a frequency shift when measured with increasing incident power. A typical measurement of a readout resonator as a function of incident power on the feedline is shown in Fig. 4.7. In this case, there is a upward 2.2 MHz shift of the resonance frequency with increasing power. A positive (negative) frequency shift indicates that the transmon qubit transition frequency lies above (below) that of the resonator. For SNS transmons based on InAs nanowires, the qubit transition frequency cannot be accurately targeted, and can fall above and below the resonator.

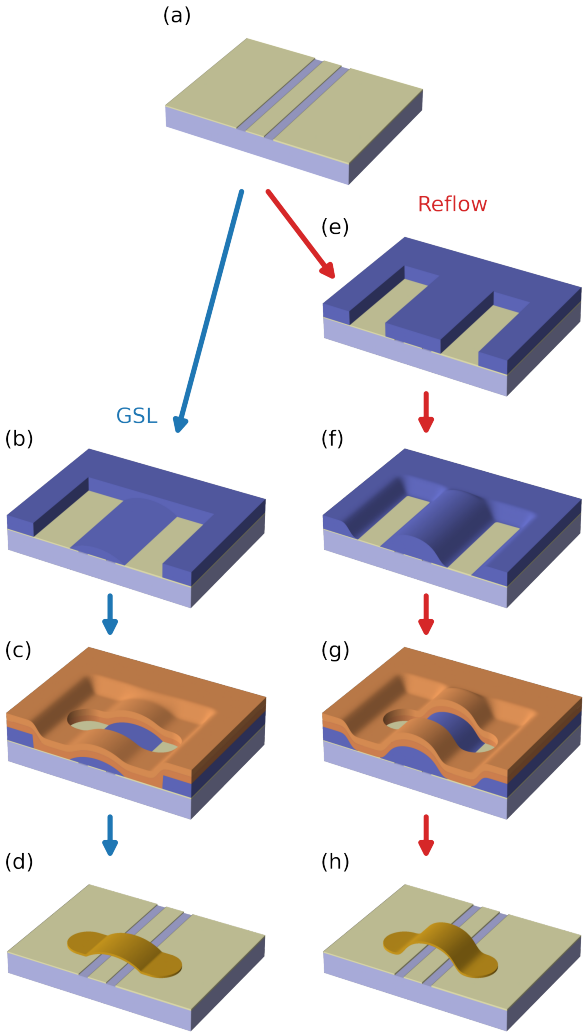

Figure 4.6: Comparison of airbridge fabrication steps using the GSL method (left, blue arrows) and the reflow method (right, red arrows). (a) Both methods start with the pre-fabrication of the base layer. (b,e) A layer of PMGI is spun and developed for both methods. The GSL method directly produces the round profile. (f) The reflow method requires reflow at 200°C to produce the round profile. (c,g) A PMMA bilayer is used to define the lateral airbridge dimensions. (d, h) NbTiN is sputtered and lifted off.

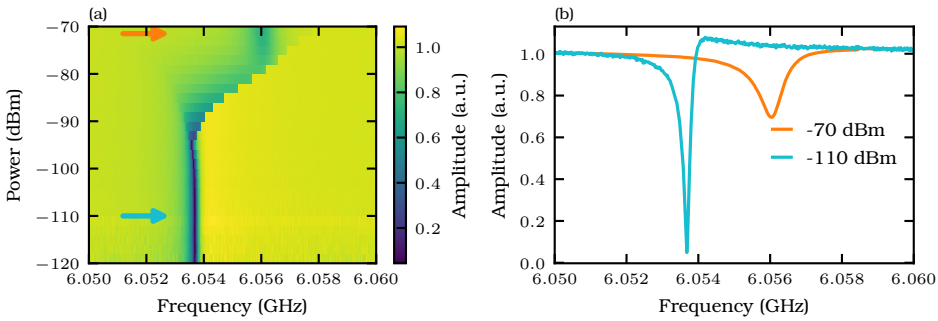

Figure 4.7: Example shift of the resonance frequency of a dedicated readout resonator with increasing incident power on the feedline, indicating that the coupled SNS transmon is operable. (a) Image plot of normalized feedline transmission as a function of probe frequency and incident power. The resonance shifts from 6.0538 GHz at −110 dBm to 6.0560 GHz at −70 dBm. This positive shift indicates that the qubit transition frequency is above the resonator frequency. (b) Linecuts of feedline transmission versus frequency at −110 dBm (cyan) and −70 dBm (orange).

5

Flux noise in an in-plane magnetic field

Flux noise is affecting all superconducting qubits that have a SQUID loop. Despite the importance of flux noise there is not a conclusive model and mitigation strategy. Affecting the flux noise by applying a magnetic field is one way to study the dynamics and get more information on the microscopic origin. Here, we establish a routine to measure the dephasing of the qubit and extract the dephasing rate. We then measure the dephasing rate for a range of different flux values. A fit of the qubit spectrum as a function of flux gives the sensitivity to flux noise at each qubit frequency. From the dephasing rate as a function of sensitivity we extract the $1/f$ flux noise amplitude. Finally the measurement routine is repeated for all magnetic fields up to 140 mT in steps of 10 mT. The key result of this chapter is that the flux noise amplitude increases linearly as a function of magnetic field.

5.1. Introduction

Flux noise is an age old problem plaguing many superconducting technologies that incorporate a squid loop, such as extremely sensitive magnetometer, RF SQUID and superconducting qubits. One such device is the flux tunable transmon qubit. Here, a magnetic flux is able to tune the transition frequency of the qubit. This is useful as a flexibility to target a specific frequency and is also frequently used for the control of 2-qubit gates [4–8]. However this control knob also makes the qubit sensitive to dephasing via flux noise. Magnetic flux noise causes dephasing by randomly changing the qubit frequency and phase. Flux noise has been a practical limitation to the technology since it was first measured in a SQUID [11]. Though progress has been made [13–17] and models have been proposed [18–21], the microscopic origin of flux noise has never been unambiguously confirmed. One way to affect the magnetic flux noise is to apply a large polarising magnetic field to the sample and observe the flux noise spectrum and amplitude. This will affect the noise in a new way and provides a test for the models that was not possible before due to compatibility limitations of the devices. Recent advances have made superconducting cQED compatible with a large in-plane magnetic field [136] while keeping the coherence [36, 42]. In this chapter a way to measure the flux noise amplitude is discussed in section 5.2, then the data analysis and the flux noise amplitude is presented in section 5.3 and finally the magnetic field is turned on and the flux noise amplitude is tracked in section 5.4.

5.2. Calibration and measurement

The flux noise measurement routine at every magnetic field value requires calibration and characterization of the qubit and resonator for every flux bias value. Since the qubit changes in frequency for every flux bias value, and via the dispersive shift the resonator as well, it is necessary to remeasure them. The resonator is measured using an 8 µs square pulse at a variable frequency [Fig. 5.1(a)]. At the resonance frequency of the quarter wave resonator the transmission through the feedline dips and if it is lossless, the dip will go all the way to zero. The square pulse of 8 µs is the longest excitation time possible in the software framework we are currently using. This time sets a minimum resolution possible in the frequency domain of about 20 kHz, which compared to the width of the resonator, of $\Delta f = f_r/Q = 290$ kHz is at the limit of what is possible to measure with such a short excitation pulse without any significant distortion. Here the quality factor of the resonator is $Q = 220000$ and the resonance frequency is $f_r = 6.40053$ GHz. The frequency of minimum transmission is chosen as a bias point for qubit readout, this also corresponds in this case to the resonance frequency. Next the qubit $|0\rangle - |1\rangle$ transition frequency (f_{01}) is determined. While monitoring the resonator bias point a second continuous wave (CW) radio frequency (RF) excitation is introduced and its frequency is swept [Fig. 5.1(b)]. When

this RF tone is resonant with the qubit transition, the transmission through the bias point of the resonator increases due to the dispersive shift of the resonator and a peak in the transmission is observed. This peak is a starting point of the f_{01} calibration, which is not exact due to stark shifts of the readout and excitation tones.

Next the time domain calibration determines the pi pulses and fine tunes the f_{01} transition frequency. First a Rabi measurement is done to calibrate the X_π, Y_π, $X_{\pi/2}$ and $Y_{\pi/2}$ pulses [5.2(a)]. The amplitude for the π-pulses is double that of the π/2-pulses and this is good enough calibration for the measurements that these are used for [5.3]. The X_π and Y_π pulses differ by a 90 degree phase. After the calibration of the pi pulses it is possible to do a fine frequency calibration using a Ramsey measurement. The typical detuning of the pi pulses frequency from the f_{01} transition after qubit spectroscopy for the measurements shown here is about 2-5 MHz. This is a relatively large detuning and is too large to have good quality time domain measurements later. Typically only one of the prerotations is done [42] as it is enough to determine the magnitude and sign of detuning, for example Ramsey x-y in figure [5.2]. However there are several advantages to measuring both $\langle x \rangle$ and $\langle y \rangle$. First of all, it is possible to orthogonalize decay due to decoherence and the effect of detuning. If only one of the quadratures is measured a small detuning can have the same syndrome as decoherence. Another advantage is the direct access to the detuning via the phase of the state, which is the angle of the point $(\langle x \rangle, \langle y \rangle)$ with the x-axis. The derivative of the phase as a function of time directly gives the detuning. The final advantage is for the fitting process. Having two data traces providing independent data for the same model makes the fitting more accurate especially since the detuning and decoherence are orthogonal for this model. The downside is that you need to take two times the amount of data, which takes about double the time. The qubit state evolution for the Ramsey measurement is modelled as a complex exponential with an oscillation, decay and a complex offset,

$$R(\tau) = A \exp\left[2\pi i \left(\Delta f \tau + \phi\right) - \frac{\tau}{T_2^*}\right] + c' + ic''. \tag{5.28}$$

Where A is the amplitude, Δf is the detuning of the drive frequency to f_{01}, ϕ is a phase offset, τ is the Ramsey free evolution time, T_2^* is the Ramsey $1/e$ decay constant and $c = c' + ic''$ is a complex offset. The complex function $R(\tau)$ has $\langle x(\tau) \rangle = \mathrm{Re}\{R(\tau)\}$ as the real part and $\langle y(\tau) \rangle = \mathrm{Im}\{R(\tau)\}$ is the imaginary part. Compared to measuring only one component there is only one extra variable, which is the offset c'', out of 6 total free variables. The data shown in [Fig. 5.2(b)] is simultaneously fit to both quadratures using Eq. (5.28), yielding a detuning of $\Delta f = 2.40$ MHz and a $T_2^* = 211$ ns. The phase as a function of time is plotted in fig. 5.2(d). The phase as a function of time is not a straight line in this case, since the center of the data in the complex plane [fig. 5.2(c)] is not at (0,0). This causes the phase

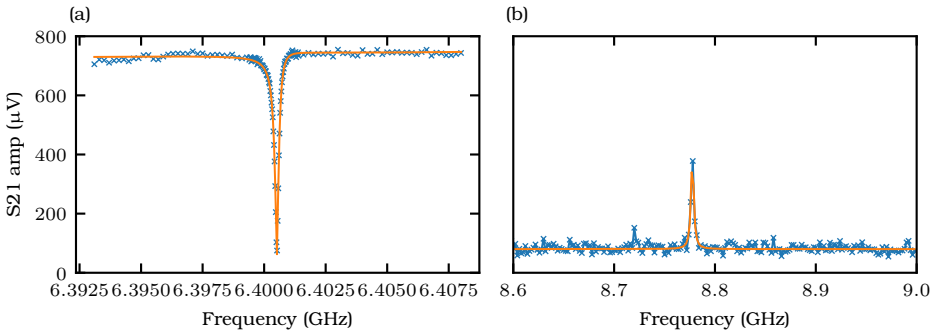

Figure 5.1: Basic characterization of the qubit and the resonator. (a) Resonator spectroscopy to figure the readout conditions necessary for qubit spectroscopy. At the resonance frequency of the quarter wave resonator the transmission through the feedline is minimum. This frequency is chosen for qubit readout. (b) Qubit spectroscopy for the $|0\rangle - |1\rangle$ transition. While reading out the resonator at the minimum transmission point, a second drive is swept in frequency. Once the drive is resonant with the transition, the qubit is partially excited and the resonator frequency shifts. This results in a peak at the qubit $|0\rangle - |1\rangle$ transition frequency.

5

angle which is defined relative to (0,0) to be dependent on what the offset is, after the oscillation has decayed to the point where the origin is not inside the circle anymore, no more phase is acquired and the fit phase does not increase anymore. When the center is corrected to be at the offset point c this artefact is corrected and the phase follows a straight line. However this artefact does not affect the ability to fit the detuning Δf correctly. The Rabi and Ramsey measurement provide a sufficient basis for the measurements performed in this chapter.

Finally the measurements of the decay time (T_1) and the Hahn echo dephasing time T_2^E are taken at a particular flux bias after the calibrations are done. The T_1 measurement determines how long it takes for the qubit to lose its excitation. The echo measurement consists of a $X_{\pi/2}$, a free evolution time $\tau/2$, X_π, a second free evolution time $\tau/2$ and a final pulse $X_{\pm\pi/2}$ which has either a positive or negative rotation. This allows to double the contrast in the measurement and aids in the fitting process. The two curves in Fig. 5.3(b) is fitted with an exponential and Gaussian decay,

$$E(\tau) = \pm A \exp\left[-\left(\frac{\tau}{T_2^{\text{exp}}}\right) - \left(\frac{\tau}{T^g}\right)^2\right] + c. \tag{5.29}$$

Here, the top curve in Fig. 5.3(b) has the positive sign and the bottom curve the negative sign, T_2^{exp} is the exponential decay time, T^g is the Gaussian decay time and c is an offset. The relaxation time measurements and

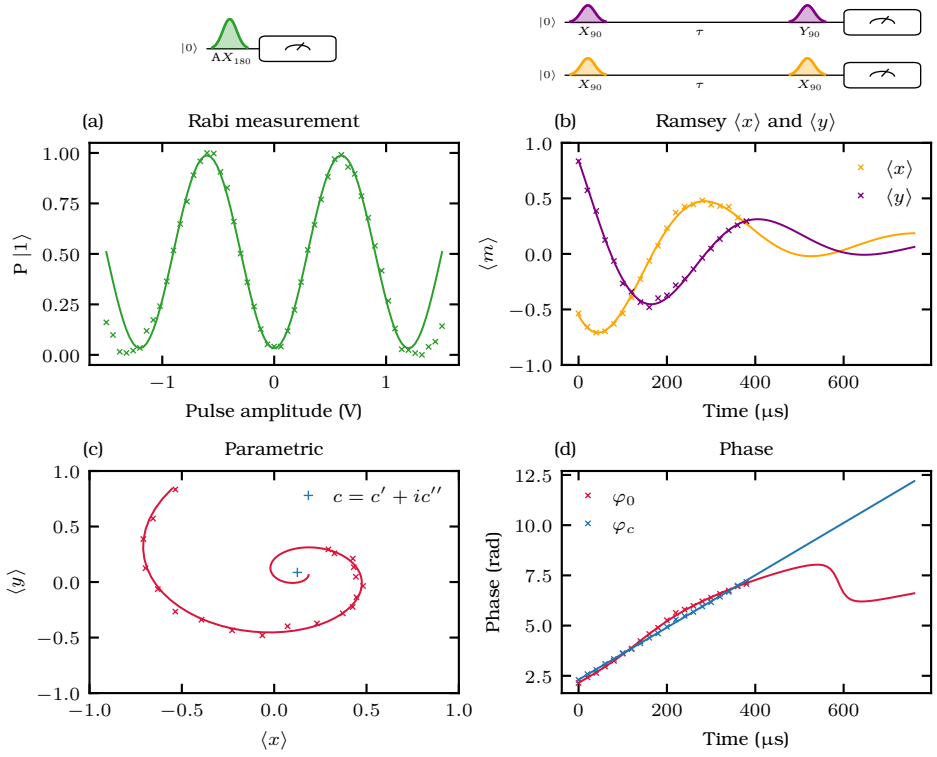

Figure 5.2: Time-domain calibration of the qubit. (a) Rabi measurement of the qubit where the excitation is monitored as a function of a Gaussian pulse centered at the f_{01} frequency. The deviation from the cosine at $\pm$ 1.2 V and higher can be due to mixer saturation or amplifier compression and is nonphysical. (b) Ramsey measurement for fine determination of the f_{01} transition frequency. The Ramsey sequence consists of a $X_{\pi/2}$ followed by a free evolution time τ and finally either another $X_{\pi/2}$ or a $Y_{\pi/2}$. This allows for measuring both the $\langle x \rangle$ and $\langle y \rangle$ expectation values after the free evolution time. This corresponds to the equator on the Bloch sphere. (c) Equatorial plane of the Bloch sphere with the parametric evolution of the qubit state after free evolution. The blue plus describes the center. (d) Phase of the qubit state as a function of time with respect to (0,0)(red) and with respect to (c',c")(blue). The fact that the red curve is not a straight line is due to the fact that the phase is not measured in this case with respect to the center of rotation. For the blue curve this is the case. The phase allows for accurate fitting and extraction of the frequency detuning of the qubit and calibration of f_{01}.

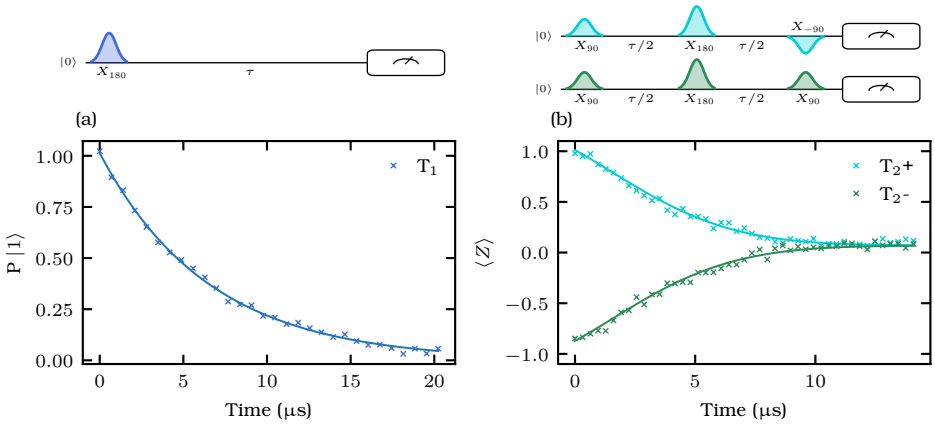

Figure 5.3: The time-domain measurements and their best fits presented in this chapter. (a) Relaxation time measurement with the best fit time of $T_1 = 6.53$ µs. (b) Dephasing time as measured with an echo sequence. The best fit parameters of this measurement are $T_2^{\text{exp}} = 7.27$ µs and $T^g = 6.97$ µs.

the dephasing time measurements form a basis to measure the dephasing rates. These measurements are repeated for multiple flux biases (Sec. 5.3) to determine the flux noise amplitude and this is repeated for magnetic fields up to 140 mT (Sec. 5.4).

5.3. Zero magnetic field flux noise measurement

The flux noise amplitude can be calculated by fitting the pure dephasing rates as measured from the echo sequences as a function of sensitivity to flux noise. Therefore the flux bias is varied and the dephasing rates and corresponding sensitivities are noted. The flux noise amplitude is then fitted with a first order polynomial.

5.3.1. Nanowire transmon frequency spectrum

The sensitivity to flux noise is obtained from the fit of the qubit frequency spectrum as a function of flux bias. The peaks are marked in Fig. 5.4(c) with blue crosses and represent the qubit f_{01} transition. This is then fitted using the short junction model for each of the two junctions,

$$H_J = \Delta \sqrt{1 - \tau \sin^2\left(\frac{\phi}{2}\right)}. \tag{5.30}$$

The resulting parameters extracted from the fit are the superconducting energy gap $\Delta = 76.2$ GHz, the transparency of the first junction $\tau_1 = 0.88$ and the transparency of the other junction $\tau_2 = 0.85$. The other free parameters in the model scale the applied current to the flux bias, in this case $\Phi_0 = 832$ μA and a flux offset from the sweetspot of -6.0 μA. The charging energy of the transmon, $E_c/h = 300$ MHz, is set as a fixed parameter. This model is not very accurate at describing the physics, since in reality the assumptions that go into the model are violated here. First of all, the model assumes a junction of zero length. Though from SEM images of a sister device it is known that the average junction length is about 200 nm. This is not directly measured for this device as the standard practice is to not SEM devices before cooldown. This finite size of the junction is known to have an impact on the transmon spectrum properties. Another questionable assumption is that there is only 1 dominant conduction channel in the junction. This is probably not true either, since the measured qubit frequency is too high to be explained by a single conduction channel in each junction, with the standard value of Δ for aluminum, which is about 45 GHz [39, 42]. The aluminum gap, which we use as a free parameter in the model, scales the Josephson energy linearly and can therefore accommodate the extra E_J needed, which may in fact be due to an unmodeled extra conduction channel. The purpose of this model is thus not to represent physical accuracy, but to have an accurate fit of the qubit frequency as a function of flux, allowing to extract the sensitivity accurately as will be necessary in the next section.

5.3.2. Accompanying time domain measurements

Now that the sensitivity at each flux bias point is known, it is possible to assign a dephasing rate to each measured qubit frequency and sensitivity. The pure dephasing rate depends both on the decoherence rate as measured with the echo measurement [fig. 5.3(b)] and the relaxation time [fig. 5.3(a)],

$$\frac{1}{T_2} = \frac{1}{T_\phi} + \frac{1}{2T_1}. \tag{5.31}$$

To get to the desired pure dephasing time and its inverse the dephasing rate it is necessary to subtract the $2T_1$ contribution. Here, two different ways are explored that get to the desired goal and later the two methods are compared. The first method calculates the time at which the coherence is $1/e$ times the original coherence. The $1/e$ time is calculated from the fit, using Eq. (5.29), when the exponent is equal to -1,

$$\left(\frac{T_2^e}{T_2^{\exp}}\right) + \left(\frac{T_2^e}{T^g}\right)^2 = 1.$$

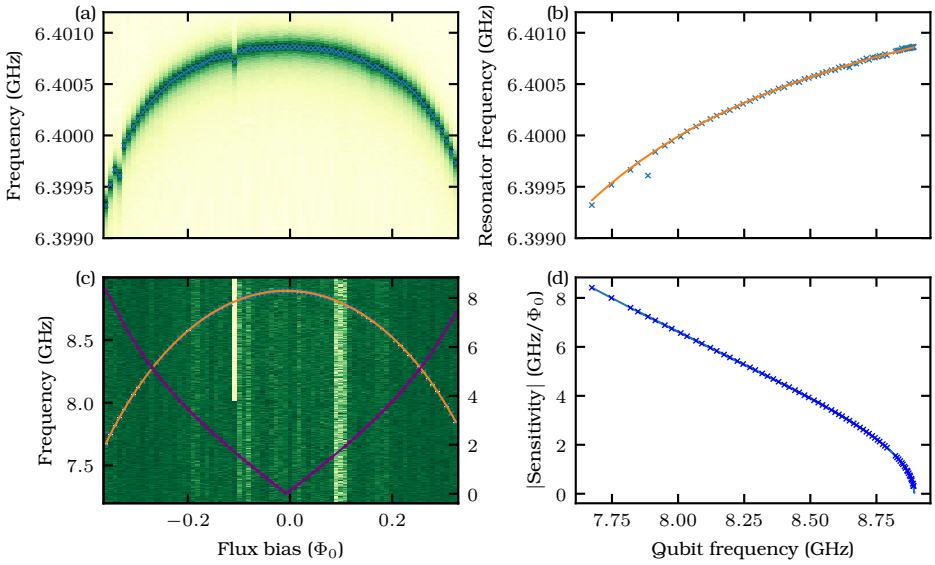

Figure 5.4: Zero field characterization of the flux tunable nanowire transmon. (a) Resonator frequency as a function of flux bias. The resonator is dispersively shifted by the flux tunable qubit. (b) Resonator frequency as a function of qubit frequency. (c) Qubit frequency and sensitivity with applied flux bias. (d) Sensitivity as a function of qubit frequency. This method is used to extract the sensitivity for the decoherence analysis.

This equation can be solved for T_2^e and, after choosing the correct sign for the root, the following relation is obtained

$$T_2^e = \frac{-\frac{1}{T_2^{\text{exp}}} + \sqrt{\left(\frac{1}{T_2^{\text{exp}}}\right)^2 + \left(\frac{2}{T^g}\right)^2}}{2\left(\frac{1}{T^g}\right)^2}. \tag{5.32}$$

Next, the $2T_1$ contribution is subtracted from this time in accordance with Eq (5.31). The resulting times T_2^e and T_ϕ^e are shown in Figs. 5.5(a) and 5.5(b) as a function of flux and frequency. The T_1 time is consistently around 6 µs and increases slightly towards lower frequencies. The T_2^e and T_ϕ^e are maximum at the sweetspot and increase towards lower frequencies, with the T_2^e peaking at around 6 µs an the T_ϕ^e around 12 µs. This is expected since the qubit is first-order insensitive to flux noise at the sweetspot. The second method calculates the dephasing rate based on the shape of the coherence decay of the echo measurement. A white noise spectrum causes exponential decay and a $1/f$ noise spectral density causes Gaussian decay.

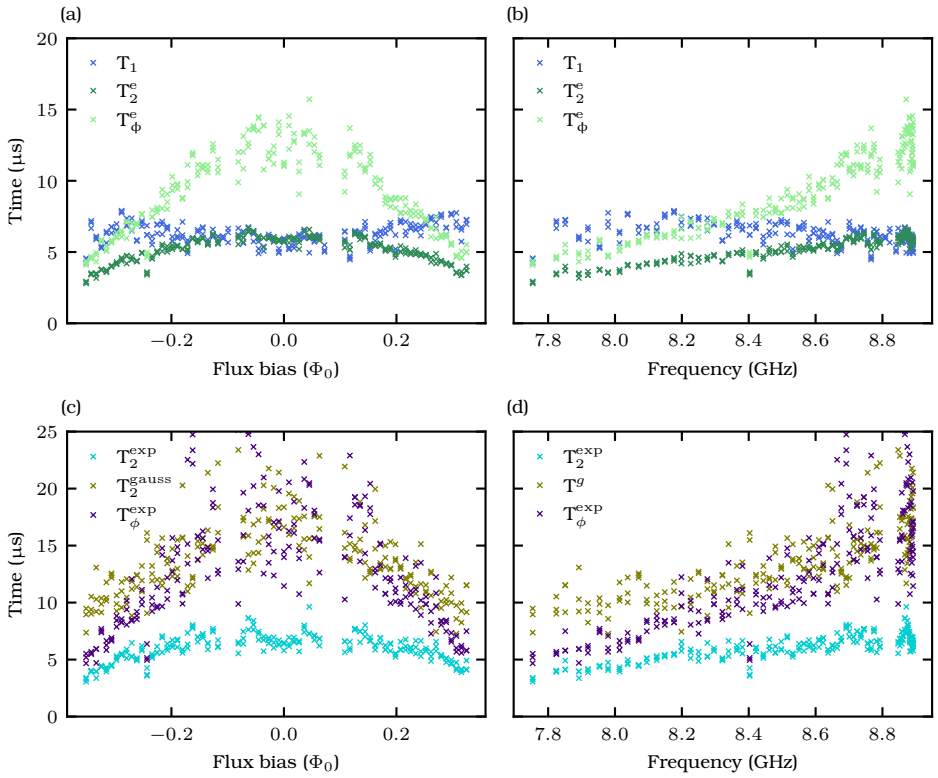

Figure 5.5: Dephasing rates as a function of flux bias and qubit frequency. (a) Dephasing times T_2^e, T_1 and T_ϕ^e times as a plotted against flux bias and frequency (b) using the $1/e$ intercept. (c) Dephasing times T^g and T_2^{exp} as a function of flux bias and qubit frequency (d).

For this reason, the echo decay is fitted with both an exponential and a Gaussian as exemplified in Fig. 5.3 using Eq.(5.29). The T^g extracted from the fit corresponds directly to the $1/f$ flux noise contribution, while the T_2^{exp} also contains the $2T_1$ contribution. The resulting coherence times are shown in Fig. 5.5(c) as a function of flux bias, while the coherence times as a function of qubit frequency are shown in Fig. 5.5. It is clear from this figure that the qubit coherence is mainly limited by exponential decay, since the T_2^{exp} time is more than a factor of 2 shorter than the T^g time. This short T_2^e time is caused by a combination of T_1 and white flux noise. One potential issue with the fitting of the decay using a Gaussian and an exponential is that the two functions are very similar and have high correlation. Therefore it can be possible that the decay constants are not very accurate and a small increase in for example T_2^{exp} can be traded for a small decrease in T^g.

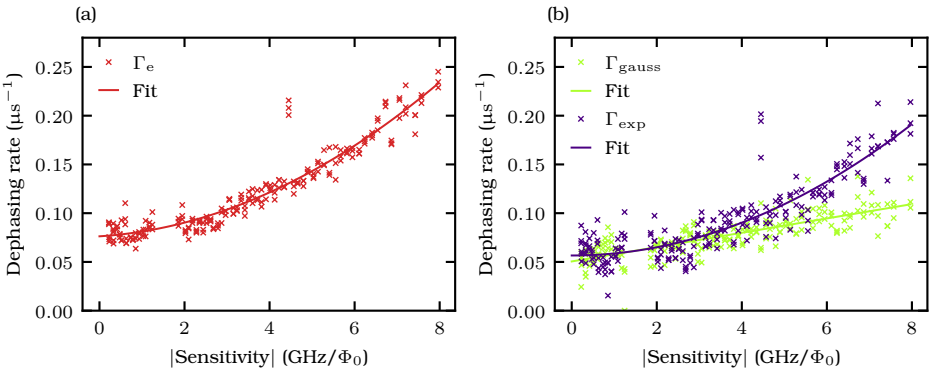

Figure 5.6: Dephasing rate, Γ_ϕ^e as a function of sensitivity to flux. (a) The dephasing rate using the $1/e$ intercept method and the quadratic fit. (b) Dephasing rates $\Gamma_\phi^{\text{gauss}}$ and Γ_ϕ^{exp} extracted from the fit directly. The fit for $\Gamma_\phi^{\text{gauss}}$ is a linear function and Γ_ϕ^{exp} is fit with a quadratic without linear term.

5

This correlation can be seen in Fig. 5.6(b) at sensitivities between 0 and 1 GHz/Φ_0.

There is significant residual dephasing at the sweetspot caused by something other than flux noise. This is indicated by the fact that at the sweetspot the T_2^e time is not equal or close to $2T_1$. Candidates for the dephasing for this particular qubit are charge dispersion, charge noise coupling to the junction and photon shot noise.

Next the dephasing rate is calculated from the dephasing times and plotted as a function of the sensitivity to flux. The relevant dephasing times are T^g, T_2^e and T_2^{exp}, out of which the pure dephasing times T^g, T_ϕ^e and T_ϕ^{exp} are obtained by subtracting the T_1 contribution. The reciprocal of this time is the dephasing rate, $\Gamma_\phi = 1/T_\phi$, and can be related to the flux noise amplitude via the sensitivity to flux. The dephasing rate derived from the $1/e$ time is related to the sensitivity to flux, $\partial f/\partial\Phi$, with a white noise and a $1/f$ noise contribution,

$$\Gamma_\phi^e = \pi^2 a \left(\frac{\partial f}{\partial \Phi}\right)^2 + 2\pi\sqrt{\ln(2)} b \left(\frac{\partial f}{\partial \Phi}\right) + c, \tag{5.33}$$

where a is the white flux noise amplitude and $b = \sqrt{A_\phi}$, A_ϕ is the $1/f$ flux noise amplitude, c captures the dephasing rates not related to flux noise. The measured Γ_ϕ^e and the fit to Eq.(5.33) are shown in Fig. 5.6(a). The data clearly do not follow a straight line, indicating that there is a white flux noise contribution. The best fit parameters to the data are $a = (14.7 \pm 0.7\, n\Phi_0/\sqrt{\text{Hz}})^2$, $b = \sqrt{A_\Phi} = 0.53 \pm 0.30\,\mu\Phi_0$ and $c = 0.076 \pm 0.003\mu\text{s}^{-1}$. These values are lower than what has previously measured [42] with the same

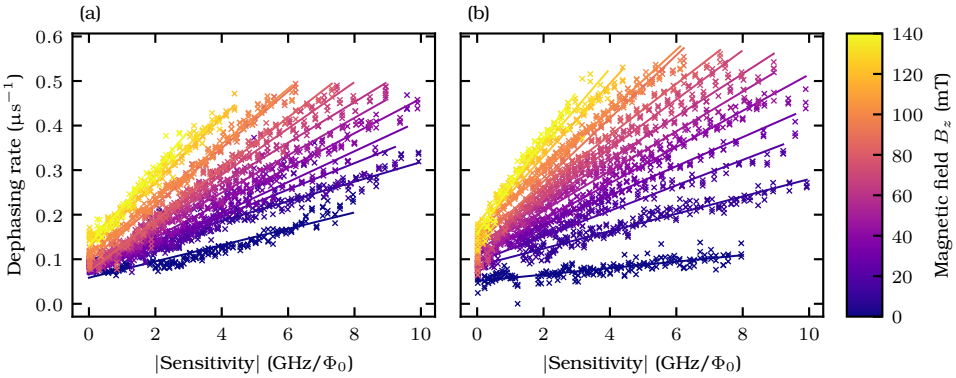

Figure 5.7: The dephasing rates as a function of sensitivity for all magnetic fields. (a) The dephasing rates as measured with the $1/e$ method and the fits in a solid line to Eq.5.35. (b) The dephasing rates from the Gaussian decay and the fit in the solid line using Eq.5.35

materials, a similar setup and the same method, however in line with the flux noise amplitudes measured in other studies [11, 12, 17]

The other method has two dephasing rates, $\Gamma_\phi^{\text{gauss}}$ and Γ_ϕ^{exp}, where the exponential dephasing rate will be fit with a quadratic function and the Gaussian dephasing rate with a line,

$$\Gamma_\phi^{\text{exp}} = \pi^2 a_{\text{exp}} \left(\frac{\partial f}{\partial \Phi} \right)^2 + c_{\text{exp}}, \tag{5.34}$$

$$\Gamma_\phi^{\text{gauss}} = 2\pi\sqrt{\ln(2)} b_{\text{gauss}} \left(\frac{\partial f}{\partial \Phi} \right) + c_{\text{gauss}}. \tag{5.35}$$

The equations are now split, since the $1/f$ noise only causes Gaussian dephasing and white noise only exponential dephasing. The fit and data are shown in Fig. 5.6(b). The best-fit parameters for the exponential part and Eq.(5.34) are $a_{\text{exp}} = (14.6 \pm 0.26\,\text{n}\Phi_0/\sqrt{\text{Hz}})^2$ and $c_{\text{exp}} = 0.057\,\mu\text{s}^{-1}$ and for the Gaussian part, Eq.(5.35), $b_{\text{gauss}} = 1.41 \pm 0.07\,\mu\Phi_0$ and $c_{\text{gauss}} = 0.051 \pm 0.002\mu\text{s}^{-1}$. The fact that $c_{\text{exp}} + c_{\text{gauss}} \neq c$, is due to high correlation between the Gaussian and the exponential part. At small sensitivities initially the exponential part is higher than the Gaussian part and around 1 GHz/Φ_0 the exponential part takes over again. The sum of the rates as indicated by the fit thus seems higher than it is in reality and this is a weakness in the method that cannot easily be overcome. The two methods agree on the amount of white flux noise but disagree on the $1/f$ flux noise. This is likely due to the fact that in this particular case the white noise component is dominant as indicated by the shorter T_ϕ^{exp} time. As the Gaussian component dominates it is expected that the two methods will agree more on this number as well.

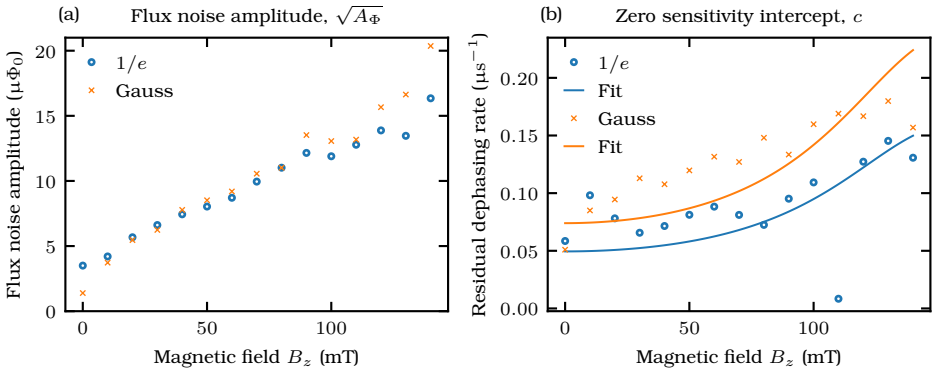

Figure 5.8: Data obtained from the fits to the data of Figs. 5.12(a) and 5.12(b) using Eq. 5.35. (a) Flux noise amplitude obtained from the fit. The cross is the Gaussian dephasing and the circle is obtained from the $1/e$ method. (b) The residual dephasing at zero sensitivity with a fit to the data using the photon shot noise model. The best fit parameters are for the Gauss dephasing $\bar{n} = 0.83$ and for the $1/e$ method of $\bar{n} = 0.55$.

5

5.4. Applying a magnetic field

The magnetic field is finally applied and all the measurements as a function of flux noise are repeated and the dephasing rates as a function of sensitivity to flux are extracted. The main experiment of the thesis is to monitor the flux noise amplitudes as the magnetic field is increased. The measurement routine is the same as discussed in earlier parts of this chapter. First the parallel magnetic field, B_z, is increased in a step of 10 mT. Then the flux bias is swept and for each value the qubit is measured together with the time-domain measurements. The maximum value of the magnetic field where it was possible to have good-quality time-domain measurements covering a large sensitivity range was $B_z = 140$ mT. This yields a total of 15 magnetic fields where the flux noise amplitude is measured. At some of the magnetic field values the qubit frequency is not continuous when the flux bias is swept, these so called flux jumps can be seen in both resonator spectroscopy [Fig. 5.10] and qubit spectroscopy [Fig. 5.11] at $B_z = 20$ mT and $\Phi = 0.6\ \Phi_0$. These flux jumps are the reason that the sensitivity is extracted from the qubit frequency. For each magnetic field, a frequency to sensitivity map is made from a portion of the qubit flux spectrum that does not show any flux jumps. This is the reason that for the majority of the magnetic fields the fit does not correspond entirely to the qubit frequencies. However this is not a problem and for all fields it is possible to have a good fit to at least a portion of the spectrum. Furthermore, for the portions of the spectrum excluded from fit due to a flux jump it is still possible to get the sensitivity. This is done via the qubit frequency to sensitivity map,

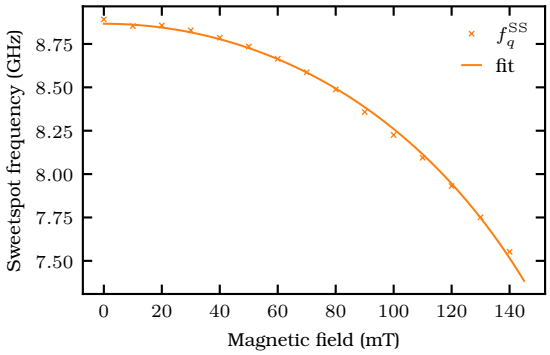

Figure 5.9: Qubit sweetspot frequency extracted from the Hamiltonian fit as a function of magnetic field. The critical field from the fit in the figure is 200 mT.

the data is then included in the time-domain data. Thus even though not everything is included into the fit, all data where it was possible to find the qubit and have good time domain measurements are included in Fig. 5.12.

The dephasing rate as a function of the sensitivity for each magnetic field is plotted for the method using the $1/e$ intercept [Fig. 5.12] and the Gaussian part of the dephasing rate [Fig. 5.13]. Although it is hard to track the dephasing rates for each field, it is clear that for both methods of analysing the dephasing rates increase faster as a function of sensitivity for each field. Except for the zero-field dephasing rates using the $1/e$ intercept method, all the curves are basically a straight line indicating that the $1/f$ flux noise is dominant at all fields except zero. This suspicion is further supported by the fact that the Gaussian dephasing rate is increased significantly in a magnetic field, while the exponential contribution is negligible. The fit using Eq.5.33 to the data of Fig. 5.12 is shown as solid lines. Here the quadratic term is set to zero, since the linear term is dominant and there is no clear quadratic term in the data for fields above zero. The $1/f$ flux noise amplitudes for each field of the $1/e$ method are shown in Fig. 5.8(a). The flux noise amplitude monotonically increases in a magnetic field, which is consistent with another similar measurement [36]. The Gaussian dephasing rates in Fig. 5.12 are fitted using Eq.5.35 and the best fit flux noise amplitudes are plotted in Fig. 5.8.

In a magnetic field, the qubit decreases in sweetspot frequency. The magnetic field reduces the superconducting gap of aluminum in the nanowire junction. There are two reasons for this. First, the alignment along the axis of the nanowire is roughly with the magnetic field, but it is not perfect. This is not adjusted for in the measurement for experimental simplicity. In subsequent cooldowns this has been done, but the qubit performance was not high enough to reproduce the measurements in this chapter. Second,

the aluminum has a critical field that depends on the thickness. So by having a misaligned field, the effective thickess is larger. For bulk aluminum the critical field is around 40 mT. Besides the critical field of the superconductor, there are more reasons that the qubit sweetspot frequency decreases in a magnetic field. There is for example the Fraunhofer effect, due to the finite extent of the junction. However, since we are looking at magnetic fields below any critical field, only a decrease in the superconducting gap is considered. Using the fact that the qubit frequency is proportional to the root of the Josephson energy, the qubit sweetspot frequency is fit with the relation

$$f_{01}(B) = f_{01}(0)\sqrt{1-\left(\frac{B}{B_c}\right)^2}. \tag{5.36}$$

Here, $f_{01}(0)$ is the sweetspot frequency at 0 mT and B_c is the critical magnetic field. The fit to this equation and the sweetspot frequencies at each field are shown in Fig. 5.9. The best fit critical field is $B_c = 200$ mT. This is much lower than reported figures for similar nanowire junctions. This is because of the misalignment of the field with the nanowire axis and because of the fact that no bottom gate is used.

The zero flux sensitivity dephasing rates, the intercepts of the fits of both methods at zero, are plotted in Fig. 5.8(b). These indicate the residual dephasing due to other noise types. One hypothesis is that the residual dephasing is due to photon shot noise. The dephasing rate should than be a function of the detuning with the resonator. Since the resonator frequency is basically constant, the detuning is dominated by the reduction in the sweetspot frequency of the qubit. The other parameter in the dephasing model of Eq. 2.17 is the coupling between the resonator and the qubit. This has been extracted at zero field with the data of Fig. 5.4 and the best fit coupling is $g = 64.7$ MHz. All the ingredients are present to fit the dephasing rate as a function of magnetic field using the field to sweetspot frequency map of Eq. 5.36. The result is shown in Fig. 5.8(b), with the best fit values for the Gauss method of $\bar{n} = 0.83$ and for the $1/e$ method of $\bar{n} = 0.56$. The fit roughly follows the data for the Gauss method and more closely for the $1/e$ method. The fit follows the data relatively well despite the large number of parameters in the model. This means that photon shot noise is a likely candidate for the residual dephasing rate.

5.5. Conclusion and discussion

In this chapter a robust method for measuring the flux noise amplitude was discussed. The Echo dephasing time and the T_1 time were measured as a function of flux bias allowing for the extraction of the dephasing rate. In parallel the qubit spectrum was measured and this provided the sensitivity to flux noise via the calibrated qubit frequency to sensitivity map. This map was obtained from a fit to the spectrum that was redone for every

magnetic field. The decay of the echo measurement was analyzed in two different ways. One method took the $1/e$ time, subtracted the T_1 contribution and then plotted the resulting time as a function of sensitivity. The resulting data were fit with a quadratic yielding the $1/f$ flux noise amplitude the white noise amplitude and an offset. The other method fitted the data using both an exponential and a Gaussian. The Gaussian corresponds to $1/f$ flux noise, while the exponential contains both white noise and the T_1 contribution. After subtracting the T_1 contribution of the exponential part both were plotted against sensitivity. The Gaussian part was fitted with a line and the exponential part with a quadratic. This procedure was then done for all magnetic fields and the data collected. It turned out that the $1/f$ flux noise amplitude increased linearly with magnetic field. This means a quadratic increase in the noise power, which is significant and unexpected. A perhaps naive model would expect the fluctuating spins to be polarized and the energy difference in a magnetic field to be prohibitively large to fluctuate to a higher energy state based on the available thermal energy. This measurement is one of the first to measure the flux noise amplitude in a magnetic field, with the data from [36] being the other one. In their work the flux noise amplitude also increased linearly. Currently we do not understand why the flux noise increases as a function of magnetic field. Perhaps the quantization axis due to the magnetic field is in a different direction than the coupling to the SQUID loop. Or maybe the magnetic field allows for nuclear spins to participate in the flux noise. This however is just speculation.

The maximum field that the qubit spectrum could be measured with high quality at was 140 mT. This was due to a combination of the qubit lowering in frequency and flux jumps in both the resonator and the qubit. The lower frequency of the qubit was due to a misalignment of the nanowire axis with the magnetic field axis. During a later cooldown we did align the magnetic field with the nanowire axis. However due to problems with both the qubit and the cryostat, the data taken during that cooldown was of substantially lower quality.

5.6. Appendix

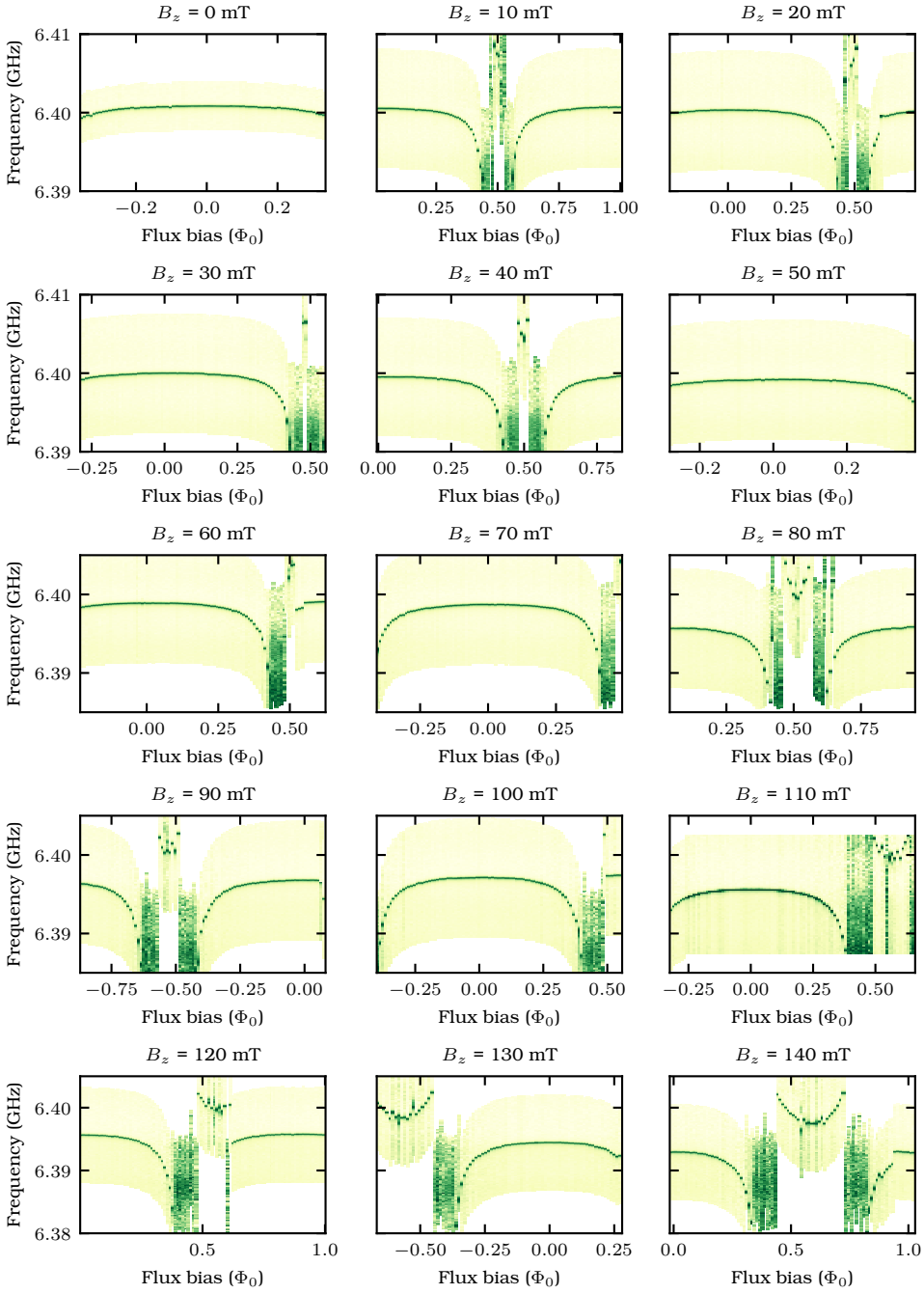

Figure 5.10: Resonator spectroscopy for all magnetic fields. This figure exemplifies the flux jumps of the qubit for example at 20 mT.

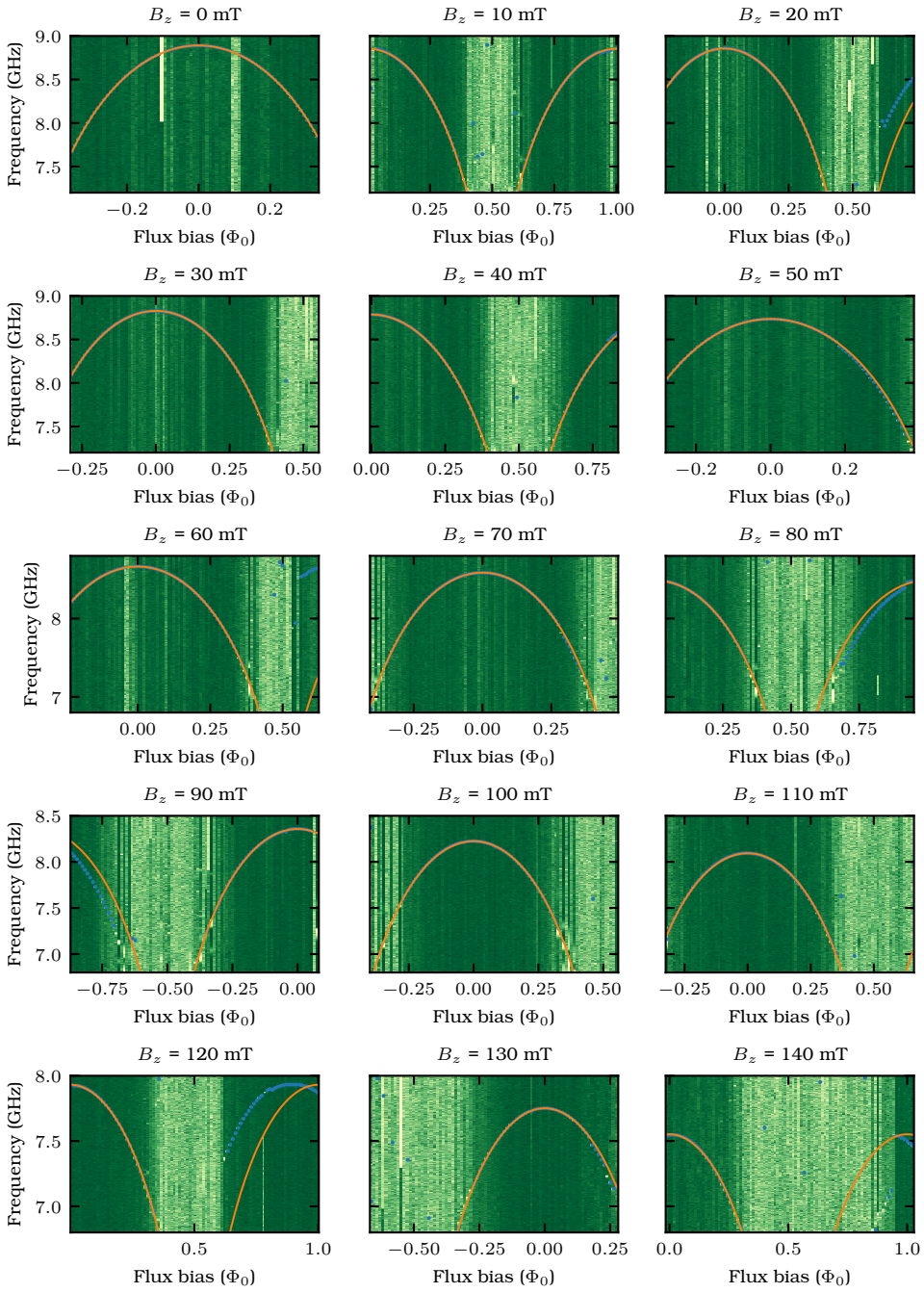

Figure 5.11: Qubit spectroscopy for all fields. The qubit frequencies are plotted in orange and the fit through these points is in orange.

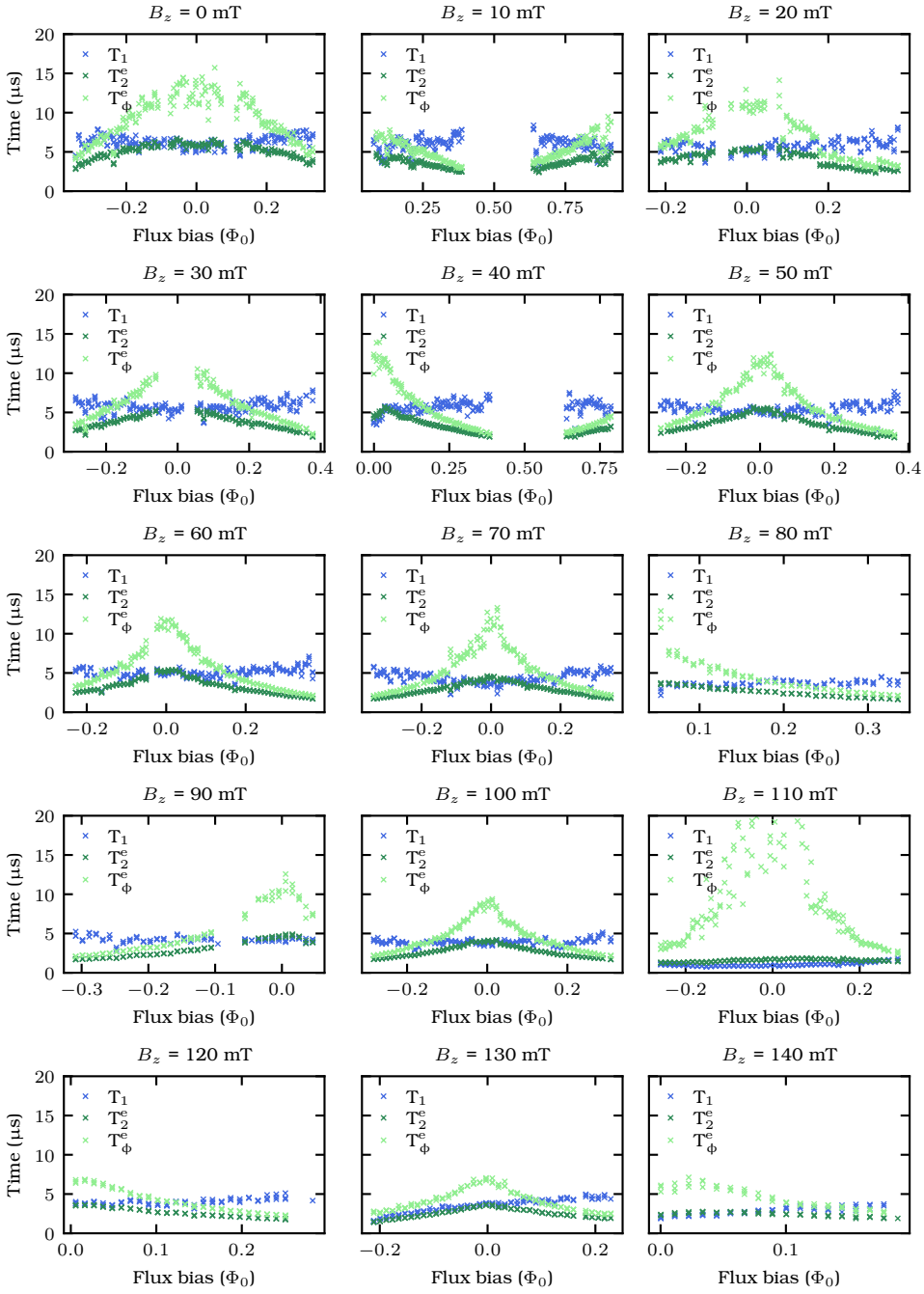

Figure 5.12: Dephasing rates using the $1/e$ method. The data of 110 mT is not taken into account in the main text due to the low T_1.

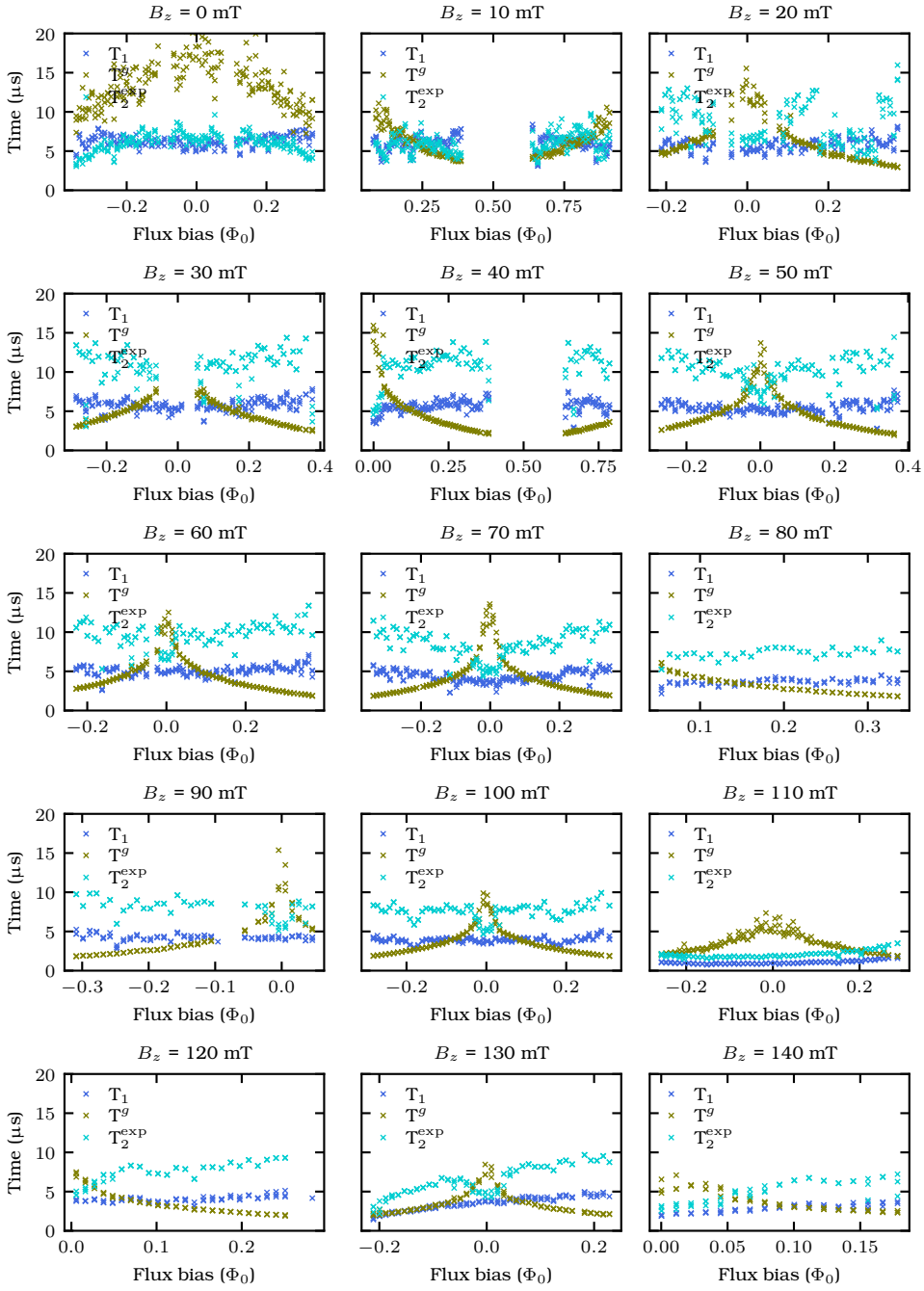

Figure 5.13: Dephasing rates with T^g and T_2^{exp} obtained using the fit to the echo decay.

6

Noise spectroscopy in an in-plane magnetic field

The linear increase in the $1/f$ *flux noise amplitude incites to investigate further. Here we first perform noise spectroscopy using the spin-locking method to obtain the noise power spectral density (PSD) in the MHz regime. Next, we apply a magnetic field and compare the noise PSD with applied magnetic field to the zero-field value. We both change the magnetic field as well as the sensitivity to flux noise. In both cases we do not observe a significant change of the noise in this frequency range. We then measure the noise PSD in the frequency range of* 10^{-2} *to* 10^{2} *Hz using a repeated Ramsey measurement again for both different magnetic fields and sensitivities. Again in this frequency range there is no significant increase in the noise PSD detectable. Finally we derive the noise floor in case of a non-perfect readout fidelity.*

6.1. Introduction

In Chapter 5, a striking increase in the flux noise amplitude was measured that linearly depended on the in-plane magnetic field. Now we want to know in what range in the frequency spectrum the noise is situated that can explain the more than hundred fold increase in the noise power. To this end we do noise PSD measurements for varying magnetic fields and qubit sensitivities to flux noise. There are several methods for measuring the noise PSD of a qubit, these methods are also referred to as quantum noise spectroscopy (QNS). Generally there are two types of QNS, one using engineered pulses combined with free-evolution that allow for the extraction of the noise spectrum [16, 55, 137–140], and the other one under driven evolution [58, 141–143]. For the free-evolution QNS, the standard method is to use a dynamical decoupling sequence, for example CPMG [55, 137–139] or UDD [144], to measure the coherence decay during the free-evolution for the noise power and reconstruct the frequency spectrum at which this noise was present. On the other hand driven evolution methods continuously drive the qubit and monitor the relaxation. One such method is the spin locking method [58, 141, 143]. Here we use spin locking QNS to measure the noise PSD in the 0.2-20 MHz frequency range, because of the ease of extracting the noise power and frequency portion at which the noise is present. Additionally we use a repeated Ramsey measurement [140] for the lower frequency range, 10^{-2} to 10^{4} Hz. The first part of this chapter discusses the spin locking measurements in zero magnetic field and fields up to 80 mT. Next the field is ramped up 100 mT and the sensitivity is increased from 0 to 2 GHz/Φ_0 while the noise PSD is measured. Finally, for the same magnetic fields and sensitivities, a repeated Ramsey measurement measures the noise PSD in the lower frequency range.

6.2. Noise spectroscopy using spin locking

Noise spectroscopy using spin locking has several advantages over other ways of measuring the noise PSD, such as CPMG or Rabi decay [55]. QNS using Rabi decay produces an oscillating function with a decaying envelope. The relatively complicated envelope combined with the oscillating modulation makes it relatively difficult to analyze and determine the noise power. On the other hand, it is relatively easy to determine the frequency at which the noise power is situated, the Rabi frequency. Contrasting to the CPMG or UDD method, here the pulsing sequence makes the coherence decay sensitive to a range of frequencies, making it difficult to extract the noise PSD. However, the decay envelope is usually exponential or Gaussian without oscillations making it relatively easy to analyze. Therefore it is desirable to have a method that combines these two advantages, which is the reason spin locking is chosen.

The spin-locking sequence, also called a $T_{1\rho}$ experiment [141], drives the qubit along the same axis as the qubit state vector on the Bloch sphere.

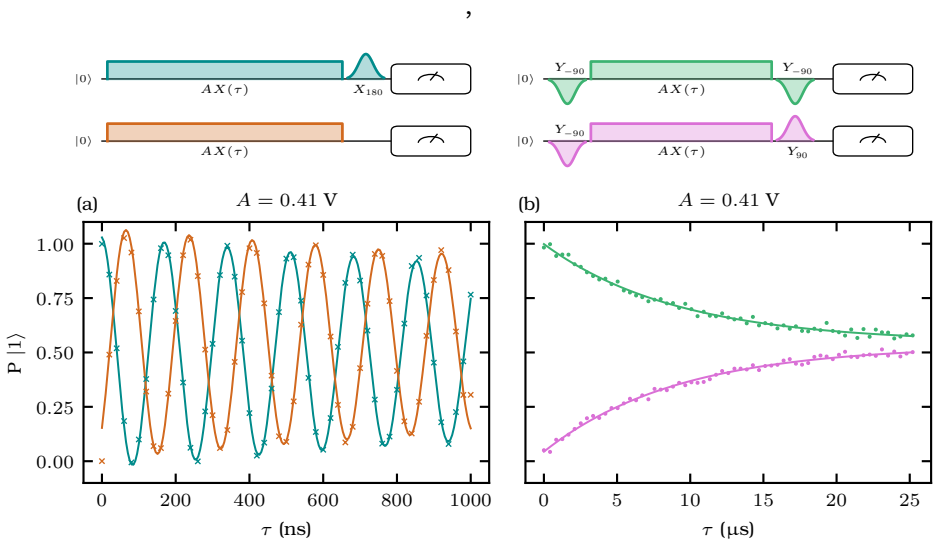

Figure 6.1: Noise spectroscopy using spin locking. (a) Rabi frequency measurement for x-axis calibration of the power spectral density plot. The pulsing circuit for the Rabi frequency measurement is shown above the figure. The circuit indicated with the blue (red) color corresponds to the measurement with the same color in the subfigure below. (b) Spin locking measurement with the circuit indicated above. The decay constant is proportional to the noise power at the Rabi frequency.

This locks the state along the drive, giving the method its name. The sequence starts with the qubit initialized in the $|0\rangle$ state, a Y_{-90} pulse is applied ending the qubit into the $|-\rangle$ state. Then a square pulse is applied along the x-axis on the Bloch sphere with a variable duration, τ, and variable amplitude, A. Because the drive is applied along the same axis as the state vector, the qubit state does not evolve coherently. Finally a tomographic prerotation is applied to readout the qubit state, which ends up in the $|1\rangle$ state or the $|0\rangle$ state depending on whether a Y_{-90} or a Y_{90} gate is applied, see Fig. 6.1(b). In the case of only coherent evolution, the final state will always be $|1\rangle$ (or $|0\rangle$ in the case of the final pulse being Y_{90}). However in the presence of noise the coherence decays exponentially to a mixed state, where the decay constant is proportional to the noise PSD at the Rabi frequency. This frequency is separately measured with a Rabi sequence [Fig. 6.1(a)] which is very similar to the spin-locking sequence. The qubit is initialized in the $|0\rangle$ state followed immediately by the square pulse with the same amplitude, A, as in the case of the spin locking sequence. After τ either first a tomographic pre-rotation is done followed by readout or the qubit state is readout immediately [Fig. 6.1(a)]. The resulting measurement as a function of τ is an oscillation at the Rabi frequency.

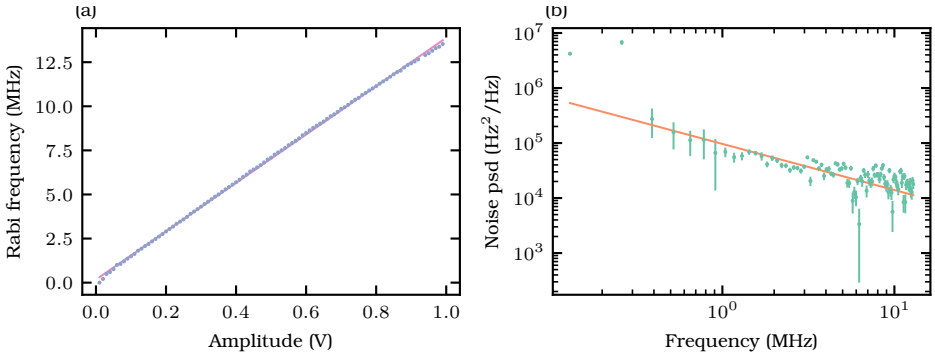

Figure 6.2: Rabi frequency and spin locking noise PSD measurements. (a) Rabi frequency measurements for square pulse amplitudes of 0.01 V to 1.00 V in steps of 0.01 V. The solid line is a linear fit to the data with a coefficient of 13.71 MHz/V and is used in the calibration of the frequency of (b). (b) Spin locking noise PSD measurement with the solid line is a fit to eq. 6.41 with $\alpha = 0.68$

In order to extract the Rabi frequency from these two measurements, the data are fit with a decaying exponential:

$$P|1\rangle(\tau) = A \exp\left(-\frac{\tau}{T_R}\right) \cos\left(2\pi f_R + \varphi_1\right) + O_1, \tag{6.37}$$

$$P|0\rangle(\tau) = -A \exp\left(-\frac{\tau}{T_R}\right) \cos\left(2\pi f_R + \varphi_2\right) + O_2. \tag{6.38}$$

Both $P|1\rangle$ and $P|0\rangle$ are simultaneously fit to the data points in Fig. 6.1(a). In this equation all the parameters that are shared between the two equations, namely the amplitude, A, the decay constant, T_R, and the Rabi frequency, f_R, are fit to both data sets. While the phases, φ_1 and φ_2, and the offsets, O_1 and O_2, are only fit to one data set. The best fit Rabi frequency f_R is then used to calibrate the frequency for the noise PSD and the rest of the parameters are not used.

A similar process is applied to the spin-locking data. The data are fit to is an exponential decay of coherence,

$$\left\langle \sigma_z^{|1\rangle}(\tau) \right\rangle = A_1 \exp\left(-\frac{\tau}{T_{1\rho}}\right) + C_1 + C_2 \tag{6.39}$$

$$\left\langle \sigma_z^{|0\rangle}(\tau) \right\rangle = A_2 \exp\left(-\frac{\tau}{T_{1\rho}}\right) - C_1 + C_2. \tag{6.40}$$

The $\langle \sigma_z \rangle$ value is rescaled to the measured data according to the formula $\left\langle \sigma_z^{|x\rangle} \right\rangle = 2P|x\rangle - 1$ for both the $x = 0$ and $x = 1$ state. The fit is done to

both data simultaneously. Here, A_1 and A_2 are amplitudes of the coherence at $\tau = 0$, $T_{1\rho}$ is the decay constant, $C_1 = \langle\sigma_z(\tau \to \infty)\rangle$ and C_2 is a constant that absorbs any offset in both channels that is present due to a imperfect calibration of the π pulses. A significant deviation of the steady state polarization, $\langle\sigma_z(\tau \to \infty)\rangle$ from zero indicates an asymmetric spectrum. Here, depending on the sign of $\langle\sigma_z(\tau \to \infty)\rangle$, at positive or negative frequencies the PSD is larger than the other. This asymmetry is indicative of either a coherent type of noise [143] or quantum noise [16].

Next, the Rabi frequency is swept by varying the square pulse amplitude and the spin locking sequence is measured. the Rabi frequency is fit for every square pulse amplitude and it provides a calibration from the pulse amplitude in voltage to the Rabi frequency [Fig. 6.2(a)]. The data are fit with a linear relation, yielding a Rabi frequency $f_R/A = 13.71$ MHz/V. This is then used for the frequency calibration of the noise PSD [Fig. 6.2(b)]. The noise PSD at the Rabi frequency is related to the spin locking dephasing rate rate, $S(f_R) = 2\Gamma_{\phi\rho}$, where $\Gamma_{1\rho} = \Gamma_1 + \Gamma_{\phi\rho}$ and $\Gamma_{\phi\rho} = 1/T_{1\rho}$. The resulting noise PSD [Fig. 6.2(b)] is then fit with a power law,

$$S(f_R) = \frac{A}{f^\alpha},$$

where A is the magnitude of the noise at 1 Hz and α defines the shape of the noise spectrum, which is $\alpha = 1$ for $1/f$ noise. However in its current form, it turns out to be difficult to fit the equation to the noise spectrum. This is because of the high correlation, up to 99.8%, between A and α. When α is varied by a small amount the amplitude varies along with it in an almost perfectly correlated way. This effect can be seen in the log-log plot [Fig. 6.2(b)], since the power law becomes a linear relationship. Now α is the slope of the line and A is the intercept of the y-axis at 1 Hz. when the slope of the line is increased a bit, while still being a good fit to the data, the intercept at 1 Hz increases as well. This high correlation gives unreliable fit parameters and makes it impossible to conclude anything from them. The solution is to add a reference point at which the amplitude is evaluated. This reference point determines at which frequency the amplitude, A, is fitted,

$$S(f_R) = \frac{A f_{\text{ref}}^\alpha}{f^\alpha}. \tag{6.41}$$

Here, f_{ref} is the reference point. The reference point is chosen at $f_{\text{ref}} = 2.2$ MHz, the frequency that minimizes the correlation between A and α and works for all fields[Sec. 6.3]. This trick is inspired from the Taylor series of a function, where the approximation to the function is centered around the reference point. It is at this point that the function and its derivatives are evaluated. The first order Taylor series of a function, $T(x) = g(x_c) + \frac{dg}{dx}(x_c)(x - x_c)$, is compared to the logarithm of Eq. 6.41, $\log(S(f_{\text{ref}})) = \log(A) - \alpha(\log(f) - \log(f_{\text{ref}}))$. Here, the role of the reference point x_c is the

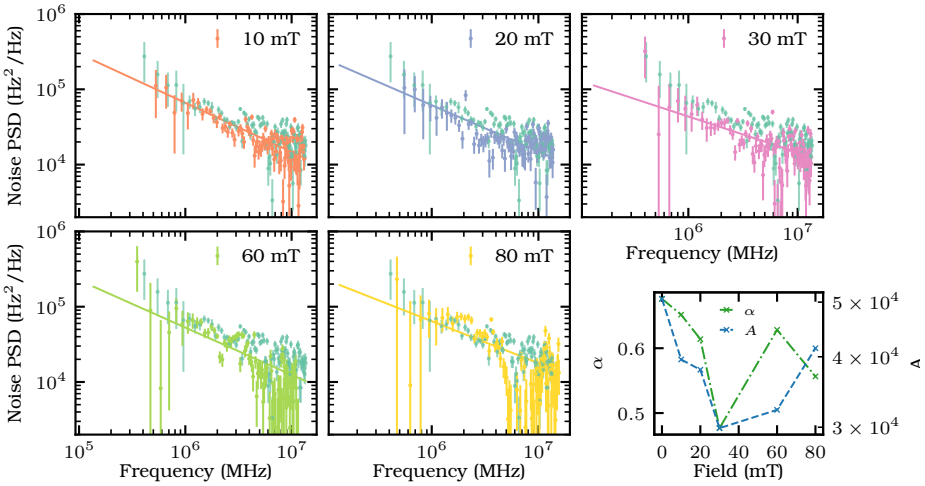

Figure 6.3: Noise PSD with increasing magnetic field. (a-e) For each plot the 0 mT is repeated in order to allow for comparison between the fields. The inset in the bottom right indicates the best fit parameters to Eq. 6.41. The amplitude is evaluated at 2.2 MHz.

same as $\log(f_{\text{ref}})$, the role of the constant offset evaluated at the reference point, $g(x_c)$, is the same as A, the slope $\frac{dg}{dx}(x_c)$ is equivalent to α, and finally x has the same role as $log(f)$. This means that the revised A is now evaluated at the reference point instead of at 1 Hz. However, if necessary the conversion can be easily made by multiplying A by f_{ref}^{α}. The best fit parameters of Eq. 6.41 to the data in Fig. 6.2(b) are $A = (50671 \pm 1340)$ Hz^2/Hz and $\alpha = 0.676 \pm 0.028$ with a correlation coefficient of -18%. This correlation is significantly less than the prior 99.8%.

6.3. Noise spectroscopy in a magnetic field

The flux noise amplitude measured with the echo sequence in chapter 5 increased linearly when the in-plane magnetic field is applied. Now noise spectroscopy using spin-locking is done in a magnetic field to see if it is possible to identify a frequency band where the noise is present. The same procedure as described in the first part of this chapter is repeated for 10, 20, 30, 60 and 80 mT, all measured at the 5 GHz/Φ_0 sensitivity to flux noise [Fig. 6.3]. To be able to compare the different noise PSDs with each other, the zero field PSD is repeated in every subplot. Every trace is fit with the Eq. 6.41 and the best-fit parameters are plotted in the bottom right inset of Fig. 6.3. It turns out that that the the 2 orders of magnitude of noise

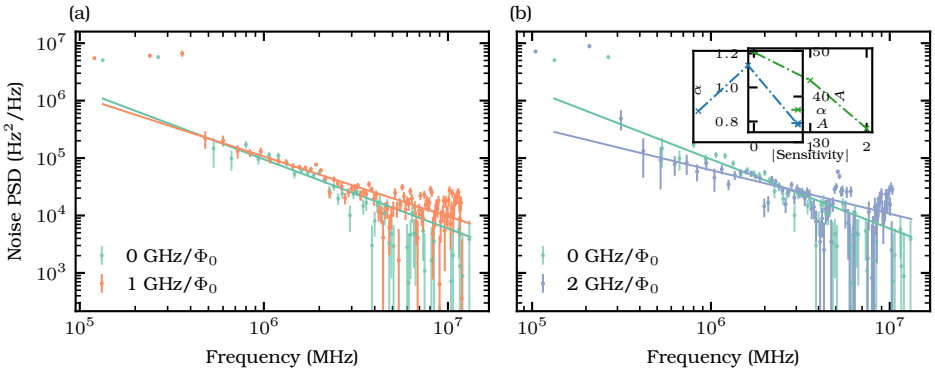

Figure 6.4: Noise PSD measurements with increasing sensitivity. (a) The data for 1 GHz/Φ_0 compared to the data at the sweetspot, with the fit to the data using Eq. 6.41. (b) The data of 2 GHz/Φ_0 compared to 0 GHz/Φ_0 and the fit. The inset shows the best fit parameters, α and A as a function of sensitivity. The fit amplitude A is referenced at 2.2 MHz.

increase in the flux noise amplitude cannot be directly measured in the 0.2-14 MHz frequency band. This can be because of two reasons. First, the flux noise increase can be in a different frequency band than available by the spin locking method. It would be a coincidence and not very likely that the noise being measured is hiding for one particular method but not for the other. However, it is worth it to use a different method to measure the noise PSD in a different frequency band to check if the PSD measurements are consistent.

The other explanation is that the noise in this frequency band is swamped with a different type of noise other than flux noise. When the field is increased the other noise would only be measured and the flux noise is in fact increasing but at a much lower amplitude. From these measurements of the noise PSD, however, it is impossible to tell what type of noise is being monitored. In principle it is possible to do using the third level of the transmon [58]. The idea is that the second level of the transmon is sensitive to different types of noise in a different way allowing to identify the type of measured noise. However, this was not done here.

6.3.1. Noise Spectroscopy at different sensitivities

A different way to check if the PSD is due to flux noise or a different noise type is to vary the sensitivity to flux noise. At 0 GHz/Φ_0 the qubit is insensitive to flux noise. This is a benchmark to compare to when the sensitivity is increased to 2 GHz/Φ_0 in steps of 1 GHz/Φ_0. The data for 1 GHz/Φ_0 and 2 GHz/Φ_0 are compared to the data from 0 GHz/Φ_0 at 80 mT

in Fig.6.4. The noise amplitude for the different sensitivities is around the same, $A \sim 40000\text{Hz}^2/\text{Hz}$. However, the slope of the noise seems to decrease from $\alpha = 1.2$ at the sweetspot to $\alpha = 0.8$ at 1 GHz/Φ_0. The data at lower fields measured at 5 GHz/Φ_0 continue this trend, where the slope of the noise PSD in the log-log plot has decreased to $\alpha \sim 0.6$. Since the amplitude at 2.2 MHz has not changed and the slope decreases, the noise power at lower frequencies should decrease and at higher frequencies increase. In this setup it was not easily possible to measure at higher frequencies, so it was chosen to measure the noise PSD at lower frequencies using a repeated sequence of Ramsey type [140] in the next section.

6.4. Noise spectroscopy using repeated Ramsey type measurements

To extend the frequency range in which it is possible to measure the noise spectral density a different method to the spin locking is needed. The method of choice is a repeated Ramsey [140] type of measurement that extends the frequency range of the noise PSD from the kHz range down to sub 1 Hz.

The measurement starts with a X_{90} pulse followed by a waiting period τ. This waiting period has to be shorter than the T_2^* time. The waiting period is followed by a Y_{90} prior to readout in order to transform a frequency detuning into a bias of the probability to measure the $|1\rangle$ state different from 0.5. Then the qubit is reset to the $|0\rangle$ state by waiting 6 T_1 and the process is repeated. If the fidelity and the quantum non demolition (QND) of the readout is high, it is possible to to the measurement restlessly [145]. In that case a XOR operation has to be done with the previous measurement outcome in order to compensate for the fact that the previous measurement could have been projected onto $|1\rangle$. In this case, the measurements were not done restless because the readout fidelity was not always very high. This block of measurements is repeated for about $N = 2^{20}$ times. First the discrete Fourier transform (DTFT) of the data are taken,

$$\tilde{X}\left(f = \frac{k}{\Delta t}\right) = \frac{1}{2\pi\tau}\sum_{n=0}^{N-1} x(n)\exp\left[2\pi i\frac{nk}{N}\right]. \tag{6.42}$$

The $2\pi\tau$ factor is present to estimate the frequency detuning measured by the Ramsey sequence from the σ_z measurements. The factor in the frequency scaling factor, Δt is the time between two measurements of the sequence. This includes the time the quantum circuit takes as well as the measurement and the initialization time and in this case is about 52.36 µs. The noise PSD can then be calculated, this is sometimes also called a periodogram,

$$S(f) = \frac{\Delta t}{N}\left|\tilde{X}(f)\right|^2. \tag{6.43}$$

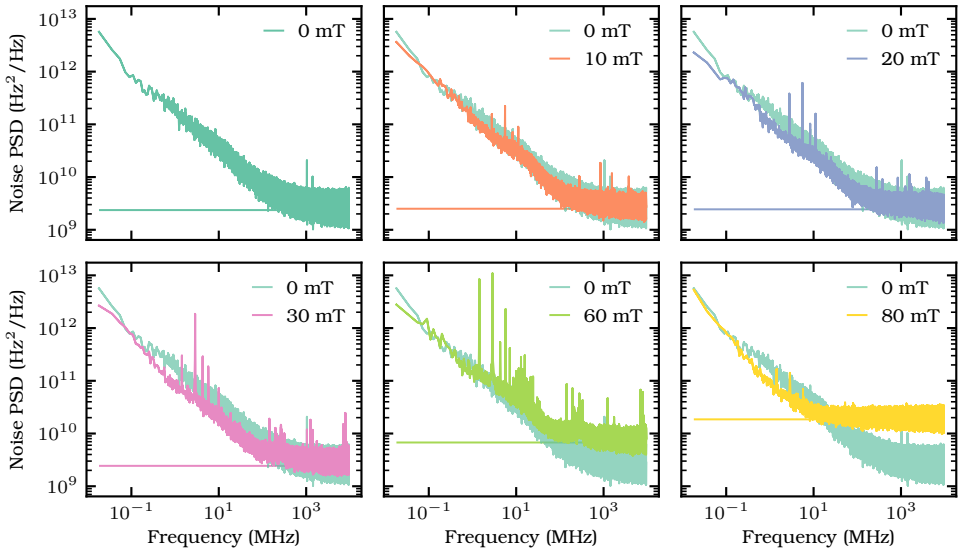

Figure 6.5: Repeated Ramsey measurements for different magnetic fields at 5 GHz/Φ_0. To avoid clutter every noise PSD trace is plotted in a separate figure with the zero field trace as a reference. The increased noise floor for 60 and 80 mT are due to a shorter τ of 60 and 40 ns respectively, while for the other fields a τ of 100 ns is used.

The data as analyzed with these equations are shown in fig. 6.5, where at every field they are compared to the zero field case. Qualitatively the trace is similar at every field to the zero field case. The slope at low frequencies is about the same, while the magnitude of the noise seems a bit lower. At fields above 0 mT sharp peaks appear at integer multiples of 50 Hz, these are the harmonics due to the light net interference somewhere in the system. Additionally peaks appear at harmonics of the 0.7 Hz pulse tube refrigerator frequency. The noise floor of the measurement is indicated with the solid horizontal line for every field in the corresponding color. The noise PSD is white after the noise floor has been met. The resulting noise is due to the discretization of the measurements. This noise PSD is in contrast with the measurements of the $1/f$ flux noise amplitude in Ch 5. There the amplitude increased linearly with field, while here for the lower frequencies the noise stays roughly the same. One possible explanation is that the low frequency noise is not due to flux noise and the increase is not observed. The fact that the noise amplitude seems to go down a little can be due to the lower readout fidelity at higher fields [Sec. 6.6.1]. This has the effect of observing a lower noise PSD.

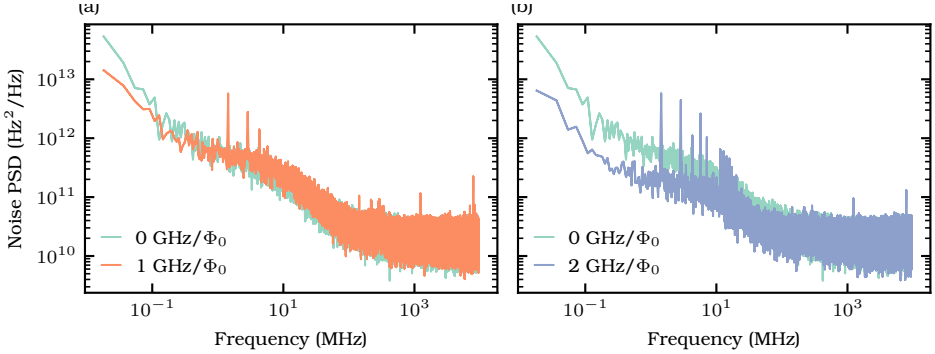

Figure 6.6: Repeated Ramsey measurements at 100 mT for different sensitivities. (a) Comparison of the trace at 1 GHz/Φ_0 in orange to the trace of 0 GHz/Φ_0 in blue. (b) Trace of 2 GHz/Φ_0 compared to 0 GHz/Φ_0. The lowering of the at low frequencies is likely due to due to drift in the qubit frequency.

6.4.1. Repeated Ramsey for increasing sensitivity

One possible check to see if the noise measured is flux noise or not is to adjust the sensitivity to flux noise and observe the noise PSD. If there is flux noise, the PSD should increase when the sensitivity is increased. The measurement for 0 to 2 GHz/Φ_0 is shown in Fig. 6.6. Again in this measurement the PSD decreases away from the quantization noise threshold. If the noise was due to flux noise, it should increase with increased sensitivity, if the noise has the same behavior as in Ch. 5. While if the noise was due to something else it should stay the same, all else being equal. It could be that the noise has different behavior in different frequency bands. It is striking though that the increased noise as measured by the echo measurements could not be found using noise spectroscopy. It turned out that the qubit was slowly drifting with about 2 kHz/s, which over the time of the measurement amounts to about 5 MHz. This drift is due to a non perfect persistent magnet. The current flowing through the magnet slowly decays due to a small resistance in the persistent heat switch. To counteract this the magnet is still supplied by the power supply, while the magnet is in persistent mode. The mismatch between the supply current and the current in the magnet provides the current decay. This decay is less than 5 MHz/h, which allows it to stay undetected for most measurements and it can easily be solved by updating the qubit frequency regularly, which is done for all the other measurements in this thesis except for the repeated Ramsey measurements. This issue was identified and to check the validity of the measurements done in this chapter, they were only averaged over a 1000 s period. This did not substantially change the measured noise PSD, except for the amount of noise on the PSD. The 1000 s period has a maximum

drift of less than 2 MHz at 80 mT, all the other measurements had substantially lower amounts of drift, with the measurements at 30 mT staying below 5 MHz even after 6000 s. Thus the only affected spectra are the ones at 80 mT, especially the sensitivity sweep.

6.5. Conclusion

In this Chapter noise spectroscopy was done using a nanowire transmon in a magnetic field for different sensitivities to flux noise. Spin locking provided noise PSDs in the range of 0.1 to 13 MHz, while repeated Ramsey measurements measured in the range of 0.1-5000 kHz. Both the noise amplitude and power of the $1/f^{\alpha}$ noise did not substantially change in a magnetic field, contrary to what was measured in Chapter 5. The spin-locking measurements provided a easy to analyze and simple to interpret method compared to the more traditional methods like CPMG. The lack of increase in flux noise is in contrast to the echo measurements of Chapter 5 that are sensitive in the same range of frequencies. Also for the lower frequencies of the repeated-Ramsey method there was no observation of the increase in the noise PSD. At these frequencies though the noise can be due to other sources. Another explanation for the repeated-Ramsey measurements at 80 mT for different sensitivities is that there was a drift in the qubit frequency that was not calibrated out. This was checked by only averaging over a small portion of time, which did not substantially change the conclusions. Additionally the noise floor of the repeated-Ramsey method was derived both for perfect readout fidelity as well as finite readout fidelity.

Future experiments can measure the higher excited states in order to dissect the noise source more precisely. The noise coupling to E_J such as flux noise or charge noise coupling to the junction can then be distinguished from photon shot noise [58].

6.6. Discretization noise floor

In order to check if the measurement and data analysis is done correctly it is desirable to know the noise floor from the discretization noise of the measurements. To do this the evolution of the density matrix is tracked along the quantum circuit. After initialization the density matrix is $\rho = |0\rangle\langle 0|$, then the $X_{90} = \frac{1}{\sqrt{2}}\begin{pmatrix} 1 & i \\ -i & 1 \end{pmatrix}$ is applied,

$$\rho_2 = X_{90}\rho X_{90}^{\dagger} = \frac{1}{2}\begin{pmatrix} 1 & i \\ -i & 1 \end{pmatrix}. \tag{6.44}$$

During the free evolution time, due to quasi-static noise there is a detuning present, this can be represented by the Hamiltonian $H = \frac{1}{2}\Delta\omega\sigma_z$, the time evolution operator is $\exp[-iHt]$. The density matrix after the free evolution

time is

$$\rho_3 = \exp[-iHt]\rho_2 \exp[iHt] = \frac{1}{\sqrt{2}}\begin{pmatrix} 1 & ie^{-i\Delta\omega t} \\ -ie^{-i\Delta\omega t} & 1 \end{pmatrix}. \tag{6.45}$$

Now the prereadout rotation is applied to transform the detuning information to the qubit state probability. The final state before redout after the $Y_{90} = \frac{1}{\sqrt{2}}\begin{pmatrix} 1 & 1 \\ -1 & 1 \end{pmatrix}$ is

$$\rho_4 = Y_{90}\rho_3 Y_{90}^{\dagger} = \frac{1}{2}\begin{pmatrix} 1-\sin(\Delta\omega t) & \cos(\Delta\omega t) \\ -\cos(\Delta\omega t) & 1+\sin(\Delta\omega t) \end{pmatrix}. \tag{6.46}$$

The probabilities of measuring the $|0\rangle$ and $|1\rangle$ states are $\mathrm{P}(|0\rangle) = \mathrm{Trace}(M_0\rho_4)$ and $\mathrm{P}(|1\rangle) = \mathrm{Trace}(M_1\rho_4)$ and reflect the detuning due to the quasi-static noise, $\mathrm{P}(|0\rangle) = \frac{1}{2} - \frac{1}{2}\sin(\Delta\omega t)$ and $\mathrm{P}(|1\rangle) = \frac{1}{2} + \frac{1}{2}\sin(\Delta\omega t)$. with the readout matrices given by $M_0 = \begin{pmatrix} 1 & 0 \\ 0 & 0 \end{pmatrix}$ and $M_1 = \begin{pmatrix} 0 & 0 \\ 0 & 1 \end{pmatrix}$. This state is continuously measured with a time spacing of Δt. Now all the prerequisites are there to calculate the power spectral density of this signal. The starting point of the noise spectral density analysis from a theoretical point of view is the Wiener-Kinchin theorem,

$$S_x(k) = \sum_n \mathrm{E}\left[x[n]x[n-k]\right] e^{2\pi i \frac{nk}{N}}. \tag{6.47}$$

This is the Fourier transform of the autocorrelation of the signal. First, the autocorrelation is calculated when $k \neq 0$

$$\begin{aligned} \mathrm{E}\left[x(n)x(n-k)\right] =& 1\cdot 1\cdot\left(\frac{1}{2} - \frac{\sin(\Delta\omega_n t)}{2}\right)\left(\frac{1}{2} - \frac{\sin(\Delta\omega_{n-k} t)}{2}\right) \\ &-1\cdot 1\cdot\left(\frac{1}{2} + \frac{\sin(\Delta\omega_n t)}{2}\right)\left(\frac{1}{2} - \frac{\sin(\Delta\omega_{n-k} t)}{2}\right) \\ &-1\cdot 1\cdot\left(\frac{1}{2} - \frac{\sin(\Delta\omega_n t)}{2}\right)\left(\frac{1}{2} + \frac{\sin(\Delta\omega_{n-k} t)}{2}\right) \\ &+1\cdot 1\cdot\left(\frac{1}{2} + \frac{\sin(\Delta\omega_n t)}{2}\right)\left(\frac{1}{2} + \frac{\sin(\Delta\omega_{n-k} t)}{2}\right) \\ =& \sin(\Delta\omega_n t)\sin(\Delta\omega_{n-k} t), \end{aligned}$$

while for $k = 0$ the expectation value $\mathrm{E}\left[x(n)^2\right]$. For this method to work it is important that the phase acquired during the free evolution time remains small, $\Delta\omega_n t \ll 1$. After this assumption the resulting expectation value is approximately equal to

$$\mathrm{E}\left[x(n)x(n-k)\right] \approx \delta[k] + \Delta\omega_n \tau \Delta\omega_{n-k}\tau. \tag{6.48}$$

This equation can now be substituted into Eq. 6.47 and the DTFT is taken,

$$S_x = \Delta t + \Delta t |\tilde{X}(f)|^2 (2\pi\tau)^2. \tag{6.49}$$

Here, S_x is the PSD of the signal, Δt is the time between two subsequent measurements and τ is the free evolution time. The noise PSD of interest is $\Delta t|\tilde{X}(f)|$, which is not directly measured, but instead it is multiplied with the $(2\pi\tau)^2$ term and there is an additional white discretization noise term. Rearranging terms it the white noise term becomes,

$$S_{\text{white}} = \frac{\Delta t}{(2\pi\tau)^2}. \tag{6.50}$$

From this equation it becomes clear how to make a better noise spectrometer. There are two options, first having a higher sample rate, making Δt smaller. Second having a longer free evolution time τ quadratically reduces the white noise. It is thus desirable to have the longest free evolution time possible, however it is important that the assumption condition, $\Delta\omega\tau \ll 1$ is still maintained.

6.6.1. Noise floor with finite readout fidelity

It is possible to extend this derivation in the case of finite readout fidelity. Assuming there is still no significant decoherence, the finite readout fidelity can be limiting the sensitivity to of the noise spectroscopy method, besides the earlier mentioned limitations. The readout matrices for non perfect readout fidelity are $M_0 = \begin{pmatrix} \sqrt{F} & 0 \\ 0 & \sqrt{1-F} \end{pmatrix}$ and $M_1 = \begin{pmatrix} \sqrt{1-F} & 0 \\ 0 & \sqrt{F} \end{pmatrix}$. The resulting probabilities for measuring the respective states are

$$p_0 = \sqrt{F}\left(\frac{1}{2} - \frac{\sin(\Delta\omega\tau)}{2}\right) + \sqrt{1-F}\left(\frac{1}{2} + \frac{\sin(\Delta\omega\tau)}{2}\right)$$
$$p_1 = \sqrt{1-F}\left(\frac{1}{2} - \frac{\sin(\Delta\omega\tau)}{2}\right) + \sqrt{F}\left(\frac{1}{2} + \frac{\sin(\Delta\omega\tau)}{2}\right)$$

This is similar to the case of perfect readout, however there is a chance of mixing the states up. The corresponding expectation value is

$$\mathrm{E}\left[x(n)x(n-k)\right] = \sin(\Delta\omega_n t)\sin(\Delta\omega_{n-k} t)\left(1 - 2\sqrt{1-F}\right),$$

for $k \neq 0$ and for $k = 0$ the expectation value is $\mathrm{E}\left[x[n]^2\right] = \left(1 + 2\sqrt{1-F}\right)$. Again the assumption is made that the acquired phase is small $\Delta\omega\tau \ll 1$, after taking the DTFT

$$S_x = \Delta t\left(1 + 2\sqrt{1-F}\right) + \Delta t|\tilde{X}(f)|^2(2\pi\tau)^2\left(1 - 2\sqrt{1-F}\right). \tag{6.51}$$

Again the quantity of interest is the noise PSD of the qubit frequency noise, $\Delta t|\tilde{X}(f)|^2$. The reduced fidelity both adds white noise and reduces the visibility of the noise PSD by a factor of $\left(1 - 2\sqrt{1-F}\right)$

7

Conclusion

7.1. Conclusion

In Chapter 3, we have first characterized flux- and gate-tunable nanowire transmons with state-of-the-art T_1 at $B_\parallel = 0$, focusing on quantitative extraction of flux and charge noise coupling to the Josephson energy. We have next investigated the evolution of a gatemon in $B_\parallel$ up to 70 mT, the upper bound set by the closing of the induced gap. Several features of the T_1 and T_2^{Echo} dependence in $B_\parallel$ are not understood yet, inviting further theoretical and experimental investigation.

In Chapter 4 a new method for fabricating airbridges has been developed using GSL. This method allows for the lowering of the fabrication temperature, which is necessary for InAs nanowire Josephson junctions in combination with PMGI. We quantified the change in resistance of these junctions for the two temperatures used by the GSL and reflow methods. Finally we connected the room temperature resistance of the InAs nanowire junctions with a SQUID loop to the operability of a transmon and conclude that a resistance lower than 18 kΩ indicates a high probability of a working qubit. For future work it would be possible to extend this work to other resists that require a lower baking temperature and do not have adhesion problems. Also positive optical resist using for example a direct laser writer can be used in combination with GSL. These methods could bring the highest baking temperature likely all the way down to room temperature.

In Ch. 5 a robust method for measuring the flux noise amplitude was discussed. The Echo dephasing time and the T_1 time were measured as a function of flux bias allowing for the extraction of the dephasing rate. In parallel the qubit spectrum was measured and this provided the sensitivity to flux noise via the calibrated qubit frequency to sensitivity map. This map was obtained from a fit to the spectrum that was redone for every magnetic field. The decay of the echo measurement was analyzed in two different ways. One method took the $1/e$ time, subtracted the T_1 contribution and then plotted the resulting time as a function of sensitivity. The resulting data were fit with a quadratic yielding the $1/f$ flux noise amplitude the white noise amplitude and an offset. The other method fitted the data using both an exponential and a Gaussian. The Gaussian corresponds to $1/f$ flux noise, while the exponential contains both white noise and the T_1 contribution. After subtracting the T_1 contribution of the exponential part both were plotted against sensitivity. The Gaussian part was fitted with a line and the exponential part with a quadratic. This procedure was then done for all magnetic fields and the data collected. It turned out that the $1/f$ flux noise amplitude increased linearly with magnetic field. This means a quadratic increase in the noise power, which is significant and unexpected. A perhaps naive model would expect the fluctuating spins to be polarized and the energy difference in a magnetic field to be prohibitively large to fluctuate to a higher energy state based on the available thermal energy. This measurement is one of the first to measure the flux noise amplitude in a magnetic field, with the data from [36] being the other one. In their

work the flux noise amplitude also increased linearly. Currently we do not understand why the flux noise increases as a function of magnetic field. Perhaps the quantization axis due to the magnetic field is in a different direction than the coupling to the SQUID loop. Or maybe the magnetic field allows for nuclear spins to participate in the flux noise. This however is just speculation.

The maximum field that the qubit spectrum could be measured with high quality at was 140 mT. This was due to a combination of the qubit lowering in frequency and flux jumps in both the resonator and the qubit. The lower frequency of the qubit was due to a misalignment of the nanowire axis with the magnetic field axis. During a later cooldown we did align the magnetic field with the nanowire axis. However due to problems with both the qubit and the cryostat, the data taken during that cooldown was of substantially lower quality.

In Chapter 6 noise spectroscopy was done using a nanowire transmon in a magnetic field for different sensitivities to flux noise. Spin locking provided noise PSDs in the range of 0.1 to 13 MHz, while repeated Ramsey measurements measured in the range of 0.1-5000 kHz. Both the noise amplitude and power of the $1/f^{\alpha}$ noise did not substantially change in a magnetic field, contrary to what was measured in Chapter 5. The spin-locking measurements provided a easy to analyze and simple to interpret method compared to the more traditional methods like CPMG. The lack of increase in flux noise is in contrast to the echo measurements of Chapter 5 that are sensitive in the same range of frequencies. Also for the lower frequencies of the repeated-Ramsey method there was no observation of the increase in the noise PSD. At these frequencies though the noise can be due to other sources. Another explanation for the repeated-Ramsey measurements at 80 mT for different sensitivities is that there was a drift in the qubit frequency that was not calibrated out. This was checked by only averaging over a small portion of time, which did not substantially change the conclusions. Additionally the noise floor of the repeated-Ramsey method was derived both for perfect readout fidelity as well as finite readout fidelity.

Future experiments can measure the higher excited states in order to dissect the noise source more precisely. The noise coupling to E_J such as flux noise or charge noise coupling to the junction can then be distinguished from photon shot noise [58].

7.1.1. Discussion

This section discusses the project with the advantage of having been through the journey and having the experience. What decisions would I have done again and what would I have done differently. There are two main parts of the project: The nanowire and the magnetic field to measure the flux noise. Both the nanowire transmon and coherent qubits in a magnetic field were new at the start of the project. A flux tunable transmon had never even been done in a magnetic field even with an SIS transmon. This required in-

novation on two fronts, which made the project challenging. The nanowire posed problems that the conventional SIS transmon does not suffer from. One particular example of this is that the nanowire changes E_J in every cool-down. Even with a thermal cycle to 4K and back the E_J changes. In general the E_J and therefore the qubit frequency went up every time a thermal cycle was done. This in combination with frequent failures of the cooling water of the pulse tube compressor meant that thermal cycles were abundant. This meant that the qubit frequency at some point was so high it was difficult to measure and not possible to do the experiment. Besides this issue maybe the nanowire is not the most suitable Josephson junction for the project. The semiconductor is sensitive to charges on its surface that couple to E_J. This means that there is an additional source of dephasing and on top of that there are frequent. In the flux noise in a magnetic field experiments the Ramsey time was never higher than 500 ns. This noise can be differentiated from flux noise by changing the sensitivity, but having a Ramsey time more similar to the Echo time and also be sensitive to flux noise would definitely be better. Another downside of the nanowire is that the magnetic field compatibility is only maximal along the nanowire axis, meaning that there is an extra alignment needing to be done. In my opinion it may have been better to first try the experiment with thin aluminum SIS junctions. This would also require some cleanroom development, but I think that the physics and the engineering would be easier. The SIS junction also obeys the Ambegaokar-Baratoff relation making engineering of the junction simpler. If the junction would have been changed the project only required making the flux tunable transmon coherent in a magnetic field. This I think could have been done faster than what is required for the nanowire junction.

One of the promises of the semiconductor Josephson junction is that there is new physics to be found. So is there any use for a SNS transmon in my opinion? The answer is yes, but not in terms of a conventional transmon. The exact same type of nanowire is used in many studies, such as for the Majorana fermion or for Andreev bound state research. Recently the spin in a quantum dot in the Josephson junction of the transmon has been studied. This type of research where the focus is on the physics of the nanowire is where it performs best. Using a gate tunable SNS transmon is in my opinion not the best idea. The gate is noisier and not as reproducible as the flux tunability. On top of this due to the universal conductance fluctuations the qubit frequency is not predictable as a function of gate bias. Flux tunability clearly has the advantage here. When gate tunability is not an advantage it is better not to have it. This makes an SNS transmon unlikely to be used in quantum computation. This assessment holds of course only with current and imperfect knowledge of the field.

Besides the Josephson junction I think there is a good future for experiments using cQED in a magnetic field. The flux jumps that occur in the resonator may be a deal breaker for some experiments, but for most it can be worked around. A significant portion of this work was dedicated to mak-

ing the flux tunable transmon magnetic field compatible. In the beginning the magnetic field introduced a lot of noise and a lack of shielding from the magnet raised the temperature of the chip significantly. These problems were eventually all overcome yielding a coherent and magnetic field compatible qubit. Future work can improve on this by exploring higher magnetic field using SIS transmon qubits. Additionally more noise spectroscopy can be done after learning the lessons from this work.

7.2. Outlook

Having learned the results of the experiment, what could be a next step in the experimental investigation of flux noise. I still think that applying a magnetic field and measuring the flux noise is a good idea. Future experiments should focus on the noise PSD, to see if the increase in flux noise amplitude as seen with the echo measurements can be accounted for. One problem is that it may be difficult to identify the noise source of the PSD that is measured. One possible solution is to use the higher levels, the $|2\rangle$ state and above. Each level reacts different to a particular noise source, where the noise PSD depends on the square of the sensitivity to the noise source. Here, we look at 3 noise sources and their impact on the second exited state. This section is

7.2.1. Flux noise and Josephson energy noise

There are two noise types for the SNS transmon that couple to the Josephson energy: Charge noise and flux noise. In future experiments it is desirable that charge noise coupling to E_J does not play a role for noise spectroscopy. This can be done by switching the junction from the SNS nanowire to a SIS junction. The SIS junction typically does not suffer from E_J noise. Since the transmon is very close to being a harmonic oscillator, with equally spaced levels, the sensitivity to E_J noise is the same for every neighbouring transition. The anharmonicity does not play a role here, because it is mostly constant near the high frequency sweetspot. Both charge noise and flux noise couple the same to the $|0\rangle - |1\rangle$ and $|1\rangle - |2\rangle$ transition. So for an SIS transmon the ratio of sensitivities the same and the ratio of flux noise PSD is [58]

$$\frac{S_\Phi^{|0\rangle-|1\rangle}}{S_\Phi^{|1\rangle-|2\rangle}} = 1. \tag{7.52}$$

This expression is constant, so there is no frequency dependent change in the noise PSD. This means that if the pure dephasing time, as measured for example with an echo measurement, is the same for higher transitions as the $|0\rangle - |1\rangle$ transition, the noise is due to flux noise.

7.2.2. Photon shot noise

Photon shot noise occurs when photons randomly enter and leave the readout resonator of the transmon. This process depends on the average number of photons in the cavity and the dispersive shift (see Sec. 2.5.3). Since the coupling of the higher transmon levels to the resonator is larger than for the lowest transition, the noise PSD is larger for the higher levels. There are additional effects, such as the detuning to the resonator being different for the higher levels due to the anharmonicity. The photon shot noise PSD for the $|1\rangle - |2\rangle$ transition relative to the $|0\rangle - |1\rangle$ transition [58]

$$\frac{S_{\bar{n}}^{|0\rangle-|1\rangle}}{S_{\bar{n}}^{|1\rangle-|2\rangle}} = \left(\frac{\chi^{|1\rangle-|2\rangle}}{\chi^{|0\rangle-|1\rangle}}\right)^2. \tag{7.53}$$

where the ratio on the right hand side is larger than one. The coupling between the resonator and transmon in rough terms goes as $\sqrt{n}$, where n is the transmon level. The ratio of the noise PSD is thus roughly proportional to transition of interest. In practise it will deviate from this rough approximation, however this fact allows us to distinguish flux noise and photon shot noise.

7.2.3. Charge tunnelling and charge dispersion

Dephasing due to charge noise is a quasiparticle tunnelling through the junction to the transmon capacitive island. The transmon is naturally insensitive to this type of noise, especially for large E_J/E_C ratios. Additionally if the charge offset term in the Hamiltonian is close to 0.5e, the noise PSD goes to zero. However for the majority of transmons the charge offset parameter is uncontrolled, so in general this noise source is still present [56]. Additionally the frequency difference for the two charge states grows exponentially with the level of the transmon. This means that it becomes more important for the higher levels, regardless of the E_J/E_C ratio. The fact that the charge parity only has two values, means that the noise PSD is Lorentzian. For a strongly coupled TLS, if the tunnelling rate is much lower than the dephasing rate, a Ramsey measurement will show a beating pattern. If the tunnelling rate is faster than the qubit relation rate, the qubit will dephase at the rate set by the tunnelling rate of the quasiparticle. In that case the noise PSD is white. However photon shot noise can also be white, so it can be helpful to see how the higher levels of the transmon are affected to quasiparticle tunnelling. The magnitude of the splitting of each level is given in Sec. 2.5.1. The ratio of the differences is given by

$$\frac{S_{\mathrm{qp}}^{|0\rangle-|1\rangle}}{S_{\mathrm{qp}}^{|1\rangle-|2\rangle}} = 16\frac{E_J}{E_C}. \tag{7.54}$$

This ratio is reduced by n for the higher levels, meaning that the factor at some point goes below 1 and there is a maximum in the charge dispersion

magnitude. However, since this ratio is relatively constant, the higher levels are exponentially more hit by charge dispersion.

In conclusion, these three different noise sources can sometimes be hard to distinguish. Therefore it helps to look at the higher transitions and see how the dephasing rate changes. This may help to isolate the flux noise contribution to the noise PSD from other sources and more accurately track it as a function of the flux bias and sensitivity to flux noise. This works for both the echo measurements as well as the noise spectroscopy measurements.

Bibliography

[1] S. Krinner *et al.* 'Realizing repeated quantum error correction in a distance-three surface code'. In: *Nature* 605.7911 (2022), pp. 669–674. url: https://doi.org/10.1038/s41586-022-04566-8.

[2] Y. Zhao *et al.* 'Realization of an Error-Correcting Surface Code with Superconducting Qubits'. In: *Phys. Rev. Lett.* 129 (3 2022), p. 030501. url: https://link.aps.org/doi/10.1103/PhysRevLett.129.030501.

[3] R. Acharya, I. Aleiner, R. Allen, T. I. Andersen, M. Ansmann, F. Arute, K. Arya, A. Asfaw, J. Atalaya, R. Babbush *et al.* 'Suppressing quantum errors by scaling a surface code logical qubit'. In: *arXiv preprint* (2022). url: https://arxiv.org/abs/2207.06431.

[4] L. DiCarlo *et al.* 'Demonstration of two-qubit algorithms with a superconducting quantum processor'. In: *Nature* 460 (2009), p. 240. url: http://www.nature.com/nature/journal/v460/n7252/abs/nature08121.html.

[5] F. W. Strauch, P. R. Johnson, A. J. Dragt, C. J. Lobb, J. R. Anderson and F. C. Wellstood. 'Quantum Logic Gates for Coupled Superconducting Phase Qubits'. In: *Phys. Rev. Lett.* 91 (2003), p. 167005. url: https://journals.aps.org/prl/abstract/10.1103/PhysRevLett.91.167005.

[6] S. S. Hong, A. T. Papageorge, P. Sivarajah, G. Crossman, N. Didier, A. M. Polloreno, E. A. Sete, S. W. Turkowski, M. P. da Silva and B. R. Johnson. 'Demonstration of a parametrically activated entangling gate protected from flux noise'. In: *Phys. Rev. A* 101 (1 2020), p. 012302. url: https://link.aps.org/doi/10.1103/PhysRevA.101.012302.

[7] R. Barends *et al.* 'Diabatic Gates for Frequency-Tunable Superconducting Qubits'. In: *Phys. Rev. Lett.* 123 (21 2019), p. 210501. url: https://link.aps.org/doi/10.1103/PhysRevLett.123.210501.

[8] M. A. Rol *et al.* 'Fast, High-Fidelity Conditional-Phase Gate Exploiting Leakage Interference in Weakly Anharmonic Superconducting Qubits'. In: *Phys. Rev. Lett.* 123 (2019), p. 120502. url: https://journals.aps.org/prl/abstract/10.1103/PhysRevLett.123.120502.

[9] S. A. Caldwell *et al.* 'Parametrically Activated Entangling Gates Using Transmon Qubits'. In: *Phys. Rev. A* 10 (3 2018), p. 034050. url: https://link.aps.org/doi/10.1103/PhysRevApplied.10.034050.

[10] A. Noguchi, A. Osada, S. Masuda, S. Kono, K. Heya, S. P. Wolski, H. Takahashi, T. Sugiyama, D. Lachance-Quirion and Y. Nakamura. 'Fast parametric two-qubit gates with suppressed residual interaction using the second-order nonlinearity of a cubic transmon'. In: *Phys. Rev. A* 102 (6 2020), p. 062408. url: https://link.aps.org/doi/10.1103/PhysRevA.102.062408.

[11] F. Wellstood, C. Urbina and J. Clarke. 'Excess noise in dc SQUIDs from 4.2 K to 0.022 K'. In: *IEEE transactions on magnetics* 23.2 (1987), pp. 1662–1665. url: https://ieeexplore.ieee.org/document/1065021.

[12] F. Yoshihara, K. Harrabi, A. O. Niskanen, Y. Nakamura and J. S. Tsai. 'Decoherence of Flux Qubits due to 1/f Flux Noise'. In: *Phys. Rev. Lett.* 97 (2006), p. 167001.

[13] R. C. Bialczak *et al.* '1/f Flux Noise in Josephson Phase Qubits'. In: *Phys. Rev. Lett.* 99 (18 2007), p. 187006. url: https://link.aps.org/doi/10.1103/PhysRevLett.99.187006.

[14] S. Sendelbach, D. Hover, A. Kittel, M. Mück, J. M. Martinis and R. McDermott. 'Magnetism in SQUIDs at Millikelvin Temperatures'. In: *Phys. Rev. Lett.* 100 (22 2008), p. 227006. url: https://link.aps.org/doi/10.1103/PhysRevLett.100.227006.

[15] P. Kumar, S. Sendelbach, M. Beck, J. Freeland, Z. Wang, H. Wang, C. Y. Clare, R. Wu, D. Pappas and R. McDermott. 'Origin and reduction of 1/f magnetic flux noise in superconducting devices'. In: *Phys. Rev. App.* 6.4 (2016), p. 041001. url: https://doi.org/10.1103/PhysRevApplied.6.041001.

[16] C. M. Quintana *et al.* 'Observation of Classical-Quantum Crossover of 1/f Flux Noise and Its Paramagnetic Temperature Dependence'. In: *Phys. Rev. Lett.* 118 (5 2017), p. 057702. url: http://link.aps.org/doi/10.1103/PhysRevLett.118.057702.

[17] J. Braumüller *et al.* 'Characterizing and Optimizing Qubit Coherence Based on SQUID Geometry'. In: *Phys. Rev. Applied* 13 (5 2020), p. 054079. url: https://link.aps.org/doi/10.1103/PhysRevApplied.13.054079.

[18] L. Faoro and L. B. Ioffe. 'Microscopic Origin of Low-Frequency Flux Noise in Josephson Circuits'. In: *Phys. Rev. Lett.* 100 (22 2008), p. 227005. url: https://link.aps.org/doi/10.1103/PhysRevLett.100.227005.

[19] S. LaForest and R. de Sousa. 'Flux-vector model of spin noise in superconducting circuits: Electron versus nuclear spins and role of phase transition'. In: *Phys. Rev. B* 92 (5 2015), p. 054502. url: https://link.aps.org/doi/10.1103/PhysRevB.92.054502.

[20] H. Wang, C. Shi, J. Hu, S. Han, C. C. Yu and R. Q. Wu. 'Candidate Source of Flux Noise in SQUIDs: Adsorbed Oxygen Molecules'. In: *Phys. Rev. Lett.* 115 (7 2015), p. 077002. url: https://link.aps.org/doi/10.1103/PhysRevLett.115.077002.

[21] S. Choi, D.-H. Lee, S. G. Louie and J. Clarke. 'Localization of Metal-Induced Gap States at the Metal-Insulator Interface: Origin of Flux Noise in SQUIDs and Superconducting Qubits'. In: *Phys. Rev. Lett.* 103 (19 2009), p. 197001. url: https://link.aps.org/doi/10.1103/PhysRevLett.103.197001.

[22] D. Poulin, A. Kitaev, D. S. Steiger, M. B. Hastings and M. Troyer. 'Quantum Algorithm for Spectral Measurement with a Lower Gate Count'. In: *Phys. Rev. Lett.* 121 (1 2018), p. 010501. url: https://link.aps.org/doi/10.1103/PhysRevLett.121.010501.

[23] T. M. Hazard, A. Gyenis, A. Di Paolo, A. T. Asfaw, S. A. Lyon, A. Blais and A. A. Houck. 'Nanowire Superinductance Fluxonium Qubit'. In: *Phys. Rev. Lett.* 122 (1 2019), p. 010504. url: https://link.aps.org/doi/10.1103/PhysRevLett.122.010504.

[24] F. Yan *et al.* 'The flux qubit revisited to enhance coherence and reproducibility'. In: *Nat. Commun.* 7.1 (2016). url: http://dx.doi.org/10.1038/ncomms12964.

[25] P. Brooks, A. Kitaev and J. Preskill. 'Protected gates for superconducting qubits'. In: *Phys. Rev. A* 87 (5 2013), p. 052306. url: https://link.aps.org/doi/10.1103/PhysRevA.87.052306.

[26] P. Groszkowski, A. D. Paolo, A. L. Grimsmo, A. Blais, D. I. Schuster, A. A. Houck and J. Koch. 'Coherence properties of the 0-π qubit'. In: *New Journal of Physics* 20.4 (2018), p. 043053. url: https://dx.doi.org/10.1088/1367-2630/aab7cd.

[27] A. D. Paolo, A. L. Grimsmo, P. Groszkowski, J. Koch and A. Blais. 'Control and coherence time enhancement of the 0–π qubit'. In: *New Journal of Physics* 21.4 (2019), p. 043002. url: https://dx.doi.org/10.1088/1367-2630/ab09b0.

[28] A. Gyenis, P. S. Mundada, A. Di Paolo, T. M. Hazard, X. You, D. I. Schuster, J. Koch, A. Blais and A. A. Houck. 'Experimental Realization of a Protected Superconducting Circuit Derived from the 0–π Qubit'. In: *PRX Quantum* 2 (1 2021), p. 010339. url: https://link.aps.org/doi/10.1103/PRXQuantum.2.010339.

[29] A. Wallraff, D. I. Schuster, A. Blais, L. Frunzio, R.-S. Huang, J. Majer, S. Kumar, S. M. Girvin and R. J. Schoelkopf. 'Strong coupling of a single photon to a superconducting qubit using circuit quantum electrodynamics'. In: *Nature* 431 (2004), pp. 162–167. url: http://www.nature.com/nature/journal/v431/n7005/abs/nature02851.html.

[30] J. Koch, T. M. Yu, J. Gambetta, A. A. Houck, D. I. Schuster, J. Majer, A. Blais, M. H. Devoret, S. M. Girvin and R. J. Schoelkopf. 'Charge-insensitive qubit design derived from the Cooper pair box'. In: *Phys. Rev. A* 76 (2007), p. 042319. url: http://journals.aps.org/pra/abstract/10.1103/PhysRevA.76.042319.

[31] N. Muthusubramanian, A. Bruno, B. Tarasinski, A. Fognini, R. Hagen and L. DiCarlo. 'Local trimming of transmon qubit frequency by laser annealing of Josephson junctions'. In: *Bulletin of the American Physical Society*. 2019, B29–015.

[32] E. J. Zhang *et al.* 'High-performance superconducting quantum processors via laser annealing of transmon qubits'. In: *Sci. Adv.* 8.19 (2022), eabi6690. url: https://www.science.org/doi/abs/10.1126/sciadv.abi6690.

[33] J. Hertzberg, E. Zhang, S. Rosenblatt, E. Magesan, J. Smolin, J. Yau *et al.* 'Laser-annealing Josephson junctions for yielding scaled-up superconducting quantum processors'. In: *npj Quantum Inf.* 7.1 (2021), pp. 1–8. url: https://doi.org/10.1038/s41534-021-00464-5.

[34] A. Bilmes, A. K. Händel, S. Volosheniuk, A. V. Ustinov and J. Lisenfeld. 'In-situ bandaged Josephson junctions for superconducting quantum processors'. In: *Superconductor Science and Technology* 34.12 (2021), p. 125011. url: https://iopscience.iop.org/article/10.1088/1361-6668/ac2a6d.

[35] A. Schneider, T. Wolz, M. Pfirrmann, M. Spiecker, H. Rotzinger, A. V. Ustinov and M. Weides. 'Transmon qubit in a magnetic field: Evolution of coherence and transition frequency'. In: *Phys. Rev. Research* 1 (2 2019), p. 023003. url: https://link.aps.org/doi/10.1103/PhysRevResearch.1.023003.

[36] J. Krause, C. Dickel, E. Vaal, M. Vielmetter, J. Feng, R. Bounds, G. Catelani, J. M. Fink and Y. Ando. 'Magnetic Field Resilience of Three-Dimensional Transmons with Thin-Film Al/AlO_x/Al Josephson Junctions Approaching 1 T'. In: *Phys. Rev. Applied* 17 (3 2022), p. 034032. url: https://link.aps.org/doi/10.1103/PhysRevApplied.17.034032.

[37] T. Hyart, B. van Heck, I. C. Fulga, M. Burrello, A. R. Akhmerov and C. W. J. Beenakker. 'Flux-controlled quantum computation with Majorana fermions'. In: *Phys. Rev. B* 88 (3 2013), p. 035121. url: http://link.aps.org/doi/10.1103/PhysRevB.88.035121.

[38] V. Mourik, K. Zuo, S. M. Frolov, S. R. Plissard, E. P. A. M. Bakkers and L. P. Kouwenhoven. 'Signatures of Majorana Fermions in Hybrid Superconductor-Semiconductor Nanowire Devices'. In: *Science* 336.6084 (2012), pp. 1003–1007. url: https://www.science.org/doi/abs/10.1126/science.1222360.

[39] G. de Lange, B. van Heck, A. Bruno, D. J. van Woerkom, A. Geresdi, S. R. Plissard, E. P. A. M. Bakkers, A. R. Akhmerov and L. DiCarlo. 'Realization of Microwave Quantum Circuits Using Hybrid Superconducting-Semiconducting Nanowire Josephson Elements'. In: *Phys. Rev. Lett.* 115 (2015), p. 127002.

[40] T. W. Larsen, K. D. Petersson, F. Kuemmeth, T. S. Jespersen, P. Krogstrup, J. Nygård and C. M. Marcus. 'Semiconductor-Nanowire-Based Superconducting Qubit'. In: *Phys. Rev. Lett.* 115 (2015), p. 127001. url: https://doi.org/10.1103/PhysRevLett.115.127001.

[41] L. Casparis, T. W. Larsen, M. S. Olsen, F. Kuemmeth, P. Krogstrup, J. Nygård, K. D. Petersson and C. M. Marcus. 'Gatemon Benchmarking and Two-Qubit Operations'. In: *Phys. Rev. Lett.* 116.15 (2016), p. 150505. url: https://link.aps.org/doi/10.1103/PhysRevLett.116.150505.

[42] F. Luthi *et al.* 'Evolution of nanowire transmon qubits and their coherence in a magnetic field'. In: *Phys. Rev. Lett.* 120.10 (2018), p. 100502. url: https://doi.org/10.1103/PhysRevLett.120.100502.

[43] J. Kroll *et al.* 'Magnetic-Field-Resilient Superconducting Coplanar-Waveguide Resonators for Hybrid Circuit Quantum Electrodynamics Experiments'. In: *Phys. Rev. Applied* 11 (6 2019), p. 064053. url: https://link.aps.org/doi/10.1103/PhysRevApplied.11.064053.

[44] S. Park and A. L. Yeyati. 'Andreev spin qubits in multichannel Rashba nanowires'. In: *Phys. Rev. B* 96 (12 2017), p. 125416. url: https://link.aps.org/doi/10.1103/PhysRevB.96.125416.

[45] B. van Heck, J. I. Väyrynen and L. I. Glazman. 'Zeeman and spin-orbit effects in the Andreev spectra of nanowire junctions'. In: *Phys. Rev. B* 96 (7 2017), p. 075404. url: https://link.aps.org/doi/10.1103/PhysRevB.96.075404.

[46] C. W. Groth, M. Wimmer, A. R. Akhmerov and X. Waintal. 'Kwant: a software package for quantum transport'. In: *New Journal of Physics* 16.6 (2014), p. 063065. url: https://doi.org/10.1088/1367-2630/16/6/063065.

[47] C. W. J. Beenakker. 'Universal limit of critical-current fluctuations in mesoscopic Josephson junctions'. In: *Phys. Rev. Lett.* 67.27 (1991), pp. 3836–3839. url: http://link.aps.org/doi/10.1103/PhysRevLett.67.3836 (visited on 22/11/2013).

[48] Y. Nazarov and J. Danon. *Advanced Quantum Mechanics*. 1st. Cambridge University Press, 2013.

[49] L. B. Nguyen, Y.-H. Lin, A. Somoroff, R. Mencia, N. Grabon and V. E. Manucharyan. 'High-Coherence Fluxonium Qubit'. In: *Phys. Rev. X* 9 (4 2019), p. 041041. url: https://link.aps.org/doi/10.1103/PhysRevX.9.041041.

[50] N. Earnest *et al.* 'Realization of a System with Metastable States of a Capacitively Shunted Fluxonium'. In: *Phys. Rev. Lett.* 120 (15 2018), p. 150504. url: https://link.aps.org/doi/10.1103/PhysRevLett.120.150504.

[51] U. Vool *et al.* 'Driving Forbidden Transitions in the Fluxonium Artificial Atom'. In: *Phys. Rev. A* 9 (5 2018), p. 054046. url: https://link.aps.org/doi/10.1103/PhysRevApplied.9.054046.

[52] M. T. Bell, J. Paramanandam, L. B. Ioffe and M. E. Gershenson. 'Protected Josephson Rhombus Chains'. In: *Phys. Rev. Lett.* 112 (16 2014), p. 167001. url: https://link.aps.org/doi/10.1103/PhysRevLett.112.167001.

[53] T. W. Larsen, K. D. Petersson, F. Kuemmeth, T. S. Jespersen, P. Krogstrup, J. Nygård and C. M. Marcus. Submitted.

[54] A. Y. Kitaev. 'Unpaired Majorana fermions in quantum wires'. In: *Physics-uspekhi* 44.10S (2001), p. 131.

[55] J. Bylander, S. Gustavsson, F. Yan, F. Yoshihara, K. Harrabi, G. Fitch, D. G. Cory, Y. Nakamura, J.-S. Tsai and W. D. Oliver. 'Noise spectroscopy through dynamical decoupling with a superconducting flux qubit'. In: *Nat. Phys.* 7 (2011), p. 565. url: http://www.nature.com/doifinder/10.1038/nphys1994.

[56] D. Ristè, C. C. Bultink, M. J. Tiggelman, R. N. Schouten, K. W. Lehnert and L. DiCarlo. 'Millisecond charge-parity fluctuations and induced decoherence in a superconducting transmon qubit'. In: *Nat. Commun.* 4 (2013), p. 1913. url: http://www.nature.com/articles/ncomms2936.

[57] P. Krantz, M. Kjaergaard, F. Yan, T. P. Orlando, S. Gustavsson and W. D. Oliver. 'A quantum engineer's guide to superconducting qubits'. In: *App. Phys. Rev.* 6.2 (2019), p. 021318. url: https://aip.scitation.org/doi/10.1063/1.5089550.

[58] Y. Sung *et al.* 'Multi-level quantum noise spectroscopy'. In: *Nature Communications* 12.1 (2021), p. 967. url: https://doi.org/10.1038/s41467-021-21098-3.

7

[59] R. H. Koch, D. P. DiVincenzo and J. Clarke. 'Model for $1/f$ Flux Noise in SQUIDs and Qubits'. In: *Phys. Rev. Lett.* 98 (26 2007), p. 267003. url: https://link.aps.org/doi/10.1103/PhysRevLett.98.267003.

[60] R. de Sousa. 'Dangling-bond spin relaxation and magnetic $1/f$ noise from the amorphous-semiconductor/oxide interface: Theory'. In: *Phys. Rev. B* 76 (24 2007), p. 245306. url: https://link.aps.org/doi/10.1103/PhysRevB.76.245306.

[61] D. Lee, J. L. DuBois and V. Lordi. 'Identification of the Local Sources of Paramagnetic Noise in Superconducting Qubit Devices Fabricated on $\alpha-Al_2\mathbf{O}_3$ Substrates Using Density-Functional Calculations'. In: *Phys. Rev. Lett.* 112 (1 2014), p. 017001. url: https://link.aps.org/doi/10.1103/PhysRevLett.112.017001.

[62] Z. Chen and C. C. Yu. 'Comparison of Ising Spin Glass Noise to Flux and Inductance Noise in SQUIDs'. In: *Phys. Rev. Lett.* 104 (24 2010), p. 247204. url: https://link.aps.org/doi/10.1103/PhysRevLett.104.247204.

[63] J. Wu and C. C. Yu. 'Modeling Flux Noise in SQUIDs due to Hyperfine Interactions'. In: *Phys. Rev. Lett.* 108 (24 2012), p. 247001. url: https://link.aps.org/doi/10.1103/PhysRevLett.108.247001.

[64] A. Blais, R.-S. Huang, A. Wallraff, S. M. Girvin and R. J. Schoelkopf. 'Cavity quantum electrodynamics for superconducting electrical circuits: An architecture for quantum computation'. In: *Phys. Rev. A* 69 (2004), p. 062320. url: https://link.aps.org/doi/10.1103/PhysRevA.69.062320.

[65] B. D. Josephson. 'Possible new effects in superconductive tunnelling'. In: *Phys. Lett.* 1.7 (1962), pp. 251–253. url: https://www.sciencedirect.com/science/article/abs/pii/0031916362913690.

[66] Y. Nakamura, Y. Pashkin and J. Tsai. 'Coherent control of macroscopic quantum states in a single-Cooper-pair box'. In: *Nature* 398 (1999), p. 786. url: http://www.nature.com/nature/journal/v398/n6730/abs/398786a0.html.

[67] R. Barends *et al.* 'Superconducting quantum circuits at the surface code threshold for fault tolerance.' In: *Nature* 508.7497 (2014), p. 500. url: http://www.nature.com/nature/journal/v508/n7497/abs/nature13171.html.

[68] L. Steffen, Y. Salathe, M. Oppliger, P. Kurpiers, M. Baur, C. Lang, C. Eichler, G. Puebla-Hellmann, A. Fedorov and A. Wallraff. 'Deterministic quantum teleportation with feed-forward in a solid state system.' In: *Nature* 500.7462 (2013), pp. 319–22. url: http://dx.doi.org/10.1038/nature12422.

[69] M. Jerger *et al.* 'Contextuality without nonlocality in a superconducting quantum system'. In: *Nat. Commun.* 7 (2016).

[70] D. Ristè, M. Dukalski, C. A. Watson, G. de Lange, M. J. Tiggelman, Y. M. Blanter, K. W. Lehnert, R. N. Schouten and L. DiCarlo. 'Deterministic entanglement of superconducting qubits by parity measurement and feedback.' In: *Nature* 502.7471 (2013), p. 350. doi: 10.1038/nature12513.

[71] E. P. Harris and D. Mapother. 'Critical field of superconducting aluminum as a function of pressure and temperature above 0.3 K'. In: *Phys. Rev.* 165.2 (1968), p. 522.

[72] A. Imamoglu. 'Cavity QED Based on Collective Magnetic Dipole Coupling: Spin Ensembles as Hybrid Two-Level Systems'. In: *Phys. Rev. Lett.* 102 (8 2009), p. 083602. url: http://link.aps.org/doi/10.1103/PhysRevLett.102.083602.

[73] J. M. Kosterlitz and D. J. Thouless. 'Ordering, metastability and phase transitions in two-dimensional systems'. In: *J. Phys. C* 6.7 (1973), p. 1181.

[74] A. Andreev. 'The Thermal Conductivity of the Intermediate State in Superconductors'. In: *JETP* 19.5 (1964), p. 1228.

[75] J. Pillet, C. Quay, P. Morfin, C. Bena, A. L. Yeyati and P. Joyez. 'Andreev bound states in supercurrent-carrying carbon nanotubes revealed'. In: *Nat. Phys.* 6.12 (2010), pp. 965–969.

[76] D. J. van Woerkom, A. Proutski, B. van Heck, D. Bouman, J. I. Väyrynen, L. I. Glazman, P. Krogstrup, J. Nygård, L. P. Kouwenhoven and A. Geresdi. 'Microwave spectroscopy of spinful Andreev bound states in ballistic semiconductor Josephson junctions'. In: *Nat. Phys.* (2017).

[77] T. Yokoyama, M. Eto and Y. V. Nazarov. 'Josephson current through semiconductor nanowire with spin–orbit interaction in magnetic field'. In: *J. Phys. Soc. Jap.* 82.5 (2013), p. 054703.

[78] N. Samkharadze, A. Bruno, P. Scarlino, G. Zheng, D. DiVincenzo, L. DiCarlo and L. Vandersypen. 'High-kinetic-inductance superconducting nanowire resonators for circuit QED in a magnetic field'. In: *Phys. Rev. App.* 5.4 (2016), p. 044004.

[79] M. Popinciuc, V. E. Calado, X. L. Liu, A. R. Akhmerov, T. M. Klapwijk and L. M. Vandersypen. 'Zero-bias conductance peak and Josephson effect in graphene-NbTiN junctions'. In: *Phys. Rev. B* 85.20 (2012), p. 205404.

[80] Y.-J. Doh, J. A. van Dam, A. L. Roest, E. P. Bakkers, L. P. Kouwenhoven and S. De Franceschi. 'Tunable supercurrent through semiconductor nanowires'. In: *Science* 309.5732 (2005), pp. 272–275.

[81] E. Pallecchi, M. Gaaß, D. Ryndyk and C. Strunk. 'Carbon nanotube Josephson junctions with Nb contacts'. In: *App. Phys. Lett.* 93.7 (2008), p. 072501.

[82] M. Della Rocca, M. Chauvin, B. Huard, H. Pothier, D. Esteve and C. Urbina. 'Measurement of the current-phase relation of superconducting atomic contacts'. In: *Phys. Rev. Lett.* 99.12 (2007), p. 127005.

[83] C. Janvier *et al.* 'Coherent manipulation of Andreev states in superconducting atomic contacts'. In: *Science* 349.6253 (2015), pp. 1199–1202.

[84] S. Chuang, Q. Gao, R. Kapadia, A. C. Ford, J. Guo and A. Javey. 'Ballistic InAs nanowire transistors'. In: *Nano Lett.* 13.2 (2013), pp. 555–558.

[85] Y.-Y. Liu, J. Stehlik, C. Eichler, M. Gullans, J. M. Taylor and J. Petta. 'Semiconductor double quantum dot micromaser'. In: *Science* 347.6219 (2015), pp. 285–287.

[86] D. J. Thoen, B. G. C. Bos, E. Haalebos, T. Klapwijk, J. Baselmans and A. Endo. 'Superconducting NbTin Thin Films With Highly Uniform Properties Over a

{

varnothing}100 mm Wafer'. In: *IEEE T. Appl. Supercon.* 27.4 (2017), pp. 1–5. url: http://ieeexplore.ieee.org/document/7752837/.

[87] B. G. C. Bos, D. J. Thoen, E. Haalebos, P. Gimbel, T. Klapwijk, J. Baselmans and A. Endo. 'Reactive magnetron sputter deposition of superconducting niobium titanium nitride thin films with different target sizes'. In: *IEEE T. Appl. Supercon.* 27.4 (2017), pp. 1–5.

[88] A. Bruno, G. de Lange, S. Asaad, K. L. van der Enden, N. K. Langford and L. DiCarlo. 'Reducing intrinsic loss in superconducting resonators by surface treatment and deep etching of silicon substrates'. In: *App. Phys. Lett.* 106 (2015), p. 182601. url: http://scitation.aip.org/content/aip/journal/apl/106/18/10.1063/1.4919761.

[89] W. Chang, S. M. Albrecht, T. S. Jespersen, F. Kuemmeth, P. Krogstrup, J. Nygård and C. M. Marcus. In: *Nat. Nanotechnol.* 10 (232 2015).

[90] J. M. Martinis, M. Ansmann and J. Aumentado. 'Energy Decay in Superconducting Josephson-Junction Qubits from Nonequilibrium Quasiparticle Excitations'. In: *Phys. Rev. Lett.* 103 (9 2009), p. 097002. doi: 10.1103/PhysRevLett.103.097002.

[91] C. Wang *et al.* 'Measurement and control of quasiparticle dynamics in a superconducting qubit'. In: *Nat. Commun.* 5 (2014), p. 5836.

[92] See supplemental material.

[93] Itseez. *Open Source Computer Vision Library*. https://github.com/itseez/opencv. 2015.

[94] F. Motzoi, J. M. Gambetta, P. Rebentrost and F. K. Wilhelm. 'Simple Pulses for Elimination of Leakage in Weakly Nonlinear Qubits'. In: *Phys. Rev. Lett.* 103 (2009), p. 110501. url: https://journals.aps.org/prl/abstract/10.1103/PhysRevLett.103.110501.

[95] M. Jerger, S. Poletto, P. Macha, U. Hübner, E. Il'ichev and A. V. Ustinov. 'Frequency division multiplexing readout and simultaneous manipulation of an array of flux qubits'. In: *App. Phys. Lett.* 101.4 (2012), p. 042604. doi: http://dx.doi.org/10.1063/1.4739454.

[96] J. M. Martinis, S. Nam, J. Aumentado, K. M. Lang and C. Urbina. 'Decoherence of a superconducting qubit due to bias noise'. In: *Phys. Rev. B* 67.9 (2003), p. 094510. url: https://doi.org/10.1103/PhysRevB.67.094510.

[97] M. Hutchings, J. B. Hertzberg, Y. Liu, N. T. Bronn, G. A. Keefe, M. Brink, J. M. Chow and B. Plourde. 'Tunable superconducting qubits with flux-independent coherence'. In: *Phys. Rev. App.* 8.4 (2017), p. 044003. url: https://journals.aps.org/prapplied/abstract/10.1103/PhysRevApplied.8.044003.

[98] W. D. Oliver and P. B. Welander. 'Materials in superconducting quantum bits'. In: *MRS bulletin* 38.10 (2013), pp. 816–825.

[99] M. Tinkham. *Introduction to Superconductivity*. 2nd. New York: McGraw-Hill, 1996.

[100] A. A. Houck *et al.* 'Controlling the Spontaneous Emission of a Superconducting Transmon Qubit'. In: *Phys. Rev. Lett.* 101, 080502 (2008), p. 080502.

[101] S. Gazibegovic *et al.* 'Epitaxy of advanced nanowire quantum devices'. In: *Nature* 548.7668 (2017), pp. 434–438. url: http://dx.doi.org/10.1038/nature23468.

[102] R. Barends *et al.* 'Minimizing quasiparticle generation from stray infrared light in superconducting quantum circuits'. In: *App. Phys. Lett.* 99 (2011), p. 113507. url: http://scitation.aip.org/content/aip/journal/apl/99/11/10.1063/1.3638063.

[103] S. Asaad, C. Dickel, S. Poletto, A. Bruno, N. K. Langford, M. A. Rol, D. Deurloo and L. DiCarlo. 'Independent, extensible control of same-frequency superconducting qubits by selective broadcasting'. In: *npj Quantum Inf.* 2 (2016), p. 16029. url: https://www.nature.com/articles/npjqi201629.

[104] P. Krogstrup, N. Ziino, W. Chang, S. Albrecht, M. Madsen, E. Johnson, J. Nygård, C. M. Marcus and T. Jespersen. 'Epitaxy of semiconductor–superconductor nanowires'. In: *Nat. Mater.* 14.4 (2015), pp. 400–406. url: https://doi.org/10.1038/nmat4176.

[105] D. Ristè, S. Poletto, M. .-. Huang, A. Bruno, V. Vesterinen, O. .-. Saira and L. DiCarlo. 'Detecting bit-flip errors in a logical qubit using stabilizer measurements'. In: *Nat. Commun.* 6 (2015), p. 6983. url: https://www.nature.com/articles/ncomms7983.

[106] Ö. Gül, D. J. Van Woerkom, I. van Weperen, D. Car, S. R. Plissard, E. P. Bakkers and L. P. Kouwenhoven. 'Towards high mobility InSb nanowire devices'. In: *Nanotechnology* 26.21 (2015), p. 215202.

[107] N. Otsu. In: 9 (1 1979), pp. 62–66. doi: 10.1109/TSMC.1979.4310076.

[108] J. Serra. *Image Analysis & Mathematical Morphology*. Academic Press, 1997. url: https://books.google.nl/books?id=jQwlnAEACAAJ.

[109] J. Canny. In: 8 (6 1986), pp. 679–698. doi: 10.1109/TPAMI.1986.4767851.

[110] D. H. Ballard. 'Generalizing the Hough transform to detect arbitrary shapes'. In: *Pattern recognition* 13.2 (1981), pp. 111–122.

[111] D. Bothner, T. Gaber, M. Kemmler, D. Koelle, R. Kleiner, S. Wünsch and M. Siegel. 'Magnetic hysteresis effects in superconducting coplanar microwave resonators'. In: *Phys. Rev. B* 86 (1 2012), p. 014517. url: https://link.aps.org/doi/10.1103/PhysRevB.86.014517.

[112] T. Stavenga and L. DiCarlo. *Lower-temperature fabrication of airbridges by grayscale lithography to increase yield of nanowire transmons in circuit QED quantum processors*. 2023. url: https://arxiv.org/abs/2301.04065.

[113] N. H. L. Koster, S. Koblowski, R. Bertenburg, S. Heinen and I. Wolff. 'Investigations on air bridges used for MMICs in CPW technique'. In: *1989 19th European Microwave Conference*. IEEE. 1989, pp. 666–671. url: https://doi.org/10.1063/1.4863745.

[114] Y. Lankwarden, A. Endo, J. Baselmans and M. Bruijn. 'Development of NbTiN-Al direct antenna coupled kinetic inductance detectors'. In: *Journal of Low Temperature Physics* 167.3 (2012), pp. 367–372. url: https://link.springer.com/article/10.1007/s10909-012-0503-0.

[115] M. Abuwasib, P. Krantz and P. Delsing. 'Fabrication of large dimension aluminum air-bridges for superconducting quantum circuits'. In: *Journal of Vacuum Science & Technology B* 31.3 (2013), p. 031601. url: https://doi.org/10.1116/1.4798399.

[116] Z. Chen *et al.* 'Fabrication and characterization of aluminum airbridges for superconducting microwave circuits'. In: *App. Phys. Lett.* 104.5 (2014), p. 052602. url: https://doi.org/10.1063/1.4863745.

[117] N. Janzen, M. Kononenko, S. Ren and A. Lupascu. 'Aluminum air bridges for superconducting quantum devices realized using a single-step electron-beam lithography process'. In: *App. Phys. Lett.* 121.9 (2022), p. 094001. url: https://doi.org/10.1063/5.0103165.

[118] C. Wen. 'Coplanar waveguide: a surface strip transmission line suitable for nonreciprocal gyromagnetic device applications'. In: *IEEE Trans. Microwave Theory Tech.* 17.12 (1969), pp. 1087–1090. url: https://ieeexplore.ieee.org/document/1127105?arnumber=1127105.

[119] R. N. Simons. *Coplanar waveguide circuits, components and systems*. New York: Wiley-Interscience, 2001.

[120] R. Versluis, S. Poletto, N. Khammassi, B. Tarasinski, N. Haider, D. J. Michalak, A. Bruno, K. Bertels and L. DiCarlo. 'Scalable Quantum Circuit and Control for a Superconducting Surface Code'. In: *Phys. Rev. Applied* 8 (3 2017), p. 034021. url: https://link.aps.org/doi/10.1103/PhysRevApplied.8.034021.

[121] J. F. Marques, B. M. Varbanov, M. S. Moreira, H. Ali, N. Muthusubramanian, C. Zachariadis *et al.* 'Logical-qubit operations in an error-detecting surface code'. In: *Nat. Phys.* 18.1 (2022), pp. 80–86. url: https://doi.org/10.1038/s41567-021-01423-9.

[122] J. Alfaro-Barrantes, M. Mastrangeli, D. Thoen, S. Visser, J. Bueno, J. Baselmans and P. Sarro. 'Superconducting high-aspect ratio through-silicon vias with DC-sputtered Al for quantum 3D integration'. In: *IEEE Electron Device Lett.* 41.7 (2020), pp. 1114–1117. doi: 10.1109/LED.2020.2994862.

[123] D. Yost *et al.* 'Solid-state qubits integrated with superconducting through-silicon vias'. In: *npj Quantum Inf.* 6.1 (2020), pp. 1–7. url: https://doi.org/10.1038/s41534-020-00289-8.

[124] J. Mallek, D. Yost, D. Rosenberg, J. Yoder, G. Calusine, M. Cook *et al.* 'Fabrication of superconducting through-silicon vias'. In: *arXiv:2103.08536* (2021). url: https://arxiv.org/abs/2103.08536.

[125] D. Rosenberg *et al.* '3D integrated superconducting qubits'. In: *npj Quantum Inf.* 3.1 (2017), pp. 1–4. url: http://dx.doi.org/10.1038/s41534-017-0044-0.

[126] B. Foxen *et al.* 'Qubit compatible superconducting interconnects'. In: *Quantum Science and Technology* 3.1 (2017), p. 014005. url: https://dx.doi.org/10.1088/2058-9565/aa94fc.

[127] N. T. Bronn, V. P. Adiga, S. B. Olivadese, X. Wu, J. M. Chow and D. P. Pappas. 'High coherence plane breaking packaging for superconducting qubits'. In: *Quantum Science and Technology* 3.2 (2018), p. 024007. url: https://iopscience.iop.org/article/10.1088/2058-9565/aaa645.

[128] C. K. Andersen, A. Remm, S. Lazar, S. Krinner, N. Lacroix, G. J. Norris, M. Gabureac, C. Eichler and A. Wallraff. 'Repeated quantum error detection in a surface code'. In: *Nat. Phys.* 16.8 (2020), pp. 875–880. url: https://doi.org/10.1038/s41567-020-0920-y.

[129] S. Heedt *et al.* 'Shadow-wall lithography of ballistic superconductor–semiconductor quantum devices'. In: *Nat. Commun.* 12.1 (2021), pp. 1–9. url: https://doi.org/10.1038/s41467-021-25100-w.

[130] J. Loomis, D. Ratnayake, C. McKenna and K. M. Walsh. 'Grayscale lithography—automated mask generation for complex three-dimensional topography'. In: *Journal of Micro/Nanolithography, MEMS, and MOEMS* 15.1 (2016), pp. 1–10. url: https://doi.org/10.1117/1.JMM.15.1.013511.

[131] Q. Deng, Y. Yang, H. Gao, Y. Zhou, Y. He and S. Hu. 'Fabrication of Micro-Optics Elements with Arbitrary Surface Profiles Based on One-Step Maskless Grayscale Lithography'. In: *Micromachines* 8.10 (2017), p. 314. url: https://www.mdpi.com/2072-666X/8/10/314.

[132] T. Mortelmans, D. Kazazis, V. A. Guzenko, C. Padeste, T. Braun, H. Stahlberg, X. Li and Y. Ekinci. 'Grayscale e-beam lithography: Effects of a delayed development for well-controlled 3D patterning'. In: *Microelectronic Engineering* 225 (2020), p. 111272. url: https://www.sciencedirect.com/science/article/pii/S0167931720300605.

[133] *GenISys Beamer*. https://www.genisys-gmbh.com/beamer.html.

[134] C. A. Mack. 'Development of Positive Photoresists'. In: *Journal of The Electrochemical Society* 134.1 (1987), pp. 148–152. url: https://doi.org/10.1149/1.2100396.

[135] F. Pedregosa *et al.* 'Scikit-learn: Machine Learning in Python'. In: *Journal of Machine Learning Research* 12 (2011), pp. 2825–2830. url: https://jmlr.csail.mit.edu/papers/v12/pedregosa11a.html.

[136] J. G. Kroll, W. Uilhoorn, K. L. van der Enden, D. de Jong, K. Watanabe, T. Taniguchi, S. Goswami, M. C. Cassidy and L. P. Kouwenhoven. 'Magnetic field compatible circuit quantum electrodynamics with graphene Josephson junctions'. In: *Nature Communications* 9.1 (2018), p. 4615. url: https://doi.org/10.1038/s41467-018-07124-x.

[137] G. A. Álvarez and D. Suter. 'Measuring the Spectrum of Colored Noise by Dynamical Decoupling'. In: *Phys. Rev. Lett.* 107 (23 2011), p. 230501. url: https://link.aps.org/doi/10.1103/PhysRevLett.107.230501.

[138] T. Yuge, S. Sasaki and Y. Hirayama. 'Measurement of the Noise Spectrum Using a Multiple-Pulse Sequence'. In: *Phys. Rev. Lett.* 107 (17 2011), p. 170504. url: https://link.aps.org/doi/10.1103/PhysRevLett.107.170504.

[139] G. A. Paz-Silva and L. Viola. 'General Transfer-Function Approach to Noise Filtering in Open-Loop Quantum Control'. In: *Phys. Rev. Lett.* 113 (25 2014), p. 250501. url: https://link.aps.org/doi/10.1103/PhysRevLett.113.250501.

[140] A. Vepsäläinen *et al.* 'Improving qubit coherence using closed-loop feedback'. In: *Nature Communications* 13.1 (2022), p. 1932. url: https://doi.org/10.1038/s41467-022-29287-4.

[141] F. Yan, S. Gustavsson, J. Bylander, X. Jin, F. Yoshihara, D. G. Cory, Y. Nakamura, T. P. Orlando and W. D. Oliver. 'Rotating-frame relaxation as a noise spectrum analyser of a superconducting qubit undergoing driven evolution'. In: *Nature Communications* 4.1 (2013), p. 2337. url: https://doi.org/10.1038/ncomms3337.

[142] F. Yoshihara, Y. Nakamura, F. Yan, S. Gustavsson, J. Bylander, W. D. Oliver and J.-S. Tsai. 'Flux qubit noise spectroscopy using Rabi oscillations under strong driving conditions'. In: *Phys. Rev. B* 89 (2 2014), p. 020503. url: https://link.aps.org/doi/10.1103/PhysRevB.89.020503.

[143] F. Yan *et al.* 'Distinguishing Coherent and Thermal Photon Noise in a Circuit Quantum Electrodynamical System'. In: *Phys. Rev. Lett.* 120 (26 2018), p. 260504. url: https://link.aps.org/doi/10.1103/PhysRevLett.120.260504.

[144] G. S. Uhrig. 'Keeping a Quantum Bit Alive by Optimized π-Pulse Sequences'. In: *Phys. Rev. Lett.* 98 (10 2007), p. 100504. url: https://link.aps.org/doi/10.1103/PhysRevLett.98.100504.

[145] M. A. Rol *et al.* 'Restless Tuneup of High-Fidelity Qubit Gates'. In: *Phys. Rev. Applied* 7 (4 2017), p. 041001. url: https://link.aps.org/doi/10.1103/PhysRevApplied.7.041001.

[146] M. W. H. Garming, I. G. C. Weppelman, M. Lee, T. Stavenga and J. P. Hoogenboom. 'Ultrafast scanning electron microscopy with sub-micrometer optical pump resolution'. In: *Applied Physics Reviews* 9.2 (2022), p. 021418. url: https://doi.org/10.1063/5.0085597.

[147] N. Muthusubramanian, P. Duivestein, C. Zachariadis, M. Finkel, S. L. van der Meer, H. M. Veen, M. W. Beekman, T. Stavenga, A. Bruno and L. DiCarlo. 'Wafer-scale uniformity of Dolan-bridge and bridgeless Manhattan-style Josephson junctions for superconducting quantum processors'. In: *arXiv preprint arXiv:2304.09111* (2023). url: https://arxiv.org/abs/2304.09111.

[148] S. Vallés-Sanclemente, S. van der Meer, M. Finkel, N. Muthusubramanian, M. Beekman, H. Ali, J. Marques, C. Zachariadis, H. Veen, T. Stavenga *et al.* 'Post-fabrication frequency trimming of coplanar-waveguide resonators in circuit QED quantum processors'. In: *arXiv preprint arXiv:2302.10705* (2023). url: https://arxiv.org/abs/2302.10705.

Acknowledgements

The work in this thesis is the culmination of many years based on the work of many people. It goes without saying that much of the content would not have been possible without the help and assistance of all of them. Therefore I would like to take this opportunity to individually thank you for being part of this journey with many ups and downs. Without your care and support this would have been impossible. Thank you!

In this part I would like to revisit my experience on how my journey to becoming a PhD went and why I did a Phd in the first place. Then I will acknowledge the people that helped me within Qutech to achieve my goals. Finally I will thank everyone outside of work who was there to support me and help me get through it.

My journey towards doing a PhD started in the group of charged particle optics (CPO), where I did my bachelor thesis on ultrafast laser pulses. Thank you, **Gerward** for your guidance during my first scientific project. Before this I did not see myself as a scientist, since I was never among the best in any class and I never got the encouragement before to know I could do this. You showed me that I could do it in a succesful way. Also thank you outside of the work environment for being a friend, I still have your kitchen ware and cutlery after you moved to the United States. **Robert**, you were there whenever I had questions and were always available for help. Also we went out after work and had discussions that I greatly enjoyed, thank you for that. **Jacob**, you were the supervisor of the project for which I will be eternally grateful. You changed my academic career on two occasions. Firstly by having the faith and confidence in me after my bachelor project to hire me as a part-time student assistant, where I could independently work on the experiment after my bachelor project had finished on a similar topic. This experience and confidence that I got from you greatly helped me with everything I have done since. Additionally you also supervised my internship during my master when I went to Buenos Aires for 6 months. This was a great experience for which I am eternally grateful.

After these experiences what came next was my master thesis in the same group where I would later do my PhD. Here, I would like to express my gratitude to my PhD promoter, **Leo**, for your guidance and mentorship throughout both my master thesis as well as during my PhD. Your insightful feedback, expertise, and persistance have been instrumental in shaping my research and helping me achieve my academic goals. I am truly grateful for your dedication and commitment to my work, and I feel privileged to have had the opportunity to work under your supervision. **Florian**, you were

my supervisor during my master project. I had a great deal of fun both during and outside of work. I feel like we complemented each other in our skills greatly and made the perfect team together. It was an honor to work with you both during my maste and during the first year of my PhD. I wish you all the best with your wife **Nienke** in the USA and I hope to see you again soon. **Elmore**, thank you for choosing me as your supervisor. I am grateful for our moments together and I am glad you could find your job as a PhD student with Chris. **Tumi**, you introduced me to a lot of different culture, art and video games. It was always a good time and an honour to work with you. Good luck in your job at TNO. I would like to extend my appreciation to **Rebecca**, the master student whom I had the pleasure of supervising during her research project. her hard work, enthusiasm, and commitment have been truly inspiring, and it has been a privilege to work with you. I am grateful for the opportunity to have worked with such a dedicated student, and I wish you all the best in your future endeavors in your work with **Srijit**. **Nathan**, you were one of the first people I met in the lab. I have always enjoyed our discussions, you were always ready to help and were selfless ready for others. **Chris**, you were the center of the lab regarding to the PhD students in the lab when I joined. You always organized fun activities and the music night exemplified this. It was always fun to be around you and you always amazed me with your broad knowledge. **Ramiro**, you were always the positive light in the lab. Hanging around with you and going out was amazing and you are super entertaining. Your dedication during your PhD was inspiring and you are truly a great person. I wish you all the best in Barcelona. **Nandini**, you always went your own way and were never deterred to let other people tell you what to do. This means that you have a lot of dedication and persistance to reach your goals. You have truly overcome many difficulties. I admire that a lot, I hope you can soon be reunited with your husband. I wish you all the best. **Jorge**, Your presentations are some of the best I have ever seen. I am sure that you wil have a lot of success in your future endeavours. Together with **Andreia** you make a great team and combination. Besides that I also enjoyed playing football together in the quantum warriors and the nights we had during covid, which was a difficult time. I wish you all the best with finishing your PhD and afterwards. **Miguel**, you are one of the hardest working people I have met. I am impressed by the output you had, while you did not have a formal training in the field. I am impressed how far you got in such a short time. I thank you also for the nights together with jorge that you mostly organised during covid. It was a hard time for all of us and especially for me. You care about the wellbeing of the members of the lab beyond what was obvious on the surface. I appreciate that more than anything. Thank you **Adriaan** for your assistance with pycQED, our measurement system, and being a helpful member of the lab as well as being manager during the meetings. You always brought order into a sometimes chaotic situation. I wish you the best with your company, Orange quantum systems. **Niels**,

you could always brighten the mood during tense times with your great humour. Thank you for being a light minded member of the lab during my PhD. **Santi**, you are a reliable colleague and friend. You never take the easy route, always challenge yourself and do what you think is best. You don't take the path of least resistance, but you take your own path. I have a lot of respect for that. I wish you all the best with the tunable couplers and I am sure our paths will cross in the future. **Hany**, for someone who did not have a physics background you have mastered your subject very well. I am impressed how you dealt with the many challenges that have come on your path so far. Your parties at your house were very nice with great food and attention to detail. I wish you the best in your future endeavours together with your wife **Jawahir**. **Sean**, I love your positive vibe and perspective on life. It has always been a pleasure working with you, your coding and organisation skills are amazing and something I admire a lot. I wish you a great future during both with your PhD and together with your fiancee **Zalyna**. **Ruggero**, we only had a short overlap in the lab, but during that time you have become an important and valued member. Outside of the lab you are also a great part during the drinks and friday night celebrations. I am happy that we had a bit of overlap and the opportunity to meet you. **Tim**, we had great nights in the lab playing card games when not much else was possible due to covid. This was a great way to get to know each other better and I enjoyed every moment of it. I especially remember the cards against humanity fondly. I hope you can find the same joy in your PhD as you did in your master thesis in the group. The group is not complete without mentioning the fabrication team that worked hard in the cleanroom to make the devices that most of us relied on. **Alessandro**, you are both creative and sometimes even a bit crazy. There is a saying that every idea in chip making has already been done by you. You are truly inspirational. **Matvey**, I admire your mastery of the cleanroom processes. You were always a very gentle and friendly person to me, which I am appreciative of. **Martijn**, when I met you when you started your bachelor thesis in the group I thought your project was impossible. However you showed me I was wrong. I am very impressed by that, I wish you the best in your cleanroom endeavours. Thank you **Christos**, for helping me in the cleanroom doing parts of the fabrication of the chips i made. Without you this would have taken substantially longer. For the people that were also part of the lab at some point, but I have not worked together with as long or as intensely, I thank you for the part that you played during the time that we were both in the lab. The fact that I do not address you individually does not mean that I do not appreciate you just as much as any other member. For that reason I would like to thank **Filip**, **Brian**, **Matt**, **Jacob**, **Wouter**, **Slava**, **Stefano**, **Nadia**, **Dave**, **Sarwan**, **René** and many others.

My sincere gratitude goes to our collaborators in Copenhagen, whom have provided us with great nanowires. Without these, the experiments would not have been possible. I owe a thank you to all of the technicians that

upgrades the systems and made sure everything keeps running smoothly. **Jelle**, **Siebe**, **Roy**, **Mark** and **Remco**, it is clear that without you the lab work would have been impossible. Thank you very much for maintaining the place and doing the chores that allowed us to do what we do. **Olaf**, you always have good advice when it comes to the shenanigans of the fridges. Your vast knowledge of cryogenic systems has been invaluable to me with all of the crashes that we had in the past years. Thank you for saving me when the cooling water decided to stop for the umpteenth time. **Jason**, you helped me always when some out-there idea had to be done and no one really knew how to do it. **Raymond** and **Raymond**, your technical knowledge about electronics is unrivalled. No matter the crazy setup you always knew the critical points and mistakes we made. Your help is always to the point and there is always something that I have not thought of in your advice. I have learned a lot from you on electronics continuing to the end of my PhD, thank you for that. Furthermore, I would like to thank the management assistants. Marja and Jenny, you guys are amazing. All of the administrative tasks happened so fast thanks to you. With everything you helped no matter the request. Your organising skills are undervalued, the christmas party especially stands out as a great Qutech event.

Next I would like to turn to those people that helped with discussions on the topics of the PhD and helped in general. First I would like to thank the folks from the Kouwenhoven group: **Damaz**, **Willemijn**, **James**, **Michiel**, **Jaap**, **Martha**, **Arno**, **Lukas**, **Alex**. The expertise that you have on nanowires was invaluable knowledge that I happily used. Doing a hybrid project meant that I sometimes had more overlap with you guys than in my own group. Especially in fabrication the knowledge that was present on the nanowires is unrivalled. The amazing work that your group has done in one of the hardest circumstances is unparalleled. Also out of the lab during friday night dinners it was always a pleasure to be in your company. Thank you for all the great times.

Next I would like to turn to those people that made the the life both inside and outside of the Qutech environment so much more pleasant. Many of which I have met during football, which is one of my passions that I played my whole life. Thank you **Gustavo**, **Chris**, **Valentin**, **Francesco**, **Stefano**, **Alberto**, **Mark**, **Michael**, **Sjoerd**, **Bas**, **Fabrizio**, **Emanuele**, **Maarten**, **Anta** and many more, thank you for the great times during football. We improved so much during the last few years. In the beginning we hardly won anything and the first half of the season we got to be number one! No matter where we were on the table I have always enjoyed playing on the monday evening and I hope I will be able to participate for a while still. Another group of people that I have learned a lot from is the group of **Srijit**: **Chris**, **Ivan**, **Qing** and many others. A very kind group of people that was always there to help. However the time I most enjoyed were the friday nights at TPKV and afterwards. You guys are something special and I will miss those days. On a similar note I would like to thank the people that have made my life at

Qutech more enjoyable. These people include **Pablo**, **Hanifa**, **Oriol**, **Vicky**, **Mohammed**, **Brennan** and others.

Thank you **Lucía** for the support you have given me during the past years, especially during the hard times. There were many difficult moments during the PhD and you were there for me when it mattered.

Als laatste wil ik graag mijn familie bedanken. Zonder de hulp van hen had ik de PhD nooit af kunnen maken. **Albert** en **Anneke**, dankjulliewel voor alle onvoorwaardelijke steun die jullie mij de afgelopen jaren hebben gegeven. Als ik ergens mee zat of hulp nodig had stonden jullie altijd meteen klaar om te helpen. **Ruben** en **Mirte**, Jullie zijn de beste broer en zus die iemand kan wensen. Ik voel me erg blij met het feit dat jullie mijn broer en zus zijn.

Curriculum Vitæ

Thijs Stavenga

02-10-1992 Born in Woudenberg, The Netherlands.

Education

2004–2010 Secondary School
Johan van Oldebarneveldt Gymnasium, Amersfoort, The Netherlands

2010–2014 Bachelor of Science, Applied Physics
Delft University of Technology, Delft, The Netherlands
Thesis: Dispersion compensation introduced by an objective lens for ultra-short laser pulses
Supervisor: Prof. dr. J.P. Hoogenboom

2014–2017 Master of Science, Applied Physics
Delft University of Technology, Delft, The Netherlands
Thesis: Transmon qubits with a nanowire Josephson junction
Supervisor: Prof. dr. L. Di Carlo

2017–2022 PhD. Physics
Delft University of Technology, Delft, The Netherlands
Thesis: Flux noise in a magnetic field
Promotor: Prof. dr. L. Di Carlo

List of Publications

5. F. Luthi, T. Stavenga, O. Enzing, A. Bruno, C. Dickel, N. Langford, M. A. Rol, T. S. Jespersen, J. Nygård, P. Krogstrup and L. DiCarlo. 'Evolution of nanowire transmon qubits and their coherence in a magnetic field'. In: *Phys. Rev. Lett.* 120.10 (2018), p. 100502. url: https://doi.org/10.1103/PhysRevLett.120.100502

4. M. W. H. Garming, I. G. C. Weppelman, M. Lee, T. Stavenga and J. P. Hoogenboom. 'Ultrafast scanning electron microscopy with sub-micrometer optical pump resolution'. In: *Applied Physics Reviews* 9.2 (2022), p. 021418. url: https://doi.org/10.1063/5.0085597

3. T. Stavenga and L. DiCarlo. *Lower-temperature fabrication of airbridges by grayscale lithography to increase yield of nanowire transmons in circuit QED quantum processors*. 2023. url: https://arxiv.org/abs/2301.04065

2. N. Muthusubramanian, P. Duivestein, C. Zachariadis, M. Finkel, S. L. van der Meer, H. M. Veen, M. W. Beekman, T. Stavenga, A. Bruno and L. DiCarlo. 'Wafer-scale uniformity of Dolan-bridge and bridgeless Manhattan-style Josephson junctions for superconducting quantum processors'. In: *arXiv preprint arXiv:2304.09111* (2023). url: https://arxiv.org/abs/2304.09111

1. S. Vallés-Sanclemente, S. van der Meer, M. Finkel, N. Muthusubramanian, M. Beekman, H. Ali, J. Marques, C. Zachariadis, H. Veen, T. Stavenga *et al.* 'Post-fabrication frequency trimming of coplanar-waveguide resonators in circuit QED quantum processors'. In: *arXiv preprint arXiv:2302.10705* (2023). url: https://arxiv.org/abs/2302.10705